VIRUS-HOST INTERACTIONS MEDIATED BY PEA ENATION MOSAIC VIRUS 2 BIOMOLECULAR CONDENSATES

A DISSERTATION IN
Cell Biology and Biophysics
and
Molecular Biology and Biochemistry
and
Biomedical and Health Informatics

Presented to the Faculty of the University
of Missouri-Kansas City in partial fulfillment of
the requirements for the degree

DOCTOR OF PHILOSOPHY

by
SHELBY L. BROWN

B.S., University of Missouri-Kansas City, 2019
M.S., University of Missouri-Kansas City, 2022

Kansas City, Missouri
2024

VIRUS-HOST INTERACTIONS MEDIATED BY PEA ENATION MOSAIC VIRUS 2 BIOMOLECULAR CONDENSATES

Shelby Leigh Brown, Candidate for the Doctor of Philosophy Degree

University of Missouri-Kansas City, 2024

ABSTRACT

The concept of phase separation applied to biological systems has been rapidly building momentum and interest. Phase separation is the conversion of a single-phase solution into two distinct phases: a dilute phase and a concentrated droplet phase. When applied to cells, the term droplet refers to membraneless organelles or condensates that concentrate biomolecules like proteins and RNA. Viruses can interfere with host condensates, like the nucleolus or stress granules, as well as generate condensates to facilitate viral processes. Our research suggests that electrostatic interactions in the intrinsically disordered region of p26, a movement protein encoded by the +sense RNA plant virus Pea enation mosaic virus 2 (PEMV2), drive p26 phase separation to form viral condensates. We demonstrate co-localization of p26 with host proteins, specifically fibrillarin and G3BP1, into condensates during virus infection and subsequently illustrate the importance of G3BP1 phase separation in the plant anti-viral response. These findings outline a key role for p26 phase separation in the coordination of virus-host interactions, viral ribonucleoprotein (vRNP) formation, and systemic virus movement. This work explores how host- and

virus-induced phase separation impacts virus-host interactions to promote or restrict a virus infection.

Viral condensate research has predominantly centered around the formation of membraneless replication factories by negative sense viruses. However, the function and composition of cytoplasmic condensates formed by positive sense RNA viruses, which utilize membrane-associated replication factories, has been largely uninvestigated. Mass spectrometry revealed that p26 condensates were enriched with ribosomal proteins and fibrillarin, a host rRNA methyltransferase hijacked by PEMV2 to support virus movement. Our data shows that p26 expression represses global translation >40% in plants. In corroboration, polysome profiling exposed significant defects in monosome formation for p26-overexpression and virus-infected samples, whereas infection with a mutant virus lacking p26 partially rescued monosome formation.

Our findings suggest that p26 binds rRNA with a high affinity, yet there was no significant alteration in rRNA abundance, processing, or 2'-*O*-methylation. Therefore, we propose that p26-mediated sequestration of fibrillarin, mRNA, rRNA, and ribosomal proteins into condensates may serve as a switch to repress translation in favor of virus trafficking, a process incompatible with active translation.

APPROVAL PAGE

The faculty listed below, appointed by the Dean of the School of Science and Engineering, have examined a dissertation titled “Virus-Host Interactions Mediated by Pea Enation Mosaic Virus 2 Biomolecular Condensates,” presented by Shelby L. Brown, candidate for the Doctor of Philosophy degree, and certify that in their opinion it is worthy of acceptance.

Supervisory Committee

Jared P. May, Ph.D., Committee Chair
Discipline of Cell Biology and Biophysics

Theodore White, Ph.D.
Discipline of Cell Biology and Biophysics

Karen Bame, Ph.D.
Discipline of Molecular Biology and Biochemistry

Michael O’Connor, Ph.D.
Discipline of Molecular Biology and Biochemistry

Monica Gaddis, Ph.D.
Discipline of Biomedical and Health Informatics

CONTENTS

FIGURES

TABLES

ABBREVIATIONS

Term Abbreviations

Abbreviation	Meaning
LLPS	Liquid-Liquid Phase Separation
IDR	Intrinsically disordered region
IDP	Intrinsically disordered protein
CBs	Cajal bodies
p-bodies	Processing bodies
RdRp	RNA-dependent RNA-polymerase
N protein	Nucleoprotein
P protein	Phosphoprotein
+sense	Positive sense
-sense	Negative sense
RNP	Ribonucleoprotein complexes
Fib2	Fibrillarin 2
N. benthamiana	*Nicotiana benthamiana*
SGs	Stress Granules
DFC	Dense fibrillar component (of the nucleolus)
vRNP	Viral ribonucleoprotein complexes
Thaliana	Arabidopsis thaliana
NMD	Nonsense-mediated decay
ORF3	Open Reading Frame 3 (p26 orthologue)

ABBREVIATIONS

Virus Abbreviations

Virus name	Abbreviation	Genome
Human immunodeficiency virus	HIV	+sense ssRNA
Tobacco Mosaic Virus	TMV	+sense ssRNA
Citrus tristeza virus	CTV	+sense ssRNA
Grapevine leafroll-associated virus 3	GLRaV-3	+sense ssRNA
Plum pox virus	PPV	+sense ssRNA
Maize dwarf mosaic virus	MDMV	+sense ssRNA
Potato virus Y	PVY	+sense ssRNA
Rice yellow mottle virus	RYMV	+sense ssRNA
Groundnut rosette virus	GRV	+sense ssRNA
Polio virus	PV	+sense ssRNA
Cricket paralysis virus	CrPV	+sense ssRNA
Brome mosaic virus	BMV	+sense ssRNA
Dengue virus	DENV	+sense ssRNA
Zika virus	ZIKV	+sense ssRNA
Hepatitis C virus	HCV	+sense ssRNA
Influenza A virus	IAV	-sense ssRNA
Rabies virus	RABV	-sense ssRNA
Respiratory syncytial virus	RSV	-sense ssRNA
Vesicular stomatitis virus	VSV	-sense ssRNA
Ebola virus	EBOV	-sense ssRNA
Marburg virus	MARV	-sense ssRNA
Measles virus	MeV	-sense ssRNA
Severe acute respiratory syndrome coronavirus 2	SARS-CoV-2	+sense ssRNA

Virus Abbreviations Continued

Virus name	**Abbreviation**	**Genome**
Semliki forest virus	SFV	+sense ssRNA
Flock house virus	FHV	+sense ssRNA
Pea enation mosaic virus 2	PEMV2	+sense ssRNA
Potato leafroll virus	PLRV	+sense ssRNA
Cauliflower mosaic virus	CaMV	dsDNA
Turnip crinkle virus	TCV	+sense ssRNA
Severe acute respiratory syndrome coronavirus	SARS-CoV	+sense ssRNA
Infectious bronchitis virus	IBV	+sense ssRNA
West Nile virus	WNV	+sense ssRNA
Tomato bushy stunt virus	TBSV	+sense ssRNA
Potato virus A	PVA	+sense ssRNA

CHAPTER 1

1. AN INTRODUCTION TO VIRUSES AND PHASE SEPARATION

Plant Research and Pathology

Plants are indispensable to the existence of humans and animals. First and foremost, contributions by plants and photosynthetic bacteria were fundamental to the formation of Earth's atmosphere.[1] Not only are plants essential for regulating the climate, they are also necessary to regulate the conditions of soil and water, both chemically and biologically.[1] Moreover, plants are the foundation of the biological food-chain, providing nutrients, vitamins, and some essential amino acids that humans can't attain from another source.[1] The knowledge acquired from studying plants and plant pathogens can be also applied to human health. Throughout history plants have been a major source for the development of medicines and drugs, like morphine and aspirin.[2] Aside from being agriculturally relevant, many major scientific advances have been made by studying plants, most notably, the discovery of genetic inheritance.[1] Plants have also been used to understand how light impacts a higher organism's physiological response.[1] Plant research also led to the first successful crystallization of an enzyme and the discovery of transposable elements.[3] Research in plants can also be beneficial for studying pathogens, as the innate immune systems of plants and animals share similarities.[4] Due to the absence of an adaptive immune system, plants use pattern recognition receptors (PRRs) and nucleotide-binding leucine rich

repeat proteins (NB-LRR) to detect pathogens and pathogen effector molecules.[5, 6] Similarly, proteins from the NB-LRR-related (NLR) superfamily contribute to innate immunity by recognizing pathogen by-products in higher organisms, like humans.[5, 7]

Plant pathology research has provided significant insights into many important eukaryotic cellular processes. For example, RNA interference (RNAi) was first described in plants and is recognized as the primary plant anti-viral response, whereas in humans, RNAi is predominantly associated with the regulation of gene expression.[3] RNA interference (RNAi) is a process in which small RNA molecules are assembled into complexes that bind mRNA and target it for degradation.[8] Additionally, an investigation of pathogen-plant interactions led to the discovery of effectors, which are molecules secreted by an organism to benefit that organism.[3, 9] In correspondence with this, transcription activator-like effectors (TALEs), effector proteins that bind to DNA and activate transcription, were first discovered while studying the plant pathogen *Xanthomonas*.[3] These discoveries led to the development of TALE-nucleases (TALENs) for gene editing, which have been tested to treat human diseases in clinical trials.[3] Moreover, the effector-triggered immune response (ETI), a host immune response to virulence factors, was initially demonstrated in plants, and then later in animals.[3] Arguably, one of the most significant contributions to the pathology field was made by a plant pathologist. In 1892, Dmitri Ivanovski discovered the first virus, a plant virus named Tobacco mosaic virus (TMV).[10]

A Short Background on Viruses

Viruses are infectious microbes that rely on living organisms for replication. Viruses have been the causative agent for some of the deadliest pandemics in human history, including the 1918 influenza pandemic and the human immunodeficiency virus (HIV) pandemic that began around 1981.[11] Some well-known human diseases caused by viruses are the flu, polio, herpes, yellow fever, Zika fever, smallpox, and COVID-19.[12-14]

The Baltimore Classification System abides by the basic classification of viruses according to their nucleic acid composition, and further categorizes viruses by strandedness.[15] Currently, this system classifies viruses into 7 groups: double-stranded (ds) DNA viruses, single-stranded (ss) DNA viruses, dsRNA viruses, positive-sense (+sense) RNA viruses, negative-sense (-sense) RNA viruses, reverse transcribing (RT) RNA viruses, and RT-DNA viruses.[16] dsDNA and ssDNA viruses use host polymerases to replicate their genome and to produce mRNA.[15] RT-DNA viruses are replicated by using the enzyme reverse transcriptase to form an RNA intermediate, whereas RT-RNA viruses use the enzyme to produce a DNA intermediate for replication.[15] dsRNA and ssRNA viruses encode an RNA-dependent RNA-polymerase (RdRp) that is used for replication of the viral RNA genome.[15]

The genome of a +sense virus is a single-stranded mRNA that can be directly translated using host machinery in the cytoplasm to produce viral proteins.[17] Once produced, the RdRp generates complementary strands of the viral genome which are used to synthesize additional copies of the genome and viral mRNAs.[17] For -sense

RNA viruses, the RdRp is packaged into the virion, which allows for the synthesis of viral mRNA from the -sense RNA shortly after infection.[17] Next, the viral mRNAs must be translated using host machinery to produce the viral proteins that are required for replication of the -sense RNA genome.[17] However, the host translational machinery typically prefers to translate mRNAs with a 5' cap structure and polyadenylated 3' end because they resemble cellular mRNAs.[18] To overcome this obstacle, many RNA viruses have developed mechanisms that allow them to cap and/or polyadenylate their mRNAs to promote translation of viral transcripts.[17] Though, this is just one of many methods used by viruses to manipulate translation, a prevalent theme that will be discussed throughout this work.

Viruses Manipulate Host Translation to Support Virus Infection

Viruses are dependent on the host translation machinery to generate viral proteins.[19] As such, they must impede host mRNA translation to favor viral protein synthesis, a process known as host shut-off.[19] There are multiple strategies that viruses can use to repress translation of host transcripts. For example, severe acute respiratory syndrome coronavirus (SARS-CoV), a +sense ssRNA virus, encodes the Nsp1 protein, which can cleave host mRNAs by associating with 40S ribosomes.[19] Another method is to induce host shut-off by interfering with the recruitment of ribosomes to host mRNAs and employing alternate methods to recruit ribosomes to viral transcripts.[19]

Many +sense ssRNA viruses encode proteins that directly target translation initiation factors to obstruct ribosome recruitment to host transcripts. Poliovirus (PV) induces host shut-off by encoding a protease that cleaves the translation initiation factors eIF4GI and eIF4GII.[19] The coronaviruses severe acute respiratory syndrome coronavirus (SARS-CoV) and infectious bronchitis virus (IBV), encode a spike (S) protein that interacts with eIF-3F to suppress translation.[19, 20] This class of viruses can also target translation factors indirectly. Dengue virus (DENV) inhibits translation by preventing the assembly of eIF4F, a protein complex that regulates the recruitment of ribosomes to mRNA.[19] This is achieved by increasing the accumulation of a translation repressor, 4E-BP1, to bind the translation initiation factor eIF4E; a process that has also been shown to suppress the host anti-viral response.[19] Viruses that disrupt the formation of eIF4F require alternative methods to initiate translation of viral transcripts, though the mechanisms used by viruses to subvert canonical translation initiation will not be discussed in this work. Viruses also manipulate translation by interfering with host membraneless organelles, a topic that will be explained in greater detail in subsequent sections of this chapter.

Plant Viruses

As of 2022, there were 10,434 species of viruses recognized by the International Committee on Taxonomy of Viruses (ICTV) [21], and almost 2,000 of these are plant viruses.[22] Plant pathogens threaten the security of the agricultural industry and the global food supply, and almost half of disease-causing plant pathogens are

viruses.[23] Globally, the cost associated with crop losses and damages due to plant viruses can exceed 30 billion USD each year.[23]

Compared to DNA plant viruses, RNA viruses are associated with more severe crop losses and substantial damages to agricultural production.[24] The citrus disease caused by Citrus tristeza virus (CTV) is regarded as the most economically important viral citrus disease in the world.[25, 26] It's estimated that CTV infections caused the loss of approximately 100 million citrus trees across the world in the 20th century.[25] The most widespread and economically damaging viral disease of grapevines, Grapevine leafroll disease (GLRD), is estimated to cause $25,000-$40,000 in losses per 10,000 square meters during the vineyard's 25-year lifespan.[25, 27] Grapevine leafroll-associated virus 3 (GLRaV-3) is the primary causative agent for GLRD.[27] Plum pox virus (PPV) infects plants that produce stone fruits (i.e. peaches, apricots, plums, nectarines, etc.), causing fruit to drop prematurely.[25] Crops that are susceptible to PPV can see yield losses of up to 80-100%; the global cost of managing the disease caused by PPV infections over the last 30 years is over $11 billion.[25] Maize dwarf mosaic virus (MDMV), Potato virus Y (PVY), and Rice yellow mottle virus (RYMV) are all examples of plant viruses that are agriculturally and economically devastating.[25] All of these viruses fall into one category: positive-sense single-stranded (ss) RNA viruses, which are the most abundant group of eukaryote-infecting viruses.[16]

Pea Enation Mosaic Virus 2

Pea Enation Mosaic Virus 2 (PEMV2) is a +sense ssRNA virus from the *Tombusviridae* family.[28] The genome of PEMV2 is 4252 nucleotides long and has 4 open reading frames that encode the RdRp, two movement proteins, and a protein believed to be involved in viral replication (Figure 1.1).[28] PEMV2 encodes two movement proteins p26 and p27, associated with long-distance movement and cell-to-cell movement, respectively.[29]

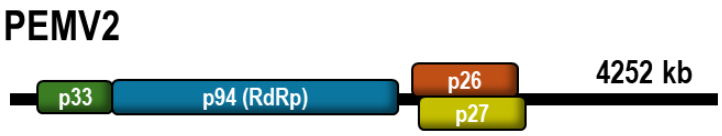

Figure 1.1 A schematic of the Pea enation mosaic virus 2 (PEMV2) genome

A schematic demonstrating the organization of the PEMV2 genome. PEMV2 is a positive-sense RNA virus with a 4252 kb genome. PEMV2 encodes 4 proteins: p33, p94, p26, and p27. P33 is believed to be involved in replication. p94 is the RNA-dependent RNA-polymerase (RdRp). p26 and p27 are movement proteins associated with long-distance and cell-to-cell movement, respectively.

PEMV2 is an umbravirus, a unique genus of viruses that do not encode capsid proteins.[30] Most viruses encode a capsid protein, also known as a coat protein, that encapsulates the viral genome for protection.[30] For plant viruses, capsid proteins are often multi-functional and are necessary for virus movement within the plant and vector transmission of the virus from plant-to-plant.[30] Due to the absence of a capsid protein, umbraviruses must co-infect with a virus from the *Luteoviridae* family for transmission between plants.[30] Though PEMV2 requires the coat protein encoded by

PEMV1, a corresponding luteovirus, to support aphid-transmission of the viruses, PEMV2 does not require a coat protein to spread throughout the plant.[30] Instead, umbraviruses encode movement proteins that facilitate cell-to-cell virus movement through the plasmodesmata and long-distance virus movement through the phloem.[30]

Groundnut rosette virus (GRV) is another umbravirus that encodes a movement protein known as open reading frame 3 (ORF3), an orthologue to p26.[28] Previous work has shown that ORF3 must localize to the nucleolus and be trafficked back into the cytoplasm to form viral ribonucleoprotein particles (vRNPs) capable of systemic virus movement and infection.[31] Soon after, it was discovered that ORF3 interacts with the nucleolar protein fibrillarin.[32] While this interaction was not deemed necessary for virus replication or cell-to-cell movement, it is required for long-distance movement of GRV.[32] It was also found that ORF3 co-localized with fibrillarin in cytoplasmic RNPs, or inclusion bodies.[31] Similarly, p26 is also involved in the formation of RNPs with viral RNA[28] and was shown to localize to large cytoplasmic inclusion bodies.[28, 29]

Phase separation in Biology

Phase separation is the process in which a single-phase solution transitions into two distinct co-existing phases, a dilute phase and a concentrated droplet phase.[33] The droplet phase concentrates biomolecules like proteins and RNA into a membraneless organelle, often referred to as a condensate.[33] Phase separation may be induced in response to a multitude of external and internal cellular stimuli. Notably,

the formation of biomolecular condensates is often linked to the stress response.[34-36] Environmental stress caused by changes in temperature, salinity, pH, and virus infection have all been shown to impact phase separation.[37, 38] In humans, the misregulation of biomolecular condensates has been linked to neurodegenerative diseases, age-related disorders, and cancers.[36, 39]

The biomolecules driving phase separation are often referred to as scaffold molecules.[37] Alternatively, client molecules partition within the condensates formed by scaffold molecules.[37] The multivalency of macromolecules is recognized as a defining characteristic of scaffold molecules.[37, 39] In this context, multivalency refers to the ability of a molecule to form various interactions through multiple domains or motifs.[39] Proteins with multiple binding domains and proteins containing intrinsically disordered regions (IDRs) are examples of multivalent proteins.[40] The IDR of a protein lacks a fixed three-dimensional structure, allowing for conformational heterogeneity and promiscuous binding.[37, 38, 41] Additionally, DNA and RNA molecules containing regions that allow for binding to other proteins or nucleic acid molecules are also multivalent.[40] Multivalent molecules are assembled into larger macromolecules; as the size of the complex increases, the solubility of the molecules will decrease (Figure 1.2).[40] Thus, phase separation transpires when the entropic cost of solubilizing these large complexes becomes higher than the cost of demixing and condensing these complexes.[40]

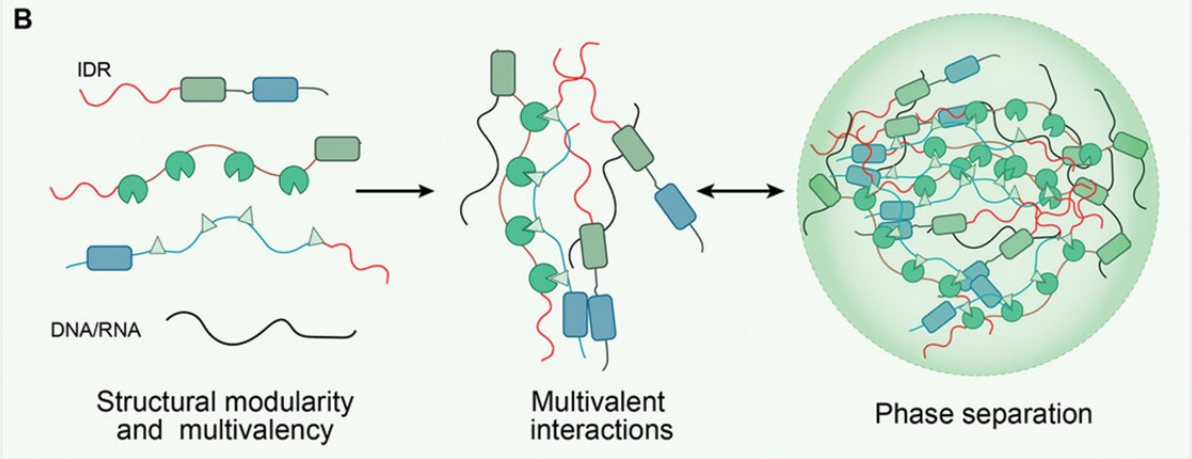

Figure 1.2 Phase Separation is driven by Interactions Between Multivalent Molecules

A simplified illustration depicting the mechanism of phase separation driven by multivalent biomolecular interactions. Adapted with permission from J. Ren, Z. Zhang, Z. Zong, L. Zhang, F. Zhou, Emerging Implications of Phase Separation in Cancer. *Adv. Sci.* 2022, 9, 2202855. https://doi.org/10.1002/advs.202202855. Copyright 2022 The Authors, Advanced Science published by Wiley-VCH GmbH.[42] Licensed under CC BY 4.0 / Cropped from original

Essential Host Condensates Form through Phase Separation

The nucleolus and Cajal bodies (CBs) are examples of nuclear host condensates (Figure 1.3).[38, 40] RNA processing, ribosome assembly, and the modulation of gene expression are all functions that have been associated with nuclear condensates.[33] These host condensates are also involved in RNA silencing, a primary anti-viral response in plants.[31] While nuclear condensates are essential for cell viability, they can also be exploited by viruses. GRV is a +sense ssRNA plant virus that replicates in the cytoplasm, but the long-distance movement protein from GRV

must interact with CBs and the nucleolus to move the virus systemically through the plant.[31]

Stress granules and processing bodies (p-bodies) are examples of cytoplasmic host condensates (Figure 1.3).[38, 40] Cytoplasmic host condensates have been linked to mRNA sequestration, metabolism, and regulation.[33] Cytoplasmic condensates can also serve as a localization site to aid in biochemical reactions.[40] Condensates that concentrate RNA, like p-bodies and stress granules, are often enriched with RNA-binding proteins (RBPs), and intrinsically disordered proteins (IDPs), proteins that contain an IDR and fully disordered proteins.[40, 43]

The formation of some cytoplasmic condensates, specifically stress granules and p-bodies, has been linked to the repression of translation.[33] During the stress response certain components are sequestered into stress granules, though these components are variable depending on the type of stress.[33] Typically these condensates contain key elements for translation, including RBPs involved in translation regulation, metabolic enzymes, and RNAs that are associated with a stalled 48S pre-initiation complex (See Table 1.1).[33] Thus, it is widely believed that mRNAs being temporarily repressed for translation can be stored and regulated in stress granules.[33] P-bodies are cytoplasmic RNPs formed via phase separation and are often associated with the metabolism and decay of mRNA, and translational repression, though the exact functions of p-bodies still remain elusive.[44, 33] By targeting p-bodies and stress granules, viruses are able to exercise control over gene expression in the host.

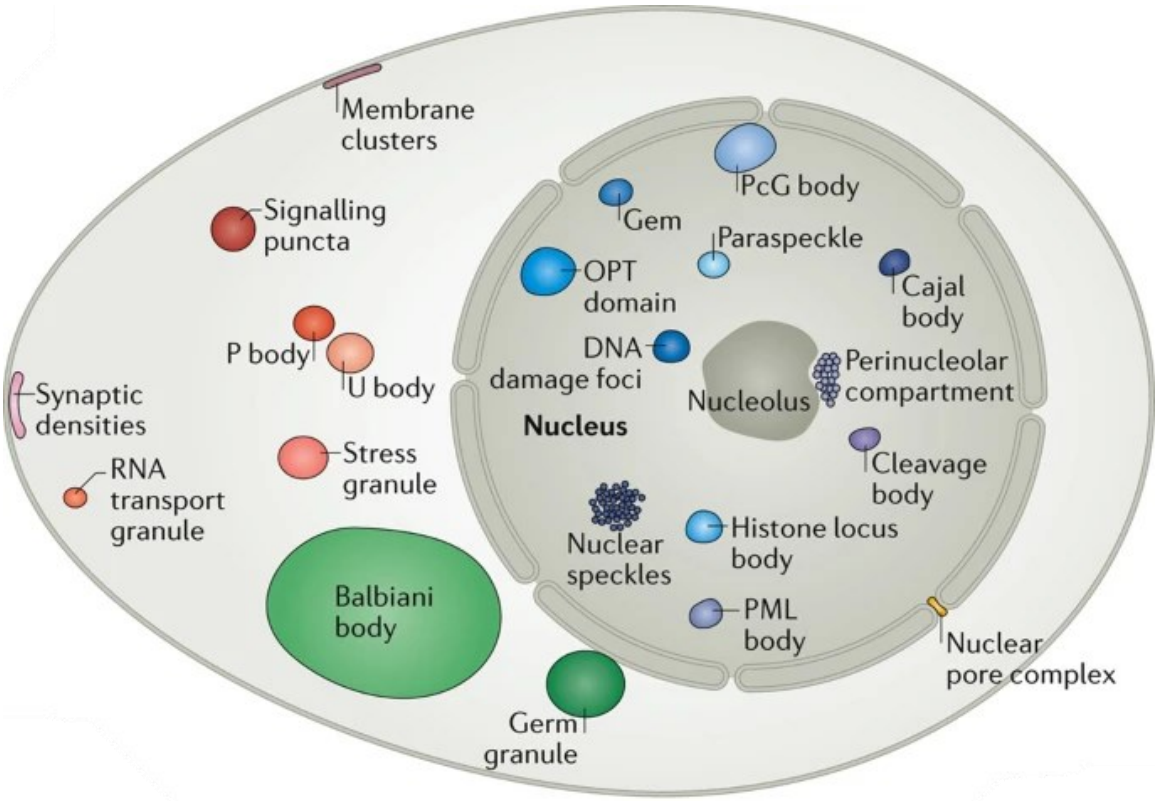

Figure 1.3 Eukaryotic Cytoplasmic and Nuclear Biomolecular Condensates

A diagram demonstrating various biomolecular condensates that have been identified in eukaryotic cells. Granules with a green hue are germ cell specific. Synaptic densities and RNA transport granules are neuronal cell specific. *Reproduced with permission from Springer Nature (SNCSC)*; Banani, S., Lee, H., Hyman, A. *et al.* Biomolecular condensates: organizers of cellular biochemistry. *Nat Rev Mol Cell Biol* **18**, 285–298 (2017). https://doi.org/10.1038/nrm.2017.7. Copyright 2017 Springer Nature.[40]

Table 1.1 An Overview of the Mammalian Stress Granule Proteome

This table provides an overview of the RNA-binding proteins (RBPs) associated with the mammalian stress granule proteome and identified by Jain, S. et al.[45] This data was collected and mined from the published manuscript: Jain S, Wheeler JR, Walters RW, Agrawal A, Barsic A, Parker R. ATPase-Modulated Stress Granules Contain a Diverse Proteome and Substructure. Cell. 2016 Jan 28;164(3):487-98. doi: 10.1016/j.cell.2015.12.038. Epub 2016 Jan 14. PMID: 26777405; PMCID: PMC4733397.

Gene ID	Protein Name	Enzymatic Activity
DDX21	Nucleolar RNA helicase 2	ATPase
CCT6A	T-complex protein 1 subunit zeta	ATPase
DHX30	Putative ATP-dependent RNA Helicase	ATPase
DAZAP1	DAZ-associated protein 1	
EIF3D	Eukaryotic translation initiation factor subunit D	
EIF3G	Eukaryotic translation initiation factor subunit G	
EIF4A1	Eukaryotic initiation factor 4A-I	ATPase
EIF4B	Eukaryotic translation initiation factor 4B	
FMR1	Fragile X mental retardation protein 1	
G3BP1	Ras GTPase-activating protein-binding protein 1	ATPase
HNRNPUL1	Heterogeneous nuclear ribonucleoprotein U-like protein 2	
HNRNPAB	Heterogeneous nuclear ribonucleoprotein A/B	
HNRNPH2	Heterogeneous nuclear ribonucleoprotein H2	
MAP4	Microtubule-associated protein 4	
MSI2	RNA-binding Musashi homolog 2	
PRDX1	Peroxiredoxin-1	
SAFB2	Scaffold attachment factor B2	
STIP1	Stress-induced-phosphoprotein 1	
SUGP2	SURP and G-patch domain-containing protein 2	
TRIP6	Thyroid receptor-interacting protein 6	
ZNF638	Zinc Finger protein 638	
ATXN2	Ataxin-2	
ATXN2L	Ataxin-2-like protein	
CAPRIN1	Caprin-1	
CELF1	CUGBP Elav-like family member 1	
DDX1	ATP-dependent RNA helicase DDX1	ATPase
DDX3X	ATP-dependent RNA helicase DDX3X	ATPase
DDX6	Probable ATP-dependent RNA helicase DDX6	ATPase
EIF3A	Eukaryotic translation initiation factor 3 subunit A	

Gene ID	Protein Name	Enzymatic Activity
EIF3H	Eukaryotic translation initiation factor 3 subunit H	
EIFG1	Eukaryotic translation initiation factor 4 gamma 1	
EIFG2	Eukaryotic translation initiation factor 4 gamma 2	
FXR2	Fragile X mental retardation syndrome-related protein 2	
G3BP2	Ras GTPase-activating protein-binding protein 2	
IGF2BP2	Insulin-like growth factor 2 mRNA-binding protein 2	
MOV10	Putative helicase MOV-10	ATPase
NUFIP2	Nuclear fragile X mental retardation-interaction protein 2	
PABPC4	Polyadenylate-binding protein 4	
PRRC2C	Protein PRRC2C	
PUM1	Pumilio homolog 1	
PURA	Transcriptional activator protein PUR-alpha	
PURB	Transcriptional activator protein Pur-beta	
RBMS2	RNA-binding motif, single-stranded-interacting protein 2	
STAU1	Double-stranded RNA-binding protein Staufen homolog 1	
STAU2	Double-stranded RNA-binding protein Saufen homolog 2	
SYNCRIP	Heterogenous nuclear ribonucleoprotein Q	
TIAL1	Nucleolysin TIAR	
UBAP2	Ubiquitin-associated protein 2	
UBAP2L	Ubiquitin-associated protein 2-like	
UPF1	Regulator of nonsense transcripts 1 Up-frameshift protein 1	
USP10	Ubiquitin carboxyl-terminal hydrolase 10	Hydrolase
CSDE1	Cold shock domain-containing protein E1	
FAM120A	Constitutive coactivator of PPAR-gamma-like protein 1	
FNDC3B	Fibronectin type III domain-containing protein 3B	
FUBP3	Far upstream element-binding protein 3	
FXR1	Fragile X mental retardation syndrome-related protein 1	
IGF2BP1	Insulin-like growth factor 2 mRNA-binding protein 1	
TNPO1	Transportin-1	
TRIM25	E3 ubiquitin/ISG15 ligase TRIM25	Ligase
ZC3H7A	Zinc finger CCCH domain-containing protein 7A	
YTHDF1	YTH domain family protein 1	
YTHDF3	YTH domain family protein 3	
ZC3HAV1	Zinc finger CCCH-type antiviral protein 1	
STRAP	Serine-threonine kinase receptor-associated protein	

There have been multiple reports of +sense ssRNA viruses targeting host condensates to promote virus infection. For example, Brome mosaic virus (BMV) has been shown to target p-bodies to facilitate viral replication.[19] Researchers have identified multiple p-body components that are deemed necessary for BMV translation and replication.[46] It was found that BMV genomic RNAs also accumulate in p-bodies; additionally, the BMV RdRp co-immunoprecipitates and partially co-localizes with the p-body component Lsm1-7p.[46]

In contrast, West Nile virus (WNV) depletes cells of p-bodies and redirects the components of p-bodies, which are important for WNV replication, to viral replication centers.[47] Poliovirus (PV) has also been reported to suppress the formation of p-bodies.[19] Deadenylation is an indispensable pre-requisite for mRNA decay and p-body formation in mammals.[48] It was found that PV infection induced cleavage of PAN3 [49], a deadenylase that when depleted, disrupts deadenylation and thus, p-body formation.[48] PV disrupts the formation of p-bodies prior to the completion of the virus replication cycle.[47] Interestingly, the dissolution of p-bodies during a PV infection is followed by the degradation of multiple proteins related to mRNA turnover.[47]

Viruses may target stress granules for a number of reasons; for example, to prevent the sequestration of viral factors into stress granules or to co-opt stress granule factors to promote virus replication.[47] Cricket paralysis virus (CrPV) inhibits stress granule formation in the early stages of infection, which may allow viral proteins and RNA to remain accessible for essential viral processes like replication and translation.[47, 50] At later stages of infection, correlating with an increase in viral protein

expression, CrPV also inhibits the formation of exogenously-induced stress granules.[47] Flaviviruses like DENV, WNV, and ZIKV have also been shown to suppress stress granule formation.[47, 51] Notably, while these flaviviruses suppressed host cell translation, viral protein synthesis remained unaffected.[51] It's been proposed that flaviviruses may recruit stress granule proteins to restrict the innate immune response or to promote virus translation or replication.[47] Likewise, Semliki Forest virus (SFV) inhibits stress granule formation and diverts RasGAP-SH3 domain binding protein 1 (G3BP1) into viral replication complexes.[47, 50]

Conversely, Hepatitis C virus (HCV) induces stress granule formation, which restricts the translation of interferon-triggered antiviral transcripts.[52] HCV also hijacks stress granule proteins, like G3BP1, to support virus replication and particle assembly.[52] While viruses have been shown to target host condensates to promote infection, many are also capable of generating viral condensates for the same purpose.

Viruses Exploit Phase Separation

Recently, there has been an influx of studies that have reported a role for phase separation in promoting DNA and RNA virus infections.[38, 53] Compared to the eukaryotic proteome, the proteome of RNA viruses is enriched with proteins containing IDRs.[54] Phase separation has been reported to be involved in all of the major steps of the viral lifecycle including viral entry and uncoating, genome replication, virion assembly and release.[55] As such, it's proposed as the phenomena behind the

formation of various viral membraneless organelles and compartments.[56] These condensates are believed to be intracellular sites that concentrate viral and host molecules to facilitate multiple virus processes.

Numerous negative strand RNA viruses have been shown to induce the formation of cytoplasmic membraneless organelles, called inclusion bodies, to carry out multiple functions to promote virus infection.[57] Influenza A virus (IAV) exploits the host aggresome machinery and nuclear import factor transportin-1 (TNPO1), an important phase separation regulator in the host, to promote the uncoating and disassembly of the IAV capsid.[55] It's been proposed that IAV whole genome assembly may take place inside viral inclusion bodies with liquid-like properties.[58, 59] Additionally, the viral transcription and replication of Rabies virus (RABV) and Respiratory syncytial virus (RSV) takes place in cytoplasmic inclusion bodies formed through phase separation.[58] Inclusion bodies have also been reported as the replication site of Vesicular stomatitis virus (VSV), Ebola virus (EBOV), Marburg virus (MARV), and Measles virus (MeV).[58] The formation of these bodies is often dependent on the expression of the viral nucleoprotein (N) and the phosphoprotein (P).[58] Viral N and P proteins often contain multiple RNA-binding domains and IDRs.[58] RABV, VSV, RSV, and MeV require N and P protein expression for the formation of inclusion bodies to facilitate viral processes and support the viral lifecycle.[58] Often, +sense RNA viruses replicate atop modified host cell membranes [60], yet +sense viruses like GRV and PEMV2 still form cytoplasmic inclusion bodies.

In contrast, +sense RNA viruses often replicate in membrane-associated compartments or atop modified host cell membranes.[17, 54, 58] HCV, DENV, and SARS-CoV-2 replication has been reported in viral factories connected to the endoplasmic reticulum (ER).[58] Semliki Forest virus (SFV) and Flock house virus (FHV) replication has been associated with viral factories attached to lysosomes and the mitochondria, respectively.[58] Despite this, cytoplasmic condensates containing viral proteins from +sense RNA viruses have been reported.[29, 31, 61] For example, the SARS-CoV-2 N protein undergoes phase separation and partitions in host stress granules under stress conditions.[62] However, viral condensates associated with +sense RNA viruses remain largely unexplored.

While investigations into protein phase separation have expanded rapidly in animal and yeast models over recent years, the study of phase separation in plants remains in its infancy. Many studies on this topic have been centered on the role of phase separation in flowering, immunity, and the stress response in plants (Figure 1.4).[63] Moreover, the study of phase separation in relation to viruses was also a newly budding field. Therefore, at the time of this work, research into the role of phase separation in plant virus infections was almost non-existent. We aimed to address this knowledge gap by demonstrating the phase separation of a plant virus movement protein and elucidating the function of viral condensates formed by a +sense RNA virus. The work herein is innovative and successfully answers several novel questions about trending scientific topics, like biomolecular phase separation. This research has provided necessary insight and knowledge to the field of virology, deepening our

understanding of virus-host interactions. Our work helps to forge a path forward by investigating the mechanics of RNA virus infections, which, over the last 100 years have caused the most global pandemics.[64]

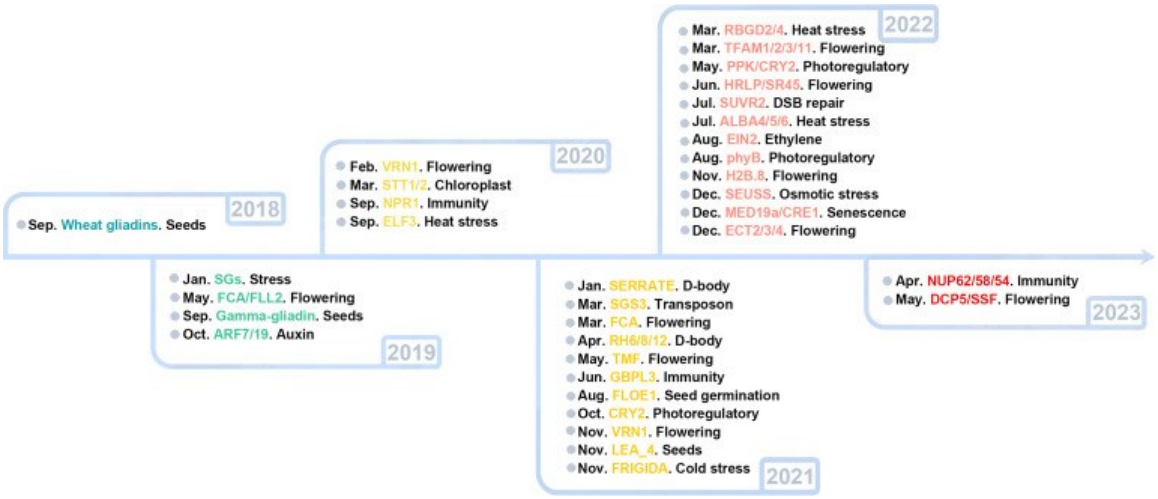

Figure 1.4 A Graphical Timeline of Phase Separation Research in Plants

This figure summarizes the work investigating phase separation in plants, beginning in 2018. This graphical timeline was reproduced with permission from Elsevier. This article was published in Plant Communications Shanghai Editorial Office in association with Cell Press, 5, Liu, Q., Liu, W., Niu, Y., Wang, T., Dong, J., Liquid–liquid phase separation in plants: Advances and perspectives from model species to crops, 100663, Copyright Elsevier 2023. https://doi.org/10.1016/j.xplc.2023.100663.[63]

CHAPTER 2

2. PHASE SEPARATION OF A PLANT VIRUS MOVEMENT PROTEIN AND CELLULAR FACTORS SUPPORT VIRUS-HOST INTERACTIONS

Adapted with permission from Brown SL, Garrison DJ, May JP. Phase separation of a plant virus movement protein and cellular factors support virus-host interactions. PLoS Pathog. 2021 Sep 20;17(9):e1009622. doi: https://doi.org/10.1371/journal.ppat.1009622. PMID: 34543360; PMCID: PMC8483311.

Chapter Summary

Both cellular and viral proteins can undergo phase separation and form membraneless compartments that concentrate biomolecules. The p26 movement protein from single-stranded, positive-sense Pea enation mosaic virus 2 (PEMV2) separates into a dense phase in nucleoli where p26 and related orthologues must interact with fibrillarin (Fib2) as a pre-requisite for systemic virus movement. Using in-vitro assays, viral ribonucleoprotein complexes containing p26, Fib2, and PEMV2 genomic RNAs formed droplets that may provide the basis for self-assembly *in planta*. Mutating basic p26 residues, arginine and lysine mutated to glycine (R/K-G), blocked droplet formation and partitioning into Fib2 droplets or the nucleolus and prevented systemic movement of a Tobacco mosaic virus (TMV) vector in *Nicotiana benthamiana*. Mutating acidic residues, aspartic acid and glutamic acid mutated to glycine (D/E-G), reduced droplet formation in vitro, increased nucleolar retention 6.5-fold, and prevented systemic movement of TMV, thus demonstrating that p26 requires

electrostatic interactions for droplet formation and charged residues are critical for nucleolar trafficking and virus movement. p26 readily partitioned into stress granules (SGs), which are membraneless compartments that assemble by clustering of the RNA binding protein G3BP following stress. G3BP is upregulated during PEMV2 infection and over-expression of G3BP restricted PEMV2 RNA accumulation >20-fold. Deletion of the NTF2 domain that is required for G3BP condensation restored PEMV2 RNA accumulation >4-fold, demonstrating that phase separation enhances G3BP antiviral activity. These results indicate that p26 partitions into membraneless compartments with either proviral (Fib2) or antiviral (G3BP) factors.

Introduction

Cellular organelles are membrane-bound compartments that are critical for eukaryotic cell function. RNA viruses frequently co-opt organelles to promote virus replication, including the endoplasmic reticulum (ER) [66], mitochondria [67], nucleus [68], and Golgi apparatus [69]. Much attention has been recently directed towards membraneless organelles that form through phase separation, which transforms a single-phase solution into a dilute phase and dense phase that concentrates biomolecules, such as proteins or RNAs.[70, 71] Proteins that undergo phase separation contain intrinsically disordered regions (IDRs) that self-associate to form oligomers.[72] Many IDR-containing proteins have RNA-recognition motifs that non-specifically bind RNA and fine-tune phase separation by controlling material exchange, shape, and rigidity of liquid droplets.[72, 73] Proteins that phase separate are often enriched in

arginine residues that promote phase separation through cation-pi interactions with aromatic contacts.[74] In addition, hydrophobic interactions can stabilize phase separations of low-complexity domains.[75]

Membraneless organelles exist as liquids, gels, or solids.[76] The most notable examples of cellular membraneless organelles are the nucleolus and cytoplasmic P-bodies.[77] Less dynamic stress granules (SGs) also form in the cytoplasm and allow host cells to repress translation and influence messenger RNA (mRNA) stability in response to various stresses.[78] SGs are visible by microscopy within minutes following stress and contain the RNA binding protein G3BP1 that self-associates to induce SG formation.[79] SGs contain a stable inner core and an outer shell that is formed by weak electrostatic and/or hydrophobic interactions.[80] The G3BP1 inner core has limited circularity and is resistant to dilution (both atypical for liquid droplets) and is surrounded by a highly dynamic shell structure.[80, 81] Interestingly, G3BP1 can have either pro-viral [82-84] or anti-viral roles [85-87] in RNA virus infection cycles.

Phase separation of viral proteins has largely been associated with negative-sense RNA viruses from the *Mononegavirales* family that form membraneless virus factories [88, 89] such as Negri bodies that form during Rabies virus infections.[57, 90, 91] In contrast, many positive-sense RNA viruses, including members of the *Tombusviridae* family, form membranous replication organelles that concentrate virus replication complexes.[92, 93] Recent work has demonstrated that the nucleocapsid (N) protein from the positive-sense SARS-CoV-2 coronavirus undergoes phase separation stimulated by the 5' end of its genomic RNA.[94, 95] N protein partitions into droplets of

heterogeneous nuclear ribonucleoproteins like TDP-43, FUS, and hnRNPA2 [96] and also interacts with G3BP1, which attenuates SG formation.[97, 98] The role of N droplet formation in the virus infection cycle is unclear but could be involved in nucleocapsid assembly and genome processing.[99] Although limited evidence for phase separation of plant virus proteins exists [100], a recent study demonstrated that Turnip mosaic virus inhibits the formation of phase-separated nuclear dicing bodies (D-bodies) that are responsible for microRNA processing and anti-viral defense.[101, 102] While these findings demonstrate cellular condensates can possess antiviral activity, examples of plant virus proteins that use phase separation to support virus-host interactions have not been reported.

Pea enation mosaic virus 2 (PEMV2) is a small (4,252 nt), positive-sense RNA plant virus belonging to the umbravirus genus in the *Tombusviridae* family. The PEMV2 long-distance movement protein p26 is required for trafficking viral RNA through the vascular system of infected plants.[103] Both p26 and the umbravirus Groundnut rosette virus (GRV) orthologue (pORF3) form large cytoplasmic granules [104-106], but also target cajal bodies in the nucleus and eventually partition in the nucleolus.[31, 107, 108] Umbravirus p26 orthologues interact with nucleolar fibrillarin, which is required for long-distance movement of the viral genomic RNA [31, 104, 108]. In addition to umbraviruses, polerovirus Potato leafroll virus (PLRV) and the satellite RNA of potexvirus Bamboo mosaic virus (satBaMV) encode proteins that also localize to the nucleolus and interact with fibrillarin to support systemic movement.[109-111] Fibrillarin forms droplets that make up the dense fibrillar component (DFC) of the nucleolus,

which shares a similar structure with SGs.[80, 112] Although the nucleolus itself is a phase separation and these plant virus proteins interact directly with fibrillarin, the role of viral protein phase separation in the infection cycle has not been investigated.

In this report, we demonstrate that PEMV2 p26 assembles viscous condensates in vivo with low intra-droplet diffusion (i.e., droplets are poorly dynamic). Viral ribonucleoprotein (vRNP) complexes containing p26, fibrillarin, and PEMV2 genomic RNAs were reconstituted in vitro through phase separation, which we hypothesize recapitulates the in vivo event necessary for systemic trafficking. Charged residues played critical roles in p26 droplet formation, nucleolar localization, and movement of a TMV vector, suggesting that phase separation and virus movement are connected. Finally, p26 partitions into SGs, and G3BP over-expression restricts PEMV2 RNA accumulation >20-fold. A G3BP mutant incapable of forming a dense phase only reduced PEMV2 RNA accumulation by 5-fold, suggesting that phase separation is involved in the antiviral host response.

Results

p26 forms poorly dynamic condensates in vivo. To visualize and characterize the material properties of p26 granules in vivo, green fluorescent protein (GFP) was fused to the C-terminus of full-length p26 and expressed from the Cauliflower mosaic virus (CaMV) 35S promoter (Figure 2.1A) following agroinfiltration of *Nicotiana benthamiana* leaves. To maximize transient gene expression, the p14 RNA silencing suppressor from Pothos latent virus [113] was included in all infiltrations

for this study. GFP expressed from the CaMV 35S promoter failed to form granules and was evenly distributed throughout the cytoplasm and nucleus of the cell (i.e., outside of the large vacuole that comprises most of the cellular space) (Figure 2.1B, Left). In contrast, $p26_{WT}$ formed large cytoplasmic granules (Figure 2.1B, Right). To probe intra-droplet dynamics, we used fluorescence recovery after photobleaching (FRAP) assays.[114] If p26 granules are highly dynamic liquid droplets, then FRAP recovery should be rapid and complete. Conversely, if p26 forms solid aggregates, no fluorescence recovery was expected. $p26_{WT}$ granules recovered nearly 50% by 30 seconds post-bleaching (Figure 2.1C), indicating that these p26 droplets had measurable fluidity. However, since $p26_{WT}$ failed to fully recover, p26 appears to form viscous condensates in vivo with poor intra-droplet dynamics.

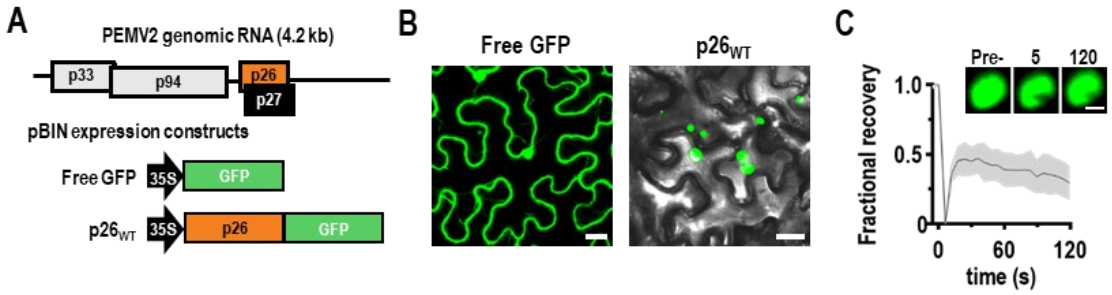

Figure 2.1 p26 forms poorly dynamic condensates in vivo

(**A**) Genomic organization of the single-stranded positive-sense RNA genome of PEMV2. Free GFP and p26 C-terminally fused with GFP ($p26_{WT}$) were expressed from binary expression plasmids under the constitutive CaMV 35S promoter. (**B**) Free GFP or $p26_{WT}$ were agroinfiltrated alongside the p14 RNA silencing suppressor in *N. benthamiana* and imaged at 2 dpi using confocal microscopy (488 nm). Note that the majority of plant mesophyll cells is taken up by a single large vacuole. Differential interference contrast (DIC) microscopy was used for $p26_{WT}$ to visualize cell borders. Bar scale: 20 µm. (**C**) FRAP analyses were performed by photobleaching cytoplasmic condensates and monitoring fluorescence recovery at 5 s intervals. A representative $p26_{WT}$ condensate is shown before photobleaching, immediately following photobleaching (5 s), and at 120 s. Bar scale 5 µm. Average FRAP intensity is shown from seven FRAP experiments and shaded area represents standard deviations.

p26 contains an intrinsically disordered region (IDR) and phase separates via electrostatic interactions. Since IDRs typically drive phase separation [115], we subjected p26 to the IDR prediction program IUPred [116], which identified an arginine-rich disordered region spanning amino acids 1-132 (Figure 2.2A and B). The same region was also predicted to have the highest propensity to phase separate using the catGRANULE algorithm (Figure 2.2C).[117] To determine if the identified p26 IDR drives droplet formation, IDR_{WT} or amino acids 133-226 (C-term) along with N-terminal histidine tags or the tag alone was fused to the N-terminus of GFP, and proteins purified after expression in *E. coli.* were assessed for size and purity by SDS-PAGE (Figure 2.2D). To assay for induction of phase separation, proteins were combined with 10% PEG-8000 and droplet formation was observed by confocal microscopy and by measuring solution turbidity (OD_{600}). As expected, IDR_{WT} assembled into condensed droplets as observed by both confocal microscopy (Figure 2.2E) and turbidity assays (Figure 2.2F). In contrast, both free GFP and C-term remained in a single phase (Figure 2.2E and F). N-terminal histidine tags did not influence IDR_{WT} phase separation propensity, particle size, or resistance to 1,6-hexanediol that selectively dissolves liquid condensates[118] (Figure S2.1, Appendix). However, FRAP recovery of IDR_{WT} dramatically increased following His-tag removal suggesting that the histidine tracts influenced droplet dynamics in vitro (Figure S2.1, Appendix).

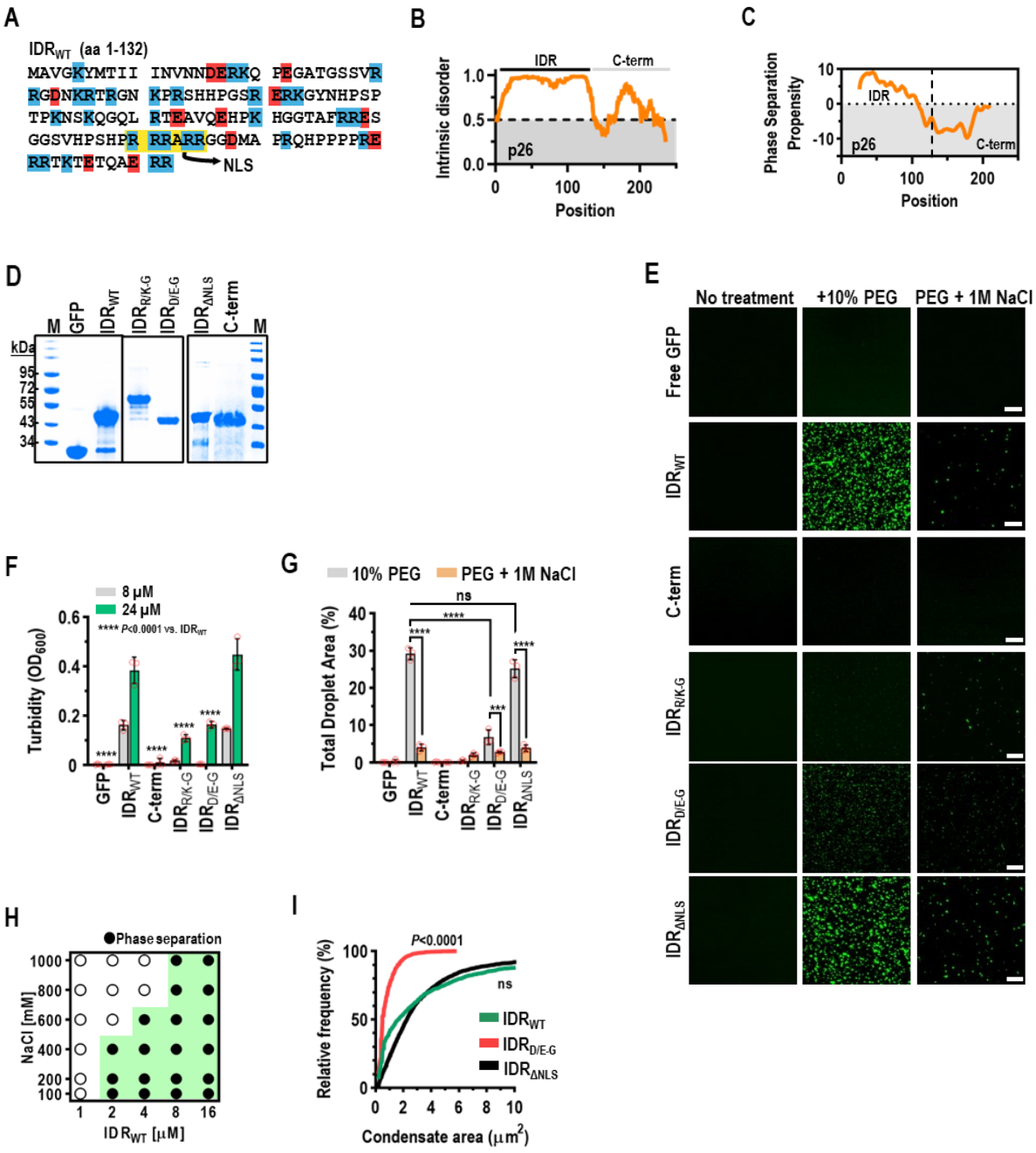
A
IDR$_{WT}$ (aa 1-132)
MAVGKYMTII INVNNDERKQ PEGATGSSVR
RGDNKRTRGN KPRSHHPGSR ERKGYNHPSP
TPKNSKQGQL RTEAVQEHPK HGGTAFRREG
GGSVHPSHPR RRARRGGDMA PRQHPPPPRE
RRTKTETQAE RR
NLS
B
IDR
C-term
Intrinsic disorder
p26
Position
C
Phase Separation Propensity
IDR
p26
C-term
Position
D
M
GFP
IDR$_{WT}$
IDR$_{R/K-G}$
IDR$_{D/E-G}$
IDR$_{\Delta NLS}$
C-term
M
kDa
95
72
55
43
34
E
No treatment
+10% PEG
PEG + 1M NaCl
Free GFP
IDR$_{WT}$
C-term
IDR$_{R/K-G}$
IDR$_{D/E-G}$
IDR$_{\Delta NLS}$
F
8 μM
24 μM
**** P<0.0001 vs. IDR$_{WT}$
Turbidity (OD$_{600}$)
G
10% PEG
PEG + 1M NaCl
ns
Total Droplet Area (%)
H
Phase separation
NaCl [mM]
IDR$_{WT}$ [μM]
I
P<0.0001
ns
IDR$_{WT}$
IDR$_{D/E-G}$
IDR$_{\Delta NLS}$
Relative frequency (%)
Condensate area (μm^2)

Figure 2.2 p26 is intrinsically disordered and phase separates through electrostatic interactions

(**A**) The p26 IDR (amino acids 1–132) is shown with highlighted residues corresponding to basic (blue) or acidic (red) residues. The conserved nuclear localization signal (NLS) is highlighted in yellow. (**B**) Graphical representation of predicted intrinsic disorder in p26 using IUPRED.[119] (**C**) Graphical representation of predicted phase separation propensity within p26 using the catGRANULE algorithm.[120] (**D**) N-terminal His-tagged recombinant proteins were analyzed by SDS-PAGE to assess size and purity. Proteins were stained using Coomassie Blue. Marker (M) sizes are shown in kilodaltons (kDa). $IDR_{R/K\text{-}G}$ migrated more slowly than expected both *in vitro* and *in vivo* (see Fig 6B). (**E**) In vitro droplet formation was visualized by confocal microscopy. Eight micromolar protein was used for all assays and 10% PEG-8000 was added as a crowding agent (Middle panels). One molar NaCl was added to disrupt electrostatic interactions (Right panel). Bar scale: 20 μm. Images in all panels are representative of at least two independent experiments. (**F**) Turbidity assays (OD_{600}) using either 8 μM or 24 μM protein were performed for all constructs. **** $P<0.0001$ by two-way ANOVA with Dunnett's multiple comparisons test vs. IDR_{WT}. Error bars denote standard deviations and individual data points (red circles) represent three biological replicates. (**G**) Total droplet areas (%) were measured from confocal images using ImageJ. Error bars denote standard deviations and red circles represent three 20x fields for each assay. *** $P<0.001$, **** $P<0.0001$, ns: not significant using two-way ANOVA with Sidak's multiple comparisons test. (**H**) Phase diagram for IDR_{WT} over a range of protein and NaCl concentrations. Results are representative of two independent experiments. (**I**) Mean condensate sizes for IDR mutants (excluding $IDR_{R/K\text{-}G}$) were plotted by cumulative distribution frequency. Particle sizes were measured from three representative 20x fields using ImageJ. *P* values represent results from two-tailed Mann-Whitney tests compared to IDR_{WT}. ns: not significant.

Electrostatic interactions that drive self-assembly and droplet formation can be inhibited by high salt concentrations.[121] Confocal microscopy revealed significantly reduced phase separation of IDR_{WT} in the presence of 1 M NaCl (Figure 2.2E), which was confirmed by comparing total droplet areas (%) from three representative 20x fields for each condition (Figure 2.2G). These results support p26 assembling in a dense phase through electrostatic interactions. To determine the saturation concentration (C_{sat}) of IDR_{WT} and further investigate NaCl-mediated reduction in droplet formation, a phase diagram was generated using confocal microscopy. The apparent C_{sat} was 2 μM and IDR_{WT} was sensitive to NaCl in a dose-responsive manner as 600 mM and 800 mM NaCl blocked droplet formation of 2 μM and 4 μM IDR_{WT}, respectively (Figure 2.2H).

Deletion of IDR sequence 5'-RRRARR-3' (amino acids 100-105), which comprises a conserved nuclear localization signal (NLS)[122] and 16% of the basic residues within the IDR, did not affect droplet formation (Figure 2.2E-G), demonstrating that the NLS is not required for phase separation. However, when all basic or acidic residues in IDR_{WT} were mutated to glycine ($IDR_{R/K-G}$ or $IDR_{D/E-G}$, respectively), $IDR_{R/K-G}$ failed to phase separate while $IDR_{D/E-G}$ showed significantly reduced phase separation compared to IDR_{WT} when examined by turbidity assays (Figure 2.2F), total droplet area (Figure 2.2G), and mean condensate size (Figure 2.2I). At higher concentrations (24 μM), $IDR_{R/K-G}$ formed non-uniform aggregates with significantly reduced circularity compared to IDR_{WT} and $IDR_{D/E-G}$ droplets (Figure S2.2, Appendix). When all potential cation-pi or hydrophobic interactions were disrupted by

mutating all arginines to lysines ($IDR_{R\text{-}K}$) or all hydrophobic residues to serine ($IDR_{VLIMFYW\text{-}S}$), respectively, total droplet areas, turbidities, and mean condensate sizes were unchanged compared to IDR_{WT}, demonstrating that cation-pi and hydrophobic interactions are not required for condensate formation (Figure S2.3, Appendix). Together, these results support the N-terminal IDR of p26 inducing phase separation through electrostatic interactions.

Charged residues govern p26 nucleolar partitioning. Umbravirus movement proteins must access the nucleolus to support systemic virus trafficking.[31] Nucleolar partitioning of full-length $p26_{WT}$, $p26_{R/K\text{-}G}$, $p26_{\Delta NLS}$, or $p26_{D/E\text{-}G}$ was examined by expressing proteins from a CaMV 35S promoter in *N. benthamiana* (via agroinfiltration) and observing localization in cells with DAPI-stained nuclei. As with ORF3 orthologues [31, 32, 104, 122], $p26_{WT}$ was observed in nuclear bodies (e.g., the nucleolus) in addition to forming cytoplasmic granules (Figure 2.3A). The percentage of nuclear granules was calculated by manually counting nuclear granules from six 20x fields and dividing by the total granule count calculated using the ImageJ “analyze particles” function in the 488 nm channel. Approximately 5% of $p26_{WT}$ granules were nuclear and coincided with published observations for the related GRV pORF3.[122] $p26_{R/K\text{-}G}$ did not form granules but instead was diffusely expressed throughout the cytoplasm and failed to partition in the nucleolus (Figure 2.3A). $p26_{\Delta NLS}$ resulted in strictly cytoplasmic localization of p26 granules (Figure 2.3A and B). $p26_{D/E\text{-}G}$ formed cytoplasmic granules similar to those of $p26_{WT}$ (Figure 2.3A), despite reduced phase

separation of $IDR_{D/E-G}$ in vitro. However, the portion of $p26_{D/E-G}$ granules that were nuclear (33%) was 6.5-fold higher compared to $p26_{WT}$ (Figure 2.3B), suggesting that the net charge of p26 may be influencing nucleolar localization.

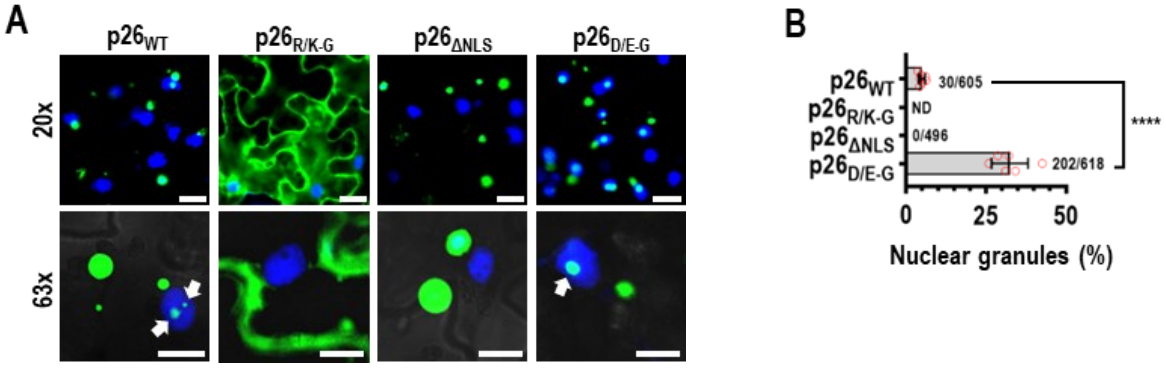

Figure 2.3 Charged residues govern p26 nucleolar partitioning

(**A**) p26-GFP fusions were expressed from the CaMV 35S promoter in *N. benthamiana* leaves following agroinfiltration. Prior to imaging, leaves were infiltrated with 5 µg/mL DAPI to stain nuclei. 20x and 63x fields are shown. Arrows denote p26 partitioned inside nuclear bodies (e.g. nucleolus). Bar scale: Top 20 µm; Bottom 10 µm. Images in all panels are representative of two independent experiments. (**B**) Nuclear granules were manually counted from six 20x fields across three biological replicates. Total granule counts (>2 μm^2 in size) were counted using the ImageJ "analyze particles" tool. Error bars denote standard deviations and data points (red circles) denote individual 20x fields. ****P<0.0001 unpaired t test, ND not detected.

p26 phase separation is required for partitioning into Fib2 droplets. Fibrillarin (Fib2), which makes up the dense fibrillar component of the nucleolus [123], is required for systemic trafficking of umbravirus vRNPs.[107, 108] The N-terminus of *Arabidopsis thaliana* Fib2 (amino acids 7-77) comprises an intrinsically disordered glycine- and arginine-rich (GAR) domain ($Fib2_{GAR}$) (Figure 2.4A) that is common to fibrillarin across eukaryotes.[124] To determine whether $Fib2_{GAR}$ is sufficient for Fib2 phase separation, histidine-tagged full-length Fib2 ($Fib2_{FL}$) or $Fib2_{GAR}$ were fused to the N-terminus of mCherry and purified from *E. coli* for in vitro phase separation assays (Figure 2.4B). mCherry alone did not form droplets in the presence of 10% PEG-8000 or under high-salt conditions (Figure 2.4C and D), whereas $Fib2_{FL}$ and $Fib2_{GAR}$ readily formed droplets under crowding conditions (Figure 2.4C). In the presence of 1 M NaCl, $Fib2_{FL}$ droplets, but not those of $Fib2_{GAR}$ were resistant to high salt (Figure 2.4C and D). These results indicate that the GAR domain is sufficient to form Fib2 droplets through electrostatic interactions and is consistent with findings using mammalian and *Caenorhabditis elegans* fibrillarin.[112, 125, 126] In addition, unlike $Fib2_{GAR}$, $Fib2_{FL}$ condensates are either not strictly dependent on electrostatic interactions or $Fib2_{FL}$ can form salt-resistant aggregates.

Fib2 functions as a scaffold for recruiting client proteins into the nucleolus and scaffolds are typically present in excess relative to clients.[127, 128] During viral infection, p26 is thought to partition into already formed nucleolar Fib2 droplets [112] and the GRV p26 ortholog can directly interact with $Fib2_{GAR}$.[32] Using a 1:6 molar ratio of IDR_{WT} and $Fib2_{GAR}$, IDR_{WT} readily partitioned into pre-formed $Fib2_{GAR}$ droplets in vitro (Figure

2.4E, Left). When $IDR_{R/K\text{-}G}$ was added to pre-formed $Fib2_{GAR}$ droplets, $IDR_{R/K\text{-}G}$ remained in the bulk phase and was excluded from $Fib2_{GAR}$ droplets (Figure 2.4E, Right, white arrows). These results demonstrate that p26 phase separation is critical for partitioning into Fib2 droplets, which could play a role in PEMV2 movement.

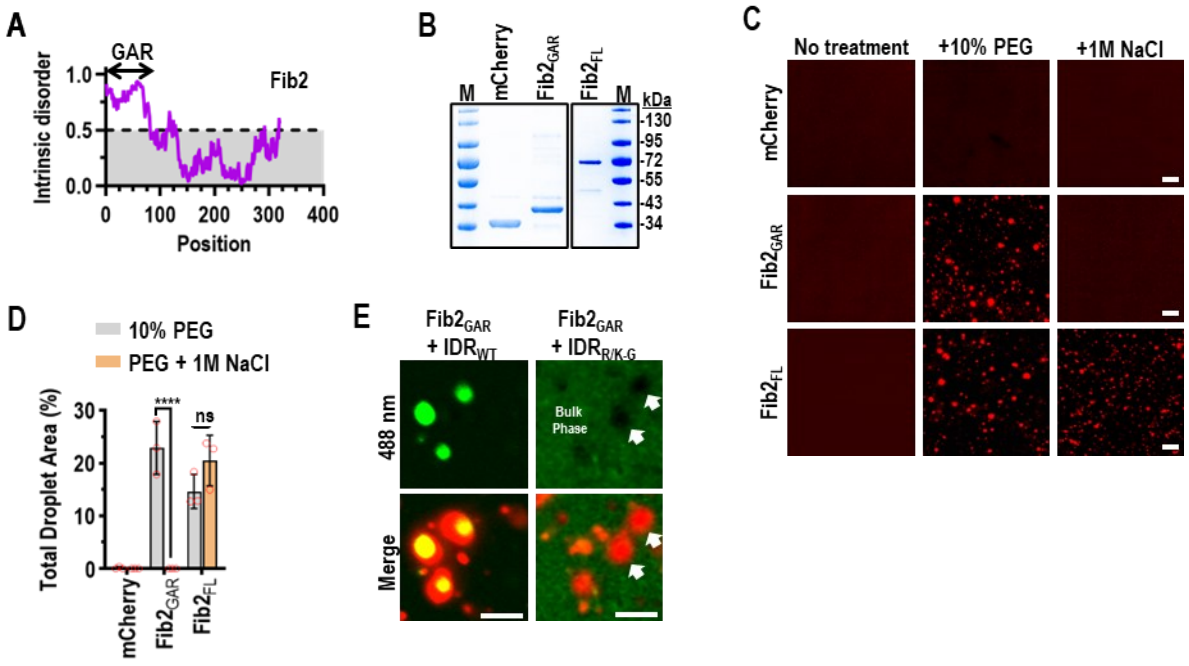

Figure 2.4 p26 phase separation is required for partitioning into Fib2 droplets

(**A**) Graphical representation of predicted intrinsic disorder in *A. thaliana* Fib2 using IUPRED.[116] The N-terminal glycine and arginine rich (GAR) domain is labelled. (**B**) The Fib2 GAR domain ($Fib2_{GAR}$) and full-length Fib2 ($Fib2_{FL}$) were fused to mCherry and purified from *E. coli* and analyzed by SDS-PAGE. Proteins were Coomassie stained and molecular weight (kDa) marker is shown. (**C**) mCherry, $Fib2_{GAR}$, and $Fib2_{FL}$ were examined by confocal microscopy after inducing phase separation with 10% PEG-8000 alone or in the presence of 1 M NaCl. Eight micromolar protein was used for all assays. Bar scale: 20 µm. Experiments were repeated. (**D**) Total droplet areas of $Fib2_{GAR}$ and $Fib2_{FL}$ were measured using ImageJ. Error bars denote standard deviations and data points (red circles) represent representative 20x fields (3 total) for each condition. **** $P<0.0001$, ns: not significant using two-way ANOVA with Sidak's multiple comparisons test. (**E**) $Fib2_{GAR}$ droplets were pre-formed using 24 µM protein before the addition of 4 µM IDR_{WT} or $IDR_{R/K-G}$. Sorting of IDR_{WT} to Fib2 droplets was observed by confocal microscopy. White arrows indicate exclusion of $IDR_{R/K-G}$ from pre-formed $Fib2_{GAR}$ droplets. Bar scale 10 µm. Images in all panels are representative of two independent experiments.

vRNPs required for systemic trafficking can be reconstituted via phase separation. Movement-competent umbravirus vRNPs consist of Fib2, p26, and the genomic RNA (gRNA).[32] Therefore, we sought to determine whether vRNPs could be re-constituted in vitro through phase separation. To determine whether full-length PEMV2 gRNA was sorted to Fib2 droplets, Cy5-labelled PEMV2 gRNA was mixed with pre-formed $Fib2_{GAR}$ or $Fib2_{FL}$ droplets at a 1:500 RNA:Fib2 molar ratio (this ratio was used since earlier work determined that umbravirus RNAs were saturated by protein interactors under these conditions [105, 108]). PEMV2-Cy5 gRNA was not efficiently sorted into $Fib2_{GAR}$ droplets when visualized by confocal microscopy (Figure 2.5A) or measured using Mander's Overlap Coefficient (MOC, Figure 2.5B), which is consistent with earlier findings that determined $Fib2_{GAR}$ does not bind RNA.[124, 125] In contrast, $Fib2_{FL}$ captured a significantly higher portion of PEMV2-Cy5 gRNA demonstrating that PEMV2 gRNA can efficiently partition in full-length Fib2 droplets (Figure 2.5A and B). Since p26 must also associate with viral RNAs, PEMV2-Cy5 gRNA was mixed with pre-formed IDR_{WT} droplets using a 1:500 ratio of RNA to protein. Approximately 50% of the IDR_{WT} signal spatially overlapped the PEMV2-Cy5 signal when visualized by confocal microscopy and quantified by MOC (Figure 2.5C and D). Partitioning of PEMV2 gRNA into IDR_{WT} droplets was not unique to PEMV2 since the distantly related carmovirus Turnip crinkle virus (TCV) and non-viral Renilla luciferase (RLuc) RNAs also sorted into IDR_{WT} droplets with equal propensity (Figure 2.5C and D). Importantly, the N-terminal His-tag of IDR_{WT} did not influence sorting of RNAs into droplets (Figure S2.1, Appendix). Finally, equimolar amounts of $Fib2_{FL}$ and

IDR_{WT} (8 μM each) were mixed with PEG, followed by the addition of 16 nM PEMV2-Cy5 gRNA, which resulted in the formation of droplets containing IDR_{WT}, $Fib2_{FL}$, and PEMV2 gRNA (Figure 2.5E). Together, these findings suggest that the formation of vRNPs *in planta* may occur in a dense phase with resident p26, Fib2, and viral RNAs.

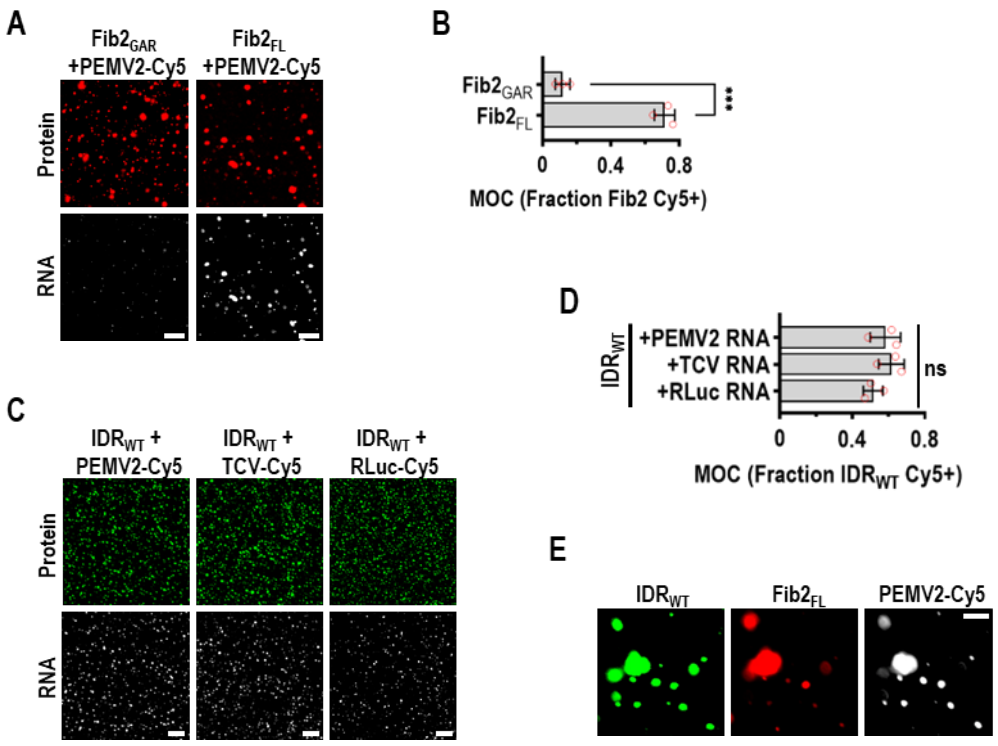

Figure 2.5 vRNPs required for systemic trafficking can be reconstituted in vitro via phase separation

(**A**) $Fib2_{GAR}$ and $Fib2_{FL}$ droplets were pre-formed prior to the addition of PEMV2-Cy5 gRNAs at a 1:500 RNA:protein molar ratio. Sorting of Cy5-labelled RNAs into Fib2 droplets was monitored using confocal microscopy. Bar scale: 20 μm. (**B**) The fraction of $Fib2_{GAR}$ or $Fib2_{FL}$ signal that was positive for Cy5-labelled RNA was determined by MOC analysis using EzColocalization.[129] Error bars denote standard deviations and individual data points (red circles) represent individual 20x fields (3 total) for each condition. ***P<0.001 unpaired t test. (**C**) IDR_{WT} droplets were pre-formed prior to the addition of PEMV2-Cy5 gRNA, TCV-Cy5 gRNA, or RLuc-Cy5 RNA. Bar scale: 20 μm. (**D**) The fraction of IDR_{WT} signal that was positive for Cy5-labelled RNA was determined by MOC analysis. ns: not significant by unpaired t test. Error bars denote standard deviations. Three 20x fields were quantified for each condition (red circles). (**E**) IDR_{WT}, $Fib2_{FL}$, and PEMV2-Cy5 gRNA were mixed under crowding conditions. Bar scale: 10 μm. Images in all Fig 5 panels are representative of at least two independent experiments.

Phase separation-deficient p26 mutants fail to systemically traffic a virus vector. p26 protects PEMV2 subgenomic RNA from nonsense-mediated decay.[106] Therefore, it is required for efficient PEMV2 RNA replication in single cells.[28] Thus, it is difficult to distinguish the effects of p26 mutations on RNA replication and virus movement. To separate these two functions, we assayed if p26 mutants could support movement of a heterologous viral RNA in *N. benthamiana*. The TMV TRBO vector contains a coat protein (CP) deletion that allows cell-to-cell movement but not systemic movement [130], which can be rescued by umbravirus ORF3 proteins expressed *in trans* or from a subgenomic promoter.[103, 131] p26 can also systemically move TRBO when expressed as a GFP-fusion, which allows for visual monitoring of virus movement.[106]

Local infections were established following agroinfiltration of *N. benthamiana* plants (4th leaf stage) using TRBO vectors expressing either free GFP, p26$_{WT}$, p26$_{R/K-G}$, or p26$_{D/E-G}$ (Figure 2.6A). High levels of free GFP and lower levels of wild-type or mutant p26 were observed at 4 days post-infiltration (dpi) by visual fluorescence and western blotting using anti-GFP antibodies (Figure 2.6B). Localization patterns of p26$_{WT}$ and p26$_{D/E-G}$ were unchanged when expressed from either a 35S promoter or from the TRBO vector and supported the previous finding that p26$_{D/E-G}$ granules were significantly enriched in nuclei compared to p26$_{WT}$ during virus infection (Figure 2.6C). Systemic movement of TRBO expressing p26$_{WT}$ was visually apparent by 14 dpi and was confirmed by RT-PCR whereas TRBO did not move systemically when expressing free GFP (Figure 2.6D). p26$_{R/K-G}$, which did not phase separate or enter

the nucleolus, was unable to support TRBO movement (Figure 2.6D). Surprisingly, $p26_{D/E-G}$ also failed to support TMV movement despite the ability of $IDR_{D/E-G}$ to form droplets (albeit less efficiently than IDR_{WT}) and partition into the nucleolus. One possibility is that increased nucleolar retention of $p26_{D/E-G}$ contributed to the block in systemic movement, which would imply that nucleolar and virus trafficking by p26 is a tightly regulated process. Together, these data suggest that p26 phase separation, nucleolar partitioning, and virus movement are connected and co-dependent on charged residues. Although deletion of the TMV CP was previously reported to block systemic movement of the TRBO vector [130], we routinely observed systemic trafficking of TRBO-GFP after 3 weeks (Figure S2.4, Appendix). However, TRBO-GFP was restricted to the petiole and midrib of systemic leaves whereas TRBO-$p26_{WT}$ spread throughout the veins and invaded the lamina (Figure S2.4, Appendix).

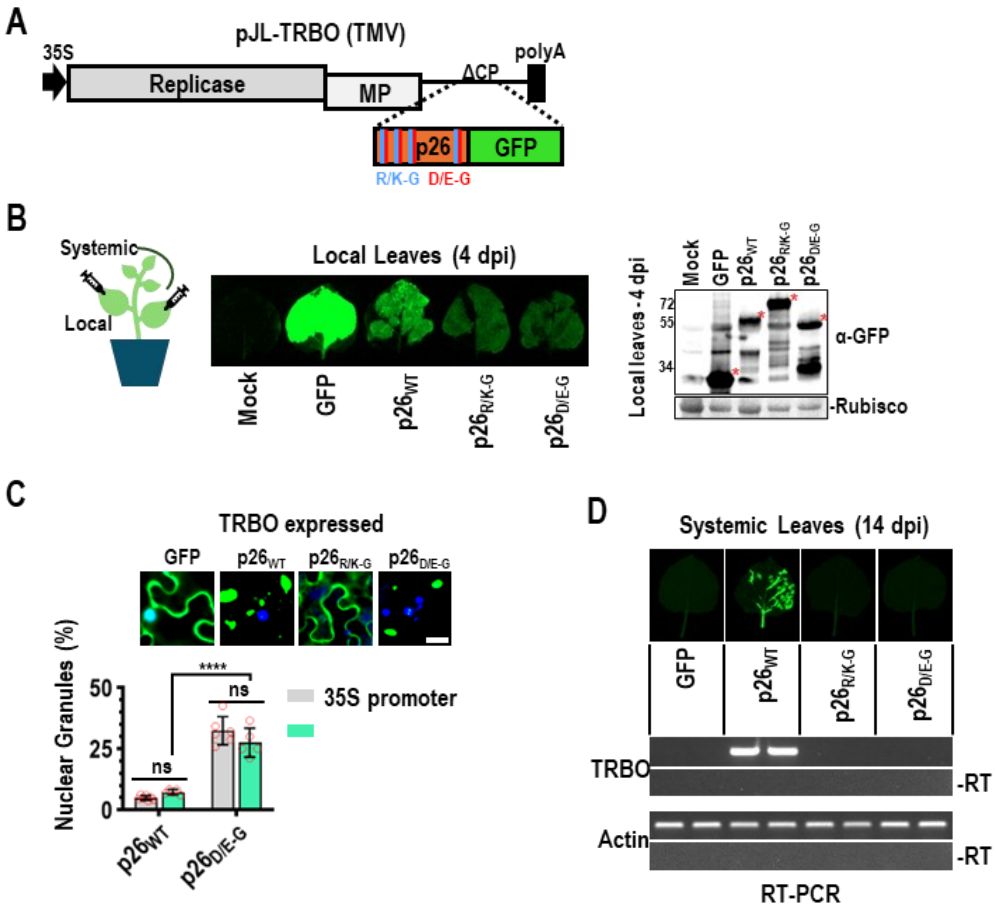
A
pJL-TRBO (TMV)
35S
Replicase
MP
ACP
polyA
p26
GFP
R/K-G
D/E-G
B
Systemic
Local
Local Leaves (4 dpi)
Mock
GFP
p26WT
p26R/K-G
p26D/E-G
Local leaves - 4 dpi
72
55
34
α-GFP
-Rubisco
C
TRBO expressed
GFP
p26WT
p26R/K-G
p26D/E-G
Nuclear Granules (%)
50
25
0
****
ns
ns
35S promoter
p26WT
p26D/E-G
D
Systemic Leaves (14 dpi)
GFP
p26WT
p26R/K-G
p26D/E-G
TRBO
-RT
Actin
-RT
RT-PCR

Figure 2.6 Phase separation-deficient p26 mutants fail to systemically traffic a virus vector

(**A**) The TMV-derived TRBO vector lacks CP and is severely impaired in systemic trafficking. Free GFP, $p26_{WT}$, $p26_{R/K\text{-}G}$, and $p26_{D/E\text{-}G}$ GFP-fusions were expressed from TRBO after establishing local infections via agroinfiltration (**B**) GFP-fusion proteins were visualized and detected in local leaves at 4 dpi by UV exposure (Left) or western blotting (Right). Pooled samples from 3 biological replicates were used for western blotting. Rubisco serves as a loading control. Red asterisks denote free GFP or GFP-fusion bands. (**C**) Localization patterns of free GFP, $p26_{WT}$, $p26_{R/K\text{-}G}$, and $p26_{D/E\text{-}G}$ in TRBO-infected leaves. Nuclear $p26_{WT}$ or $p26_{D/E\text{-}G}$ granules were counted from five 20x fields across three biological replicates and divided by the total number of granules (counted with ImageJ) to calculate a percentage (%). Bar scale: 20 μm. Results were compared with $p26_{WT}$ or $p26_{D/E\text{-}G}$ expressed from the duplicated 35S promoter (Figure 3B data is included for comparison). Error bars denote standard deviations and data points (red circles) represent individual 20x fields. ns not significant by multiple unpaired t tests. ****P<0.0001 unpaired t test. (**D**) Systemic leaves were imaged at 14 dpi. RT-PCR was used to detect the TRBO vector or actin as a control. -RT: No reverse transcriptase controls. Two pools of 3–4 leaves are shown for each construct. Results are representative of three independent experiments consisting of at least 4 plants/construct.

p26 sorts into G3BP phase separations that restrict PEMV2 accumulation. Since SGs can have both pro-viral and anti-viral roles in RNA virus infection cycles, we investigated whether p26 could partition in G3BP SGs. A nuclear transport factor 2 (NTF2) protein with RNA recognition motif (RRM) from *A. thaliana* functions as a G3BP-like SG nucleator in plants [132] (Figure 2.7A). As previously demonstrated by Krapp et. al. [132], RFP-tagged G3BP displays a diffuse cytoplasmic expression pattern in *N. benthamiana* under no stress but forms cytoplasmic SGs after heat shock (Figure 2.7B). In mammals, the N-terminal NTF2 domain is required for both G3BP phase separation and recruitment to SGs [133, 134] and here ΔNTF2 failed to form SGs after heat shock (Figure 2.7B). During co-expression of $p26_{WT}$ and G3BP from 35S promoters, p26 partitioned into SGs following heat shock as visualized by confocal microscopy (Figure 2.7B, white arrows).

To determine whether p26 partitions into SGs during a viral infection, G3BP was agroinfiltrated into *N. benthamiana* plants systemically infected with TRBO-$p26_{WT}$ (Figure 2.7C). p26 condensates co-localize with G3BP demonstrating that p26 and G3BP can share phase separations during an authentic viral infection (Figure 2.7C). When native G3BP expression was measured by RT-qPCR at 3 dpi in PEMV2-infected *N. benthamiana* leaves, a 61% increase in expression was observed during infection that could be part of an anti-viral host response (Figure 2.7D). To confirm that G3BP has an inhibitory effect on PEMV2 accumulation, G3BP was co-infiltrated with PEMV2 and the p14 silencing suppressor into *N. benthamiana*. At 3 dpi, PEMV2 accumulation was reduced >20-fold by G3BP over-expression, demonstrating that

G3BP exerts strong anti-viral activity (Figure 2.7E). Virus accumulation was partially restored (only 5-fold inhibition) during overexpression of ΔNTF2 indicating that phase separation by G3BP is required for maximal anti-viral activity (Figure 2.7E).

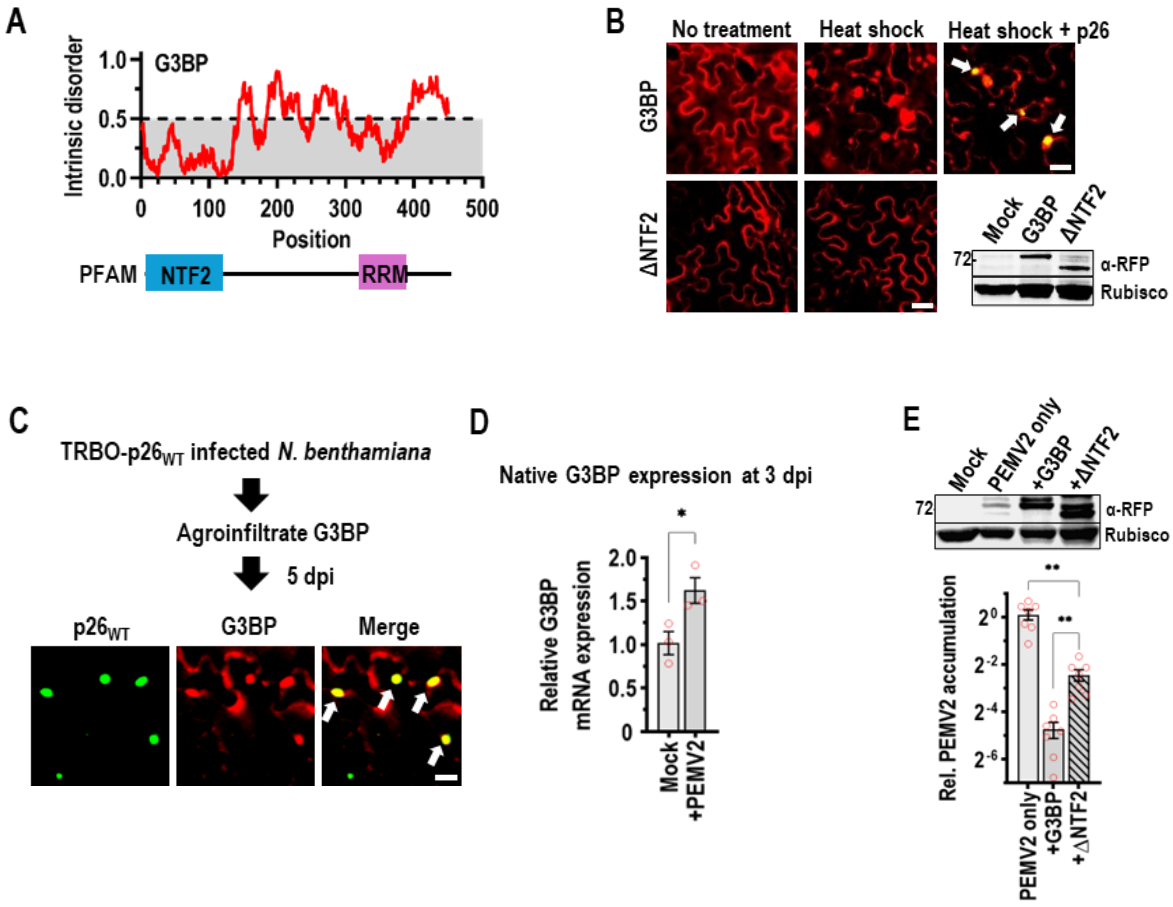
A
Intrinsic disorder
1.0
0.5
0.0
G3BP
0
100
200
300
400
500
Position
PFAM
NTF2
RRM
B
No treatment
Heat shock
Heat shock + p26
G3BP
ΔNTF2
Mock
G3BP
ΔNTF2
72
α-RFP
Rubisco
C
TRBO-p26WT infected N. benthamiana
Agroinfiltrate G3BP
5 dpi
p26WT
G3BP
Merge
D
Native G3BP expression at 3 dpi
Relative G3BP mRNA expression
2.0
1.5
1.0
0.5
0
*
Mock
+PEMV2
E
Mock
PEMV2 only
+G3BP
+ΔNTF2
72
α-RFP
Rubisco
Rel. PEMV2 accumulation
2^0
2^-2
2^-4
2^-6
**
**
PEMV2 only
+G3BP
+ΔNTF2

Figure 2.7 p26 is sorted into G3BP phase separations that restrict PEMV2 accumulation

(**A**) Graphical representation of predicted intrinsic disorder in *A*. *thaliana* G3BP using IUPRED.[116] G3BP contains an N-terminal NTF2 domain and C-terminal RNA Recognition Motif (RRM). (**B**) Following agroinfiltration, G3BP or ΔNTF2 expression patterns were visualized at 3 dpi in the absence of stress or after heat shock. During co-expression, p26 partitioning into G3BP SGs was observed following heat shock (White arrows). Scale bar: 20 μm. Inset shows western blot using anti-RFP antibodies to detect full-length G3BP and ΔNTF2. Rubisco was used as a loading control. Results represent two independent experiments. (**C**) G3BP was agroinfiltrated into *N*. *benthamiana* plants systemically infected with TRBO-p26$_{WT}$. Confocal microscopy was used to observe co-localization (White arrows) between p26 and G3BP during virus infection. Scale bar: 20 μm. Results are representative of two independent experiments. (**D**) Native G3BP expression was measured in Mock- or PEMV2-infected *N*. *benthamiana* at 3 dpi by RT-qPCR. The agroinfiltrated p14 RNA silencing suppressor was used as a reference gene. Data is from three biological replicates (red circles). *P<0.05; student's t-test. Bars denote standard error. (**E**) PEMV2 was agroinfiltrated alone, or alongside either G3BP or ΔNTF2 (both tagged with RFP). Western blot confirmed expression of G3BP and ΔNTF2 (top). RT-qPCR was used to measure PEMV2 gRNA accumulation and represents 7 biological replicates from 2 independent experiments (red circles, Bottom). Bars denote standard error. Brown-Forsythe and Welch ANOVA with multiple comparisons was used to determine if observed differences were significant. ** P<0.01.

Discussion

Our study demonstrates that p26 forms viscous droplets in vivo that fail to recover more than 50% in FRAP assays suggesting that intra-droplet dynamics are poor. Using vitro assays, we determined that the N-terminal IDR of p26 drives phase separation through electrostatic interactions since droplet formation was significantly reduced in the presence of high-salt. Furthermore, mutation of all basic residues to glycine (R/K-G), prevented p26 droplet formation both in vitro and in vivo. $p26_{R/K-G}$ was also unable to systemically move a TMV vector lacking CP but it remains unclear whether the block in systemic movement was due to the inability of $p26_{R/K-G}$ to phase separate or to enter the nucleolus, or a combination of both. Since p26 must interact with Fib2 in phase-separated nucleoli to support virus movement [32], we also investigated whether IDR_{WT} or $IDR_{R/K-G}$ could partition in pre-formed Fib2 droplets. Unlike IDR_{WT}, $IDR_{R/K-G}$ remained in the bulk-phase and was excluded from Fib2 droplets suggesting that the ability of p26 to assemble in a dense phase is important for interacting with Fib2.

While mutation of acidic residues (D/E-G) did not abolish phase separation *in vitro*, phase separation was significantly reduced compared to wild-type as measured by turbidity, total droplet area, and mean droplet size. Phase separation of arginine-rich peptides can occur through charge repulsion in the presence of buffer counteranions or RNAs [135, 136], which could explain how arginine-rich $p26_{D/E-G}$ forms droplets. Nucleolar retention of $p26_{D/E-G}$ granules was 6.5-fold higher compared to $p26_{WT}$, which might have resulted from increased protein net charge ($p26_{D/E-G}$ at pH

7.4 is +36 compared to +14 for $p26_{WT}$). These findings support earlier work showing that nucleolar localization of cellular and viral proteins was dependent on the overall positive charge.[137, 138] Surprisingly, $p26_{D/E-G}$ failed to support movement of a TMV vector, which may have resulted from increased nucleolar retention.

SGs that are assembled by self-association and phase separation of G3BP can support or restrict RNA virus replication.[133, 134] Seven *A. thaliana* G3BP-like candidates have been identified [139] containing an N-terminal NTF2 domain that is required for phase separation of mammalian G3BP1.[134] G3BP expression was upregulated during PEMV2 infection suggesting that G3BP could be expressed as part of a concerted host response to infection. We determined that PEMV2 RNA accumulation was severely restricted by over-expression of G3BP but was partially restored during expression of ΔNTF2, demonstrating that phase separation of G3BP enhances anti-viral activity towards PEMV2.

Since PEMV2 accumulation was not fully restored during ΔNTF2 expression, G3BP retains measurable anti-viral activity in the dilute state in the absence of SGs. Human G3BP1 can bind and promote the degradation of mRNAs with structured 3' untranslated regions (3' UTRs) in conjunction with upframeshift 1 (Upf1) as part of the structure-mediated RNA decay (SRD) pathway.[140] PEMV2 contains a highly structured 3' UTR [141] and like many RNA viruses is inhibited by Upf1.[142, 143] Therefore, G3BP over-expression could enhance SRD targeting of PEMV2 RNAs. While it remains unknown whether p26 partitioning into G3BP SGs is beneficial or detrimental for PEMV2 replication, p26 disrupts the Upf1-dependent nonsense-mediated decay

(NMD) pathway [106] and Upf1 is known to partition into SGs.[144] Future research will investigate whether partitioning of p26 into SGs interferes with Upf1- or G3BP-dependent RNA decay pathways.

In summary, our findings demonstrate that a plant virus movement protein forms droplets and partitions inside the nucleolus and SG membraneless compartments. Since nucleolar partitioning is required for virus trafficking and G3BP SG formation severely restricts PEMV2 replication, our findings highlight both beneficial and detrimental virus-host interactions mediated by phase separation.

Materials & methods

Construction of plant and bacterial expression vectors. All coding sequences and cloning strategies for the following constructs are detailed in S1 Supplemental Information [65]. Sequences for all primers used in this study are available in 2.S1 Table [65]. The pBIN61S binary vector was used to express proteins of interest in plants from the constitutive Cauliflower mosaic virus (CaMV) duplicated 35S promoter. $p26_{WT}$, $p26_{R/K\text{-}G}$, $p26_{D/E\text{-}G}$, and $p26_{\Delta NLS}$ GFP-fusions were PCR-amplified from synthetic double-stranded DNA fragments (Integrated DNA Technologies, Coralville, Iowa) and cloned into pBIN61S using the *BamH*I and *Sal*I restriction sites. $p26_{R/K\text{-}G}$ and $p26_{D/E\text{-}G}$ constructs contain glycine substitutions for all basic or acidic p26 residues, respectively. $p26_{\Delta NLS}$ is missing the coding sequence for amino acids 100-105 (5'-RRRARR-3') of p26. pBIN61S-GFP has been previously described.[145] The TMV vector pJL-TRBO has been previously described [130] and was a gift from John

Lindbo (Addgene plasmid # 80082). pJL-TRBO containing $p26_{WT}$ fused to GFP has also been previously described.[106] $p26_{R/K-G}$ and $p26_{D/E-G}$ GFP-fusions were PCR amplified from synthetic DNA fragments with introduced *Pac*I and *Not*I restriction sites for digestion and ligation into the corresponding pJL-TRBO sites. G3BP:RFP contains the G3BP coding region (accession AT5G43960.1) followed by the coding region of RFP and was a generous gift from Dr. Björn Krenz.[132] To construct ΔNTF2, G3BP:RFP was PCR amplified with the coding sequence for amino acids 2-125 of G3BP omitted. PCR amplification introduced forward *BamH*I and reverse *Sal*I restriction sites for cloning into pBIN61S. All ligations used T4 DNA Ligase (New England Biolabs, Ipswich, Massachusetts) following the manufacturer's protocol. pCB-PEMV2 has been previously described [142] and contains the full-length PEMV2 genome under control of a CaMV duplicated 35S promoter and was used to establish infections in *N. benthamiana*. All constructs were Sanger sequenced for accuracy.

For C-terminal GFP-fusion recombinant protein production in *E. coli*, pRSET his-eGFP [146] was used as a backbone and was a gift from Jeanne Stachowiak (Addgene plasmid # 113551). Coding sequences for the wild-type p26 IDR (amino acids 1-132) or p26 C-terminus (amino acids 133-226) were PCR amplified from a full-length PEMV2 infectious clone. The coding sequence for the last 10 amino acids of p26 was omitted from the C-term construct to circumvent proteolysis encountered during bacterial expression (not shown). Mutant IDRs containing R/K-G, D/E-G, or ΔNLS mutations were synthesized (Integrated DNA Technologies, Coralville, Iowa) as double-stranded DNA fragments and were used in restriction digests and ligation

reactions. IDR_{WT} was cloned into the *BamH*I restriction site of pRSET his-eGFP and sequenced for directionality and accuracy. C-term, $IDR_{R/K-G}$, $IDR_{D/E-G}$, and $IDR_{\Delta NLS}$ were cloned into pRSET his-eGFP using both the *Nhe*I and *BamH*I restriction sites and sequenced for accuracy.

Fib2 (accession AT4G25630.1) was cloned by first synthesizing cDNAs from *A. thaliana* seedling total RNAs using random hexamers and SuperScript III reverse transcriptase according to the manufacturer's protocol (ThermoFisher Scientific, Waltham, Massachusetts). Next, the Fib2 coding sequence was PCR amplified using primers that introduced *Nhe*I and *BamH*I restriction sites for cloning the fragment into pRSET-his-mCherry [147], a gift from Jeanne Stachowiak (Addgene plasmid # 113552). The resulting construct was full-length Fib2 with a C-terminal mCherry fusion ($Fib2_{FL}$). The coding sequence for the Fib2 GAR domain (amino acids 7-77 of Fib2) was PCR amplified from $Fib2_{FL}$ using primers that introduced *Nhe*I and *BamH*I restriction sites, digested, and ligated into corresponding sites of pRSET-his-mCherry to generate $Fib2_{GAR}$. Both constructs contain N-terminal histidine tags for affinity purification and were sequenced for accuracy.

Agroinfiltration and plant growth. All plant expression constructs used in this study were electroporated into *Agrobacterium tumerfaciens* strain C58C1. Liquid cultures were passaged in media containing the appropriate antibiotics and 20 μM acetosyringone 1 day prior to infiltration. Overnight cultures were pelleted and resuspended in a solution of 10 mM $MgCl_2$, 10 mM MES-K [pH 5.6], and 100 μM

acetosyringone as previously described.[142] All agroinfiltrations included a construct expressing the p14 RNA silencing suppressor from Pothos latent virus and has been previously described.[113] p14 was agroinfiltrated using a final OD_{600} of 0.2 and was included to enhance transient gene expression. pBIN61S-derived constructs expressing GFP, $p26_{WT}$, $p26_{R/K\text{-}G}$, $p26_{\Delta NLS}$, or $p26_{D/E\text{-}G}$ were agroinfiltrated at a final OD_{600} of 0.4. pJL-TRBO TMV vectors expressing GFP, $p26_{WT}$, $p26_{R/K\text{-}G}$, or $p26_{D/E\text{-}G}$ were also agroinfiltrated at a final OD_{600} of 0.4. G3BP and ΔNTF2 were agroinfiltrated using a final OD_{600} of 0.2. Finally, pCB-PEMV2 was agroinfiltrated alone or co-infiltrated with G3BP or ΔNTF2 using a final OD_{600} of 0.2 for each construct. Typically, the 3^{rd}-5^{th} leaves from young *N. benthamiana* plants were infiltrated with a 1 mL syringe. Visualization of nuclei in agroinfiltrated leaves was achieved by infiltrating a solution of 5 µg/mL DAPI (4′,6-diamidino-2-phenylindole) into leaves 45 minutes prior to confocal imaging. *N. benthamiana* plants were grown in a humidity-controlled chamber at 24°C, 65% humidity, and 12-hour day/night schedule (200 µmol $m^{-2}s^{-1}$).

Fluorescence recovery after photobleaching (FRAP). $p26_{WT}$ was transiently expressed from a 35S promoter in *N. benthamiana* as a GFP-fusion and produced visible fluorescence by 2 dpi. Leaf samples were wet-mounted and imaged using a Zeiss LSM 510 Meta confocal microscope with a 20X objective. FRAP was performed using Zen 2009 software (Zeiss, Oberkochen, Germany) and photobleaching a ~2 µm diameter region with 100% laser power (488 nm) with subsequent fluorescence recovery measured at 5 s intervals. Background regions and unbleached reference

droplets were recorded as controls. Data analysis was performed by subtracting background intensities, followed by normalization to set the first post-bleach value to zero as previously described.[148] Seven $p26_{WT}$ droplets were analyzed by FRAP and data was presented as a fraction of the pre-bleach fluorescence intensity with standard deviations using GraphPad Prism software (GraphPad, San Diego, California).

Protein expression and purification. The protein sequences of all recombinant proteins produced in this study are available in S1 Supplemental Information [65]. Histidine-tagged recombinant proteins were expressed in BL21(DE3) *E. coli* (New England Biolabs, Ipswich, Massachusetts) using autoinduction Luria-Bertani (LB) broth and purified using HisPur™ cobalt spin columns (Thermo Scientific, Waltham, Massachusetts). Proteins were purified under denaturing conditions according to the manufacturer's protocol using 8 M urea. All equilibration, wash, and elution buffers contained 1 M NaCl to suppress phase separation. Following elution of recombinant proteins from the cobalt resin, proteins were re-folded through dialysis in buffer containing 10 mM Tris-HCl (pH 7.0), 300 mM NaCl, 1 mM EDTA, 1 mM dithiothreitol, and 10% glycerol as previously used for the related pORF3 from GRV.[105] Urea was removed in a stepwise fashion by using dialysis buffers containing 4 M urea, 1 M urea, or no urea. Proteins were concentrated using Amicon® 10K Ultra centrifugal filters and concentrations were measured using a Bicinchoninic acid (BCA) protein assay (Millipore Sigma, St. Louis, Missouri). Next, protein molarity was determined

using predicted molecular weights for each protein using ProteinCalculator v3.4 (http://protcalc.sourceforge.net/) and are available in S1 Supplemental Information [65]. Protein purity was assessed by SDS-PAGE. If necessary, hydrophobic interaction chromatography using methyl HIC resin was used to further purify and concentrate GFP-fusion samples according to the manufacturers protocol (Bio-Rad, Hercules, California).

In vitro phase separation and RNA sorting assays. For in vitro assays, recombinant proteins were used at a final concentration of 8 μM unless otherwise noted. Phase separation assays consisted of the following mixture: 8 μM protein, 10 mM Tris-HCl (pH 7.5), 1 mM DTT, 100 mM NaCl, and 10% PEG-8000 to induce phase separation. High-salt conditions included NaCl at a final concentration of 1 M and "no treatment" did not include PEG-8000. Turbidity assays comparing IDR_{WT} with controls or IDR mutants were performed with either 8 μM or 24 μM protein under standard assay conditions. 100 μL reactions were placed at room temperature for 15 minutes prior to OD_{600} measurements using a 96-well plate reader. Details regarding in vitro assays using untagged IDR_{WT} or tagged $IDR_{R\text{-}K}$ and $IDR_{VLIMFYW\text{-}S}$ constructs are available in S1 Materials and Methods [65].

Cy5-labelled gRNAs from PEMV2 or TCV were synthesized by T7 run-off transcription using *Sma*I-linearized full-length infectious clones of PEMV2 (see S1 Supplemental Information [65]) or TCV [149]. Cy5-labelled *Renilla* luciferase (RLuc) RNAs were synthesized from PCR products containing a T7 promoter, RLuc ORF, and a 13-

nt 3' untranslated region using p2luci plasmid as template [150] (see S1 Table for primers [65]. Cy5-UTP (APExBIO, Houston, Texas) was added to in vitro transcription reactions according to the HiScribe T7 Quick High Yield RNA Synthesis Kit protocol (New England Biolabs, Ipswich, Massachusetts). Synthesized RNAs were purified using the Monarch RNA Cleanup Kit (New England Biolabs, Ipswich, Massachusetts). RNA integrity was assessed by agarose gel electrophoresis and RNA concentrations were determined using a UV5Nano spectrophotometer. RNAs were mixed with 8 μM IDR_{WT}, $Fib2_{GAR}$, or $Fib2_{FL}$ at a final concentration of 16 nM (1:500 RNA:protein ratio). For observing vRNP formation in vitro, equimolar amounts of $Fib2_{FL}$ and IDR_{WT} (8 μM each) were mixed with 16 nM PEMV2-Cy5 gRNA since atomic force microscopy revealed that Fib2 and GRV pORF3 form ring-like complexes with equimolar composition.[107]

Confocal microscopy and image processing. Phase separation during in vitro assays occurred rapidly and samples were directly loaded onto glass slides for confocal microscopy. A 20x objective from a Zeiss LSM 510 Meta confocal microscope with Zen 2009 software was used to visualize droplet formation. IDR_{WT} and Fib2 droplets were observed after excitation with the 488-nm or 543-nm lines, respectively. Cy5-labelled RNAs were observed after excitation with the 633-nm laser line.

Confocal images were used to measure total droplet areas (%) from three representative 20x fields for each condition. Raw images (.lsm extension) were first

imported into ImageJ.[151] Images were thresholded (typically 500-66535 for 16-bit images) and total droplet areas (%Area) were measured using the “analyze particles” function excluding particles <1 μm^2 in size. Mean droplet sizes were measured from three representative 20x fields for IDR_{WT}, $IDR_{D/E\text{-}G}$, and $IDR_{\Delta NLS}$ using the “analyze particles” function. Particles <0.2 μm^2 in size were excluded from downstream analyses. Particle sizes were plotted using a cumulative distribution function (CDF) for comparing droplet sizes between IDR_{WT} and mutant IDRs.

The number of p26 granules that co-localized with DAPI-stained nuclei after expression from a 35S promoter or TRBO vector in *N. benthamiana* were manually counted from 20x fields. Next, the total number of granules >2 μm^2 was counted for each thresholded 20x field using the ImageJ “analyze particles” function. Thresholds were used to include only granules in the focal plane of the 20x field. Dividing the number of nuclear granules by the total granule count yielded the percentage of nuclear granules for $p26_{WT}$, $p26_{\Delta NLS}$, or $p26_{D/E\text{-}G}$.

The ImageJ plugin EzColocalization [129] was used to measure colocalization in multi-channel confocal images. Raw images were imported into ImageJ and split into separate channels for GFP/mCherry and Cy5. Default settings including Costes threshold parameters were used to calculate Mander’s overlap coefficients (MOC) that measured the fraction of IDR_{WT}, $Fib2_{GAR}$, $Fib2_{FL}$ signal that was positive for Cy5-labelled RNAs from three 20x fields.

TMV movement assay and RT-PCR. Following agroinfiltration of TRBO vectors expressing GFP, $p26_{WT}$, $p26_{R/K-G}$, or $p26_{D/E-G}$ GFP-fusions, fluorescence in local and systemic leaves was monitored daily using a hand-held long-wave UV lamp. By 4 dpi, robust local infections were evident, and leaves were imaged (488 nm) using a Bio-Rad Gel Doc XR System prior to grinding in liquid nitrogen. Total protein was extracted by resuspending leaf tissue in 1X PBS supplemented with 3% β-mercaptoethanol and EDTA-free protease inhibitor cocktail (Thermo Scientific, Waltham, Massachusetts). Samples were mixed with 6X Laemmli SDS buffer, boiled, and separated by SDS-PAGE. A semi-dry transfer method was used to transfer proteins to nitrocellulose for western blotting using anti-GFP antibodies (Life technologies, Carlsbad, California) at a 1:5000 dilution. Goat anti-rabbit IgG (H+L) conjugated with horseradish peroxidase (Thermo Scientific, Waltham, Massachusetts) was used as a secondary antibody at a 1:5000 dilution. Blots were visualized using the Pierce enhanced chemiluminescence kit (Thermo Scientific, Waltham, Massachusetts). Systemic leaves were harvested at 14 dpi for total RNA extraction using Trizol. 100 ng total RNA was digested with RQ1 DNase (Promega, Madison, Wisconsin) and served as template for reverse transcription using iScript supermix (Bio-Rad, Hercules, California). Controls lacking reverse transcriptase (-RT) were included for all sample and primer sets. 1 µL cDNA was used as template for 25 cycles of PCR using GoTaq polymerase (Promega, Madison, Wisconsin) targeting the TMV replicase in the TRBO vector. For loading controls, *N. benthamiana* actin was amplified by 31 cycles of PCR. Primer sequences are available in S1 Table [65].

G3BP expression, SG formation, and visualization. Full-length G3BP or ΔNTF2 (RFP-tagged) were transiently expressed in *N. benthamiana* using agroinfiltration and visualized 3 dpi using confocal microscopy (543-nm line). Heat shock of G3BP-expressing plants was performed by incubating plants at 37°C for 45 minutes prior to imaging. p26 partitioning into SGs was observed following heat shock of plants transiently co-expressing $p26_{WT}$ and G3BP from 35S promoters. To observe co-localization of p26 and G3BP during virus infection, *N. benthamiana* plants (3-4 leaf stage) were first infiltrated with TRBO-$p26_{WT}$. After strong $p26_{WT}$ GFP-fusion signal was observed in the systemic leaves (typically ~2-3 weeks), G3BP was agroinfiltrated and leaves were imaged at 5 dpi following excitation with the 488-nm and 543-nm lines to observe p26 and G3BP, respectively. Using the same protocol as above, western blotting with anti-RFP antibodies at a 1:5000 dilution (ThermoFisher Scientific, Waltham, Massachusetts) was performed to examine full-length G3BP or ΔNTF2 expression levels following agroinfiltration.

RT-qPCR. Agroinfiltrated “spots” were cut from leaves and stored at -80ºC. Samples were ground in liquid nitrogen and total RNA was extracted using the Quick-RNA Plant Kit (Zymo Research, Irvine, California). An on-column DNase I step was added using RQ1 DNase (Promega, Madison, Wisconsin). Total RNAs were used as templates for SYBR green-based one-step reverse-transcriptase quantitative PCR (RT-qPCR) using the NEB Luna One-Step RT-qPCR kit (New England Biolabs,

Ipswich, Massachusetts). All primers used in this study were designed using Primer3 [152] and were validated by standard curve analysis with PCR efficiencies ranging from 90-110%. Targets included native *N. benthamiana* G3BP (Transcript ID: Niben101Scf03456g00002.1) and PEMV2 gRNA. Gene expression was normalized to the internal control transcripts from the agroinfiltrated p14 RNA silencing suppressor. All primer sequences are available in S1 Table [65]. Expression analyses were performed by the ΔΔCq method using Bio-Rad CFX Maestro software. Target fidelity was monitored by melt curve analyses and no reverse transcriptase controls.

Statistical analyses. GraphPad Prism (version 9.0.1) software was used for all statistical analyses in this study. Total droplet areas (%) from confocal images or turbidities (OD_{600}) were compared using a two-way ANOVA with Sidak's multiple comparison test. *P* values <0.001 were considered significant. Mann-Whitney tests were used to compare ranked droplet sizes (μm^2) from confocal images. *P* values <0.001 were considered significant. An unpaired t test was used to determine if differences in nuclear localization of $p26_{WT}$ or $p26_{D/E-G}$ granules were significant. Mander's Overlap Coefficient (MOC) values were compared using either an unpaired t test (2 samples, Figure 2.5B) or a one-way ANOVA with Tukey's multiple comparisons test (3 samples, Figure 2.5D). *P* values >0.001 were considered not significant. Nuclear localization of $p26_{WT}$ or $p26_{D/E-G}$ expressed from a 35S promoter or TRBO vector was compared using multiple unpaired t tests. *P* values >0.001 were considered not significant. Following RT-qPCR, relative G3BP gene expression

values were compared using an unpaired t test. PEMV2 RNA levels were compared using Brown-Forsythe and Welch ANOVA tests and Dunnett's multiple comparisons test. *P* values <0.05 were considered significant.

CHAPTER 3

3. VIRAL CONDENSATES FORMED BY PEA ENATION MOSAIC VIRUS 2 SEQUESTER RIBOSOMAL COMPONENTS AND SUPPRESS TRANSLATION

Adapted with permission from Brown, S. L.; May, J. P. Viral condensates formed by Pea enation mosaic virus 2 sequester ribosomal components and suppress translation. *Virology* **2025**, *601*, 110301. DOI: https://doi.org/10.1016/j.virol.2024.110301.

Chapter Summary

Viral proteins with intrinsic disorder can undergo liquid-liquid phase separation (LLPS), forming condensates that facilitate specific stages of virus replication cycles. However, the impact of viral condensate formation on essential cellular processes, such as translation, is unclear. Our previous research showed that the long-distance movement protein p26 from Pea enation mosaic virus 2 (PEMV2) undergoes phase separation to form cytoplasmic condensates and to partition into the nucleolus. Nevertheless, the effects of p26 condensates on cellular processes remained unclear. In this study, we performed mass spectrometry on affinity-purified p26 condensates from *Saccharomyces cerevisiae*. Enriched proteins were ribosomal, but there was no significant overlap with known stress granule or processing body constituents, suggesting that p26 condensates are distinct and sequester RNA-binding proteins involved in translation and ribosome biogenesis. Puromycin incorporation assays and

polysome profiling revealed that p26 suppresses global translation and ribosome assembly in *Nicotiana benthamiana*, with similar defects observed during the late stages of PEMV2 infection. Although p26 sequesters the 2'-*O*-methyltransferase fibrillarin in cytoplasmic condensates, it does not inhibit translation by altering 2'-*O*-methylation of rRNAs. Instead, p26 binds directly to rRNAs, sequestering them into insoluble complexes and reducing their accessibility. Our data supports a model in which p26 sequesters rRNAs and ribosomal proteins into condensates during the late stages of infection, making these components inaccessible for translation and disrupting ribosome assembly. This impairment may favor viral RNA trafficking over translation.

p26 Plays an Indirect Role in Virus Accumulation

Following our previous work, we wanted to investigate the function of p26 condensates and identify what role they play in virus infection. Virus-induced membraneless organelles are often associated with replication, likely because many viral condensates have been identified as virus factories for -sense RNA viruses. Viral condensates have also been reported in conjunction with +sense RNA virus infections [29, 31, 61], despite +sense virus replication factories being membrane-associated.[54, 58] Thus, we hypothesized that p26 condensates served a function outside of virus replication.

In support of this, it has been shown that mutating the p26 start codon in PEMV2 reduces the accumulation of viral RNA 4-fold but does not completely inhibit

viral accumulation.[29] The decrease in viral accumulation is likely a result of nonsense-mediated decay (NMD), an RNA degradation pathway that poses a threat to many RNA viruses.[29] PEMV2 is targeted by the NMD pathway, but previous work has shown that p26 is able to confer protection for cellular and viral mRNAs against NMD.[29] NMD targets transcripts with premature termination codons (PTCs), long 3' untranslated regions (UTRs), and functional mRNA to protect the host from expressing truncated proteins and to modulate gene expression.[29] Often, +sense ssRNA viruses have highly structured and multi-functional 3' untranslated regions (UTRs), which allow the 3'UTR to regulate processes like viral replication, translation, and the host immune response.[153] Due to the presence of a long 3' UTR, RNA viruses are particularly susceptible to RNA degradation pathways, like nonsense-mediated decay (NMD).[29] RNA viruses must circumvent RNA decay to sustain virus accumulation. Therefore, we believe p26 plays an indirect role in virus accumulation as opposed to forming condensates that directly contribute to viral replication.

The mechanism for p26-mediated protection of host and viral transcripts against NMD is still unclear, though it's been proposed that p26 condensates may facilitate this phenomenon.[29] Previous work with GRV has shown that ORF3, a p26 orthologue, binds ssRNA, ssDNA and dsRNA with seemingly no specificity.[29, 154] It was posited that p26 may sequester host and viral mRNAs into p26 inclusion bodies to safeguard the transcripts from NMD surveillance.[29]

Introduction

Condensates that form through liquid-liquid phase separation (LLPS) can play important roles in organizing cellular components and regulating basic cellular processes like genomic organization [155], transcriptional regulation [156], and translation [157]. Nearly all viruses interact with cellular condensates during infection, frequently redirecting host proteins from these condensates to viral replication sites.[158] For instance, numerous families of RNA and DNA viruses divert proteins from stress granules and processing bodies, disrupting their normal roles in translational repression and RNA decay to promote viral replication.[47]

Viral proteins can undergo LLPS during infection, forming condensates that play crucial roles in virus replication cycles.[158, 159] Well-studied examples include condensates formed by negative-stranded RNA viruses in the order *Mononegavirales*, which aid RNA replication.[160] N protein condensates from SARS-CoV-2 maximize replication efficiency and promote both nucleocapsid assembly and genome processing.[61, 99] Similar to animal viruses, plant viruses such as Tomato bushy stunt virus (TBSV) also form condensates that are essential for efficient virus accumulation.[161, 162] The multi-functional p26 movement protein from Pea enation mosaic virus 2 (PEMV2) undergoes LLPS and transports viral RNAs through the vascular system of infected plants.[65, 103] This process requires interactions between p26 and fibrillarin [105, 108], a 2'-*O*-methyltransferase that forms the dense fibrillar component of the nucleolus [125].

RNA viruses often employ "shut-off" mechanisms to inhibit host translation, effectively disrupting cellular protein synthesis to prioritize viral replication. These mechanisms typically involve the degradation of host mRNAs or the sequestration of translation machinery.[19] Although radical shut-off mechanisms are not common in plant virus infections [163], several translation factors are relocated to viral replication complexes formed by tobamoviruses, tombusviruses, and potyviruses [164]. While viral condensates have yet to be directly implicated in host shut-off, several studies suggest that LLPS-prone viral proteins may play more nuanced roles in regulating or repressing translation. For example, SARS-CoV-2 N protein interacts with the translation machinery and forms complexes with nucleophosmin 1 and small nucleolar RNAs.[165] These interactions increase 2'-*O*-methylation (2'-OMe) of 18S and 28S ribosomal RNAs (rRNAs), specifically enhancing the translation of viral RNAs.[165] Next, condensation of the Human immunodeficiency virus (HIV-1) nucleocapsid suppresses the translation of viral RNAs to favor virus assembly.[166] In plants, Potato virus A (PVA) encodes HCpro, which forms "RNA granules" that can either enhance or suppress the translation of viral RNAs, depending on their composition. In these granules, oligouridylate-binding protein 1 (UBP1) suppresses translation, while eIF(iso)4E promotes VPg-dependent translation of viral RNAs.[167] Finally, p26 inhibits the co-translational nonsense-mediated decay (NMD) pathway that targets PEMV2, potentially through the translational repression of NMD targets.[106, 142]

Viral condensates are increasingly recognized for their role in promoting virus replication, primarily through concentrating viral and host factors.[54] However, despite

this growing understanding, much less is known about how these condensates influence basic cellular processes, such as translation. In this study, we demonstrate that the PEMV2 movement protein, p26, sequesters ribosomal components, leading to defects in ribosome assembly during infection. Due to the incompatibility between translation and systemic viral movement of PEMV2 RNAs, we propose that p26 condensates could repress translation to favor virus trafficking during the late stages of infection.

Results

p26 condensates are enriched with ribosomal proteins and repress global translation. To characterize the protein interactome of p26 condensates, we performed mass spectrometry analyses of affinity-purified p26 condensates from LLPS-enriched fractions in *Saccharomyces cerevisiae*. Using yeast for proteomics is common amongst plant virologists [168-170] and has been instrumental in identifying virus-host interactions that are conserved in plants.[171, 172] GFP or p26:GFP constructs were expressed in *S. cerevisiae* for 6 hours via a galactose-inducible (GAL1) promoter. Protein expression was confirmed using confocal microscopy and like our previous work in *Nicotiana benthamiana* [65], GFP showed a diffuse nuclear-cytoplasmic expression pattern, whereas p26 formed discernable nuclear and cytoplasmic foci (Figure 3.1A).

Yeast expressing GFP or p26:GFP were subjected to a modified stress granule purification method using differential centrifugation [173], followed by affinity purification

using GFP-Trap. The presence of p26 condensates in the LLPS-enriched fractions was confirmed by direct visualization using confocal microscopy before affinity purification and nano LC-MS/MS analysis (Figure 3.1A). To account for non-specific binding during immunoprecipitation, both the soluble and LLPS-enriched fractions from GFP-expressing lysates were analyzed by LC-MS/MS. An average of ~300 proteins and 2,059 unique peptides were identified in the p26 condensate samples (Supplementary Data 1 [174]). After applying a 1% false discovery rate (FDR) cut-off, adjusting for a complete absence of spectral counts in the GFP LLPS control samples, and an imputed Log2-fold change >2, 44 proteins were identified as significant, including the known p26 interactor fibrillarin (NOP1) (Figure 3.1B). Interestingly, 18 of the top 20 most enriched proteins in p26 condensates were ribosomal proteins (Figure 3.1C). When comparing the p26 interactome to the known constituents of stress granules and processing bodies in yeast [80], only 2 out of the 44 identified p26-interactors were shared with stress granules (Figure 3.1D). This indicates that p26 condensates are distinct entities that sequester RNA-binding proteins involved in translation and ribosome biogenesis, as revealed by gene ontology analyses (Figure 3.1E, Supplementary Data 2 [174]).

Given the strong association between ribosomal proteins and p26 condensates, we next investigated whether p26 impacts translation. At 6 h post-induction, global protein synthesis was measured in yeast expressing GFP or p26:GFP by measuring the uptake of a methionine analog (L-homopropargylglycine) using Click-iT chemistry and flow cytometry (Figure 3.1F). Mean global translation was

reduced by 6% in p26-expressing cells compared to GFP control cells (Figure 3.1G). In the top 10% of p26-expressing cells, the level of translational repression doubled to >12% (Figure 3.1H). Due to the aforementioned translational repression observed with p26 expression, we anticipated a decrease in growth rates. Indeed, following galactose induction, yeast expressing p26 showed a clear growth defect compared to those expressing GFP (Figure 3.1I). However, when protein expression was suppressed by glucose, *S. cerevisiae* strains transformed with either GFP or p26 displayed identical growth curves (Figure 3.1I). In summary, p26 condensates are enriched with ribosomal proteins, and p26 expression suppresses global translation, leading to noticeable growth defects in yeast.

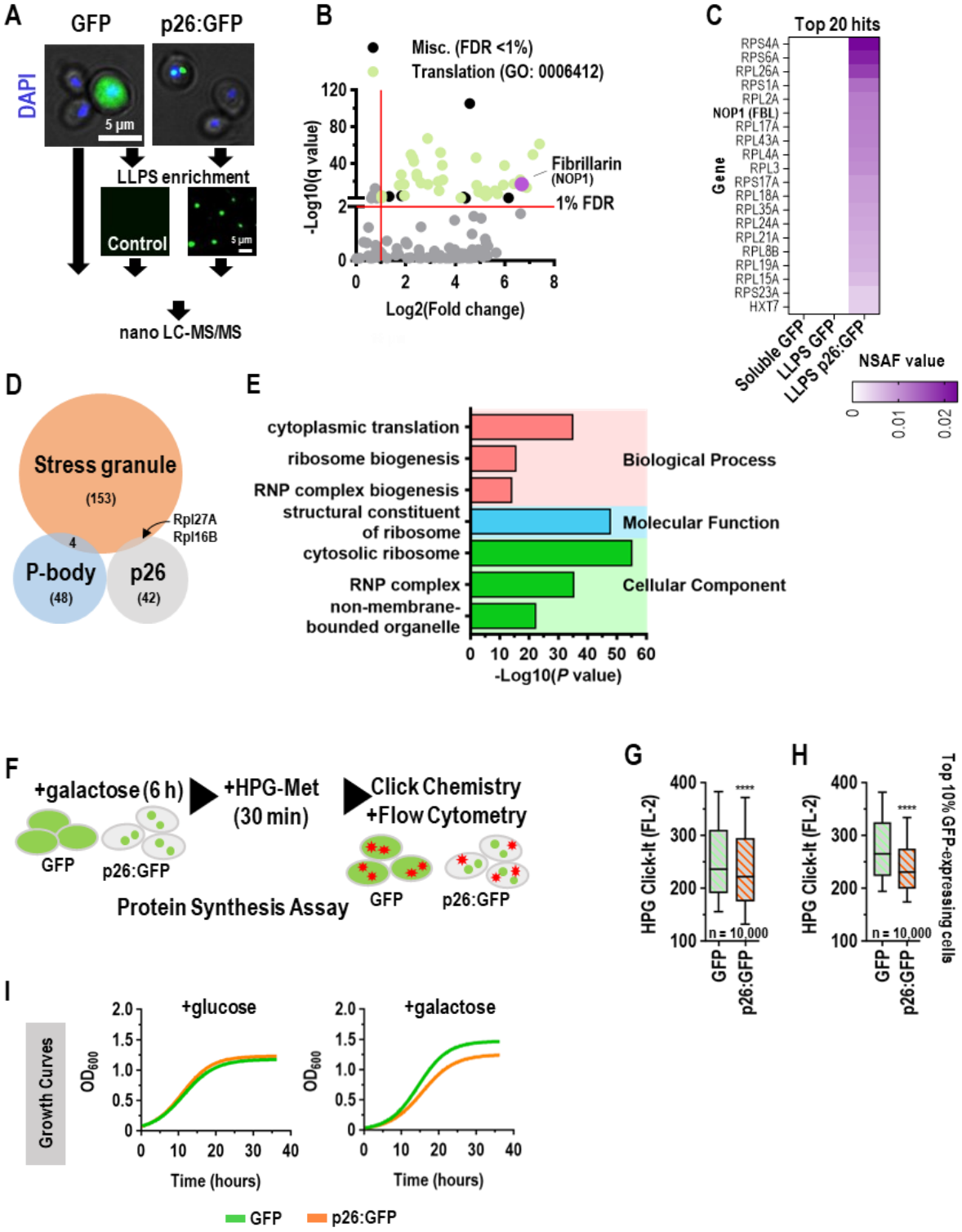
A
GFP
p26:GFP
DAPI
5 µm
LLPS enrichment
Control
5 µm
nano LC-MS/MS
B
Misc. (FDR <1%)
Translation (GO: 0006412)
-Log10(q value)
Log2(Fold change)
Fibrillarin (NOP1)
1% FDR
C
Top 20 hits
Gene
RPS4A
RPS6A
RPL26A
RPS1A
RPL2A
NOP1 (FBL)
RPL17A
RPL43A
RPL4A
RPL3
RPS17A
RPL18A
RPL35A
RPL24A
RPL21A
RPL8B
RPL19A
RPL15A
RPS23A
HXT7
Soluble GFP
LLPS GFP
LLPS p26:GFP
NSAF value
D
Stress granule
(153)
Rpl27A
Rpl16B
4
P-body
(48)
p26
(42)
E
cytoplasmic translation
ribosome biogenesis
RNP complex biogenesis
structural constituent of ribosome
cytosolic ribosome
RNP complex
non-membrane-bounded organelle
Biological Process
Molecular Function
Cellular Component
-Log10(P value)
F
+galactose (6 h)
+HPG-Met (30 min)
Click Chemistry +Flow Cytometry
GFP
p26:GFP
Protein Synthesis Assay
G
HPG Click-It (FL-2)
n = 10,000
H
Top 10% GFP-expressing cells
I
Growth Curves
+glucose
+galactose
OD600
Time (hours)
GFP
p26:GFP

Figure 3.1 p26 condensates are enriched with ribosomal proteins and repress global translation

(**A**) p26 condensates were purified from *S. cerevisiae* using differential centrifugation and affinity purification. p26 condensates were visualized in yeast and LLPS-enriched fractions using confocal microscopy. (**B**) p26 interactors were identified using a 1% FDR following nano LC-MS/MS. (**C**) Top 20 p26 interactors are ranked by normalized spectral abundance factor (NSAF). Proteins were only included if they were identified in all p26 LLPS samples and absent from GFP controls. (**D**) Proteins passing a 1% FDR were cross-referenced with known stress granule and P-body proteins. (**E**) Gene ontology analyses of p26 interactors passing a 1% FDR were performed using the Saccharomyces Genome Database Go Term Finder (Version 0.86). (**F**) Overview of protein synthesis assay in *S. cerevisiae* using click chemistry and flow cytometry. (**G-H**) Flow cytometry analyses measuring global translation (i.e., HPG-Met incorporation). **** $P<0.0001$ unpaired Mann-Whitney rank test (**I**) Growth curves of *S. cerevisiae* with repressed p26 expression (+glucose) or induced expression (+galactose). Logistic growth curves represent the mean values from 6-8 biological replicates, where n=2.

p26 disrupts ribosome assembly and translation in plants during PEMV2 infection. To confirm that p26 also represses translation in plants, a puromycin incorporation assay (Figure 3.2A) was used to measure global translation in *N. benthamiana* leaves [175] expressing either GFP or p26:GFP. Puromycin inhibits translation by mimicking aminoacyl-tRNA, causing premature termination of the growing peptide chain. Proteins were expressed for 2 days following agroinfiltration and puromycin was vacuum infiltrated into leaves prior to tissue lysis. Puromycin incorporation (i.e., translation) was then quantified by densitometry following western blotting with anti-puromycin antibodies. As expected, global translation was repressed in plants expressing p26, with a 42% reduction observed in leaves expressing p26 compared to GFP (Figure 3.2B).

To determine whether the observed translational repression during p26 expression was due to a defect in ribosome assembly, we performed polysome profiling to separate and analyze ribosomal complexes based on their size and density. Interestingly, we observed a significant decrease in monosome formation in p26-expressing *N. benthamiana* leaves compared to those expressing GFP (Figure 3.2C). The polysome profiles we observed in control plants resemble those in other mature leaf tissues, with subdued polysome peaks and difficulty distinguishing the 40S and 60S subunits.[176] To validate these findings in the context of PEMV2 infection, we also performed polysome profiling using PEMV2-infected plants. We first measured PEMV2 accumulation in *N. benthamiana* following agroinfiltration over a 1-week period, observing an initial phase from 0-2 days characterized by low PEMV2

levels, followed by a "late" phase from 3-7 days post-infiltration where PEMV2 levels peaked (Figure 3.2D). Somewhat expectedly, no significant difference in puromycin incorporation was observed between mock- and PEMV2-infected plants during the early stages of infection, likely due to the low levels of PEMV2 accumulation at this stage (Figure 3.2D). Therefore, we performed polysome profiling at 5 dpi in plants infected with either the wild-type PEMV2 strain or the PEMV2Δp26 mutant, which carries a start codon mutation preventing p26 expression [106] and shows a 10-fold decrease in viral accumulation (Figure 3.2E). Like ectopic p26 over-expression, PEMV2 infection suppressed monosome and polysome formation; however, ribosome assembly was restored during infection with PEMV2Δp26 (Figure 3.2F). These results demonstrate that p26 expression, whether on its own or during virus infection, causes defects in ribosome assembly and translation. Additionally, our findings suggest that translation is repressed during the late stages of PEMV2 infection, which could have implications for virus movement, a process that inherently conflicts with active translation.

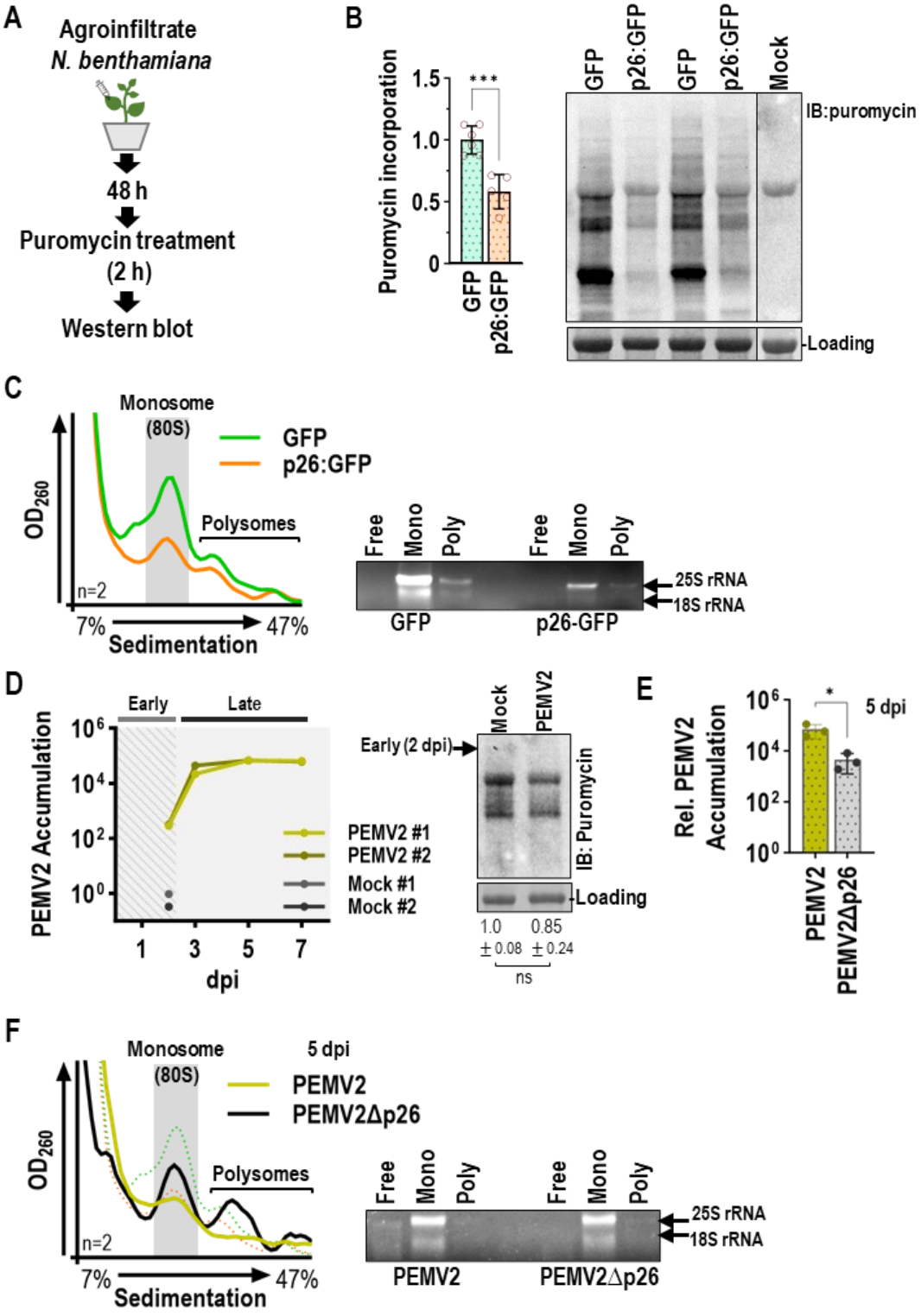
A
Agroinfiltrate
N. benthamiana
48 h
Puromycin treatment
(2 h)
Western blot
B
Puromycin incorporation
1.5
1.0
0.5
0
***
GFP
p26:GFP
GFP
p26:GFP
GFP
p26:GFP
Mock
IB:puromycin
Loading
C
Monosome
(80S)
GFP
p26:GFP
OD260
Polysomes
n=2
7%
47%
Sedimentation
Free
Mono
Poly
Free
Mono
Poly
25S rRNA
18S rRNA
GFP
p26-GFP
D
Early
Late
PEMV2 Accumulation
10^6
10^4
10^2
10^0
1
3
5
7
dpi
PEMV2 #1
PEMV2 #2
Mock #1
Mock #2
Mock
PEMV2
Early (2 dpi)
IB: Puromycin
Loading
1.0
0.85
±0.08
±0.24
ns
E
Rel. PEMV2
Accumulation
10^6
10^4
10^2
10^0
*
5 dpi
PEMV2
PEMV2Δp26
F
Monosome
(80S)
5 dpi
PEMV2
PEMV2Δp26
OD260
Polysomes
n=2
7%
47%
Sedimentation
Free
Mono
Poly
Free
Mono
Poly
25S rRNA
18S rRNA
PEMV2
PEMV2Δp26

Figure 3.2 p26 disrupts ribosome assembly and translation in plants during PEMV2 infection

(**A**) Overview of puromycin incorporation assay in *N. benthamiana.* (**B**) Puromycin incorporation assay was measured following western blotting with anti-puromycin antibodies and densitometry. Ponceau S-stained rubisco (large subunit) served as loading controls and was also used for densitometry normalization. *** $P<0.001$ unpaired t test. (**C**) Polysome profiling of GFP- or p26-expressing *N. benthamiana* was performed at 3 days post-infiltration. Polysome profile curves represent the mean absorbances from two independent experiments. Aliquots were collected from free mRNA, monosome or polysome fractions and separated by gel electrophoresis. (**D**) Mock- or PEMV2-infected plants (n=2) were subjected to RT-qPCR targeting PEMV2 and ubiquitin (reference) RNAs. Mock or PEMV2 samples were collected at 2 dpi and subjected to the puromycin incorporation assay and western blotting with anti-puromycin antibodies, where the loading control is Ponceau S-stained rubisco (large subunit). Quantification, via densitometry, is reported as mean $\pm$ standard deviation from five biological replicates. ns not significant unpaired t test (**E**) Wild-type and mutant PEMV2 virus accumulation was quantified at 5 dpi using RT-qPCR. GAPDH transcripts served as the reference for relative PEMV2 levels, with wild-type levels normalized to 5 dpi PEMV2 in Panel D. * $P<0.05$ unpaired t test. (**F**) Polysome profiles from wild-type or mutant PEMV2-infected plants (5 dpi). Polysome profile curves represent the mean absorbances from two independent experiments. Free GFP and p26:GFP polysome profiles from Panel C are included for comparison (dashed lines). Aliquots from free mRNA, monosome, or polysome fractions were separated by gel electrophoresis.

PEMV2 does not disrupt fibrillarin-mediated 2'-*O*-methylation of rRNAs. It is well established that related umbravirus movement proteins must interact with fibrillarin to establish systemic infections.[31, 32] However, it remains unclear whether p26 or other viral proteins that interact with fibrillarin [177] can influence its 2'-*O*-methyltransferase activity. Fibrillarin is primarily responsible for the 2'-*O*-methylation (2'-OMe) of rRNAs.[178] These 2'-OMe modifications stabilize rRNA structure, influence base-pairing, and regulate ribosome activity.[179-181] During p26 expression, fibrillarin (Fib2) co-localizes with p26 condensates in the cytoplasm, deviating from its typical nucleolar localization pattern (Figure 3.3A). Furthermore, we confirmed that p26 and Fib2 directly interact by co-immunoprecipitation analyses (Figure 3.3B). To determine whether 2'-OMe patterns on rRNAs are altered by p26, we performed RiboMethSeq to measure changes in 2'-OMe levels during PEMV2 infection with single-nucleotide resolution. RiboMethSeq is highly sensitive and can detect changes in 2'-OMe levels as small as approximately 10%.[182-185] This method is based on the increased protection of phosphodiester bonds in RNA from cleavage under alkaline conditions due to 2'-OMe modifications on the 5'-neighboring base.

We performed RiboMethSeq on mock-infected and PEMV2-infected *N. benthamiana* plants. Additionally, we included Fib2-silenced *N. benthamiana* as a positive control to confirm reduced 2'-OMe levels across rRNAs (Figure 3.3C). Normalized read count and coverage across the entire 45S rRNA precursor was nearly identical between mock- and PEMV2-infected samples (Figure 3.3D), ruling out the possibility that p26 represses translation by decreasing overall rRNA abundance.

Next, if p26 interferes with rRNA processing, an increase in the number of reads mapping to the external or internal transcribed spacers (e.g., 5' ETS or ITS1) is expected. However, we failed to observe any significant increase in rRNA precursors during PEMV2 infection (Figure 3.3E), indicating that p26, and therefore PEMV2, likely suppresses translation through mechanisms unrelated to rRNA processing. RiboMethScores were calculated for conserved 18S and 25S rRNA 2'-OMe sites that were previously validated in *Arabidopsis thaliana* rRNAs [186]. We confirmed the presence of 2'-OMe at >95% of conserved sites between Arabidopsis and *N. benthamiana* (Figure 3.3F). Importantly, nearly all positions had reduced RiboMethScores in Fib2-silenced plants, confirming the importance of fibrillarin for rRNA methylation (Figure 3.3F). However, no significant changes in 2'-OMe levels were observed during PEMV2 infection (Figure 3.3F, Supplementary Data 3 [174]). This suggests that p26's sequestration of Fib2 into cytoplasmic condensates does not impact rRNA 2'-OMe modification or contribute to p26-mediated translational repression.

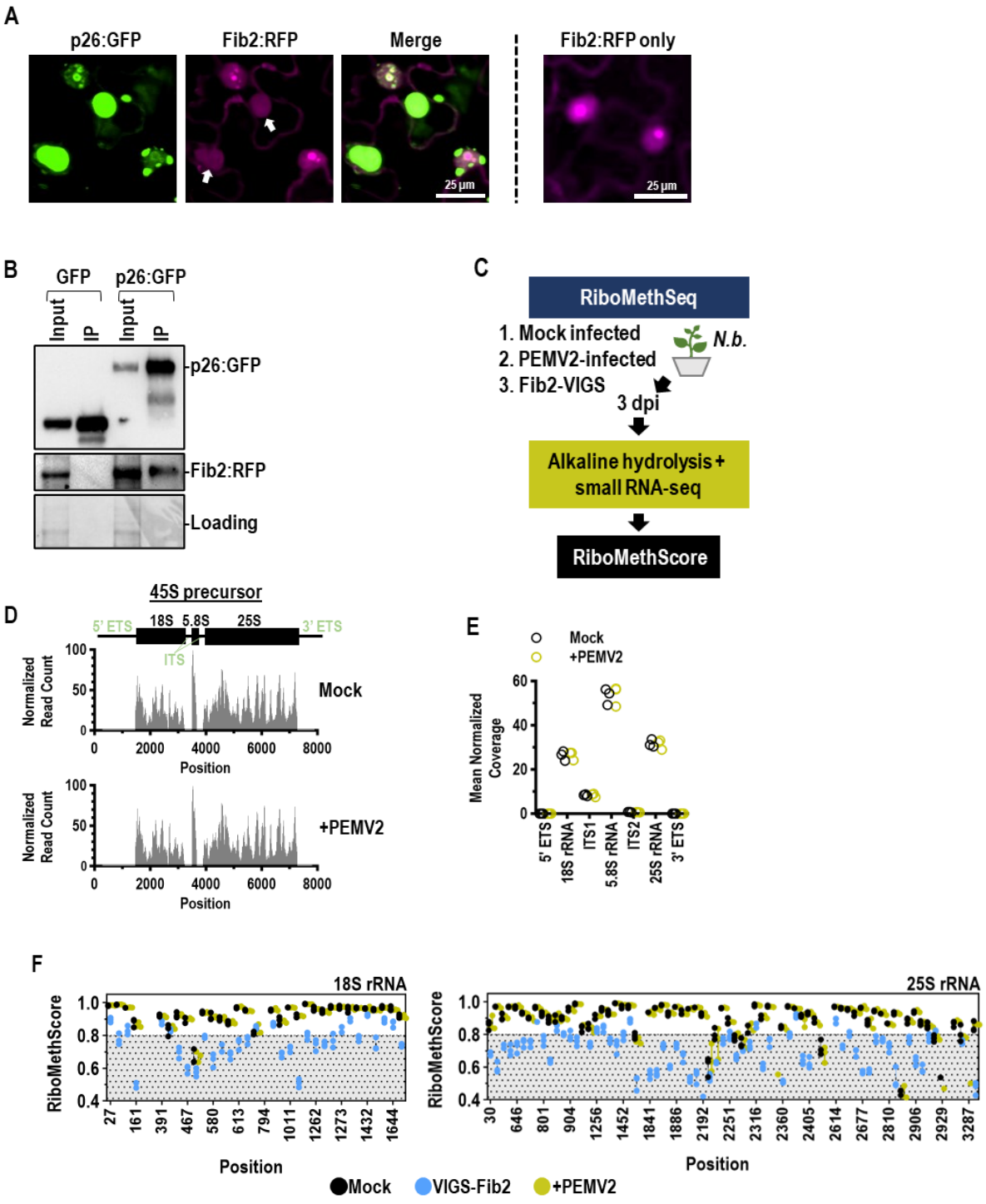
A
p26:GFP
Fib2:RFP
Merge
Fib2:RFP only
25 µm
25 µm
B
GFP
p26:GFP
Input
IP
Input
IP
p26:GFP
Fib2:RFP
Loading
C
RiboMethSeq
1. Mock infected
2. PEMV2-infected
3. Fib2-VIGS
N.b.
3 dpi
Alkaline hydrolysis + small RNA-seq
RiboMethScore
D
45S precursor
5' ETS
18S
5.8S
25S
3' ETS
ITS
Normalized Read Count
Mock
+PEMV2
Position
E
Mock
+PEMV2
Mean Normalized Coverage
5' ETS
18S rRNA
ITS1
5.8S rRNA
ITS2
25S rRNA
3' ETS
F
18S rRNA
25S rRNA
RiboMethScore
Position
Mock
VIGS-Fib2
+PEMV2

Figure 3.3 PEMV2 does not disrupt fibrillarin-mediated 2'-O-methylation of rRNA

(**A**) Co-localization between p26:GFP and Fib2:RFP was visualized using confocal microscopy following agroinfiltration of *N. benthamiana*. White arrows denote cytoplasmic co-localization between p26 and Fib2. (**B**) Co-immunoprecipitation analyses between p26 and Fib2. GFP-Trap was used to pull-down p26:GFP from *N. benthamiana* leaves that were co-infiltrated with Fib2:RFP. Ponceau S-stained membranes are shown for loading controls. (**C**) Experimental design for RiboMethSeq. (**D**) Normalized read counts across the 45S rRNA precursor for Mock- or PEMV2-infected samples. (**E**) The mean normalized coverage of rRNA precursor regions was determined by calculating the mean normalized read counts for each region. Biological replicates are shown. (**F**) RiboMethScores for conserved rRNA 2'-OMe sites previously validated in *A. thaliana* are shown for the 18S and 25S rRNAs during mock or PEMV2 infection. Fib2-silenced plants (VIGS-Fib2) were used as a control to confirm reduced 2'-OMe levels across rRNAs.

p26 directly binds and sequesters rRNAs into insoluble condensates. After determining that p26 does not disrupt rRNA methylation, we investigated whether p26 binds and sequesters rRNAs into condensates as a potential mechanism for disrupting ribosome assembly and translation. p26 is a strong RNA-binding protein and has been shown to non-specifically sequester RNAs into p26 condensates in vitro.[65] Although p26 expression does not change overall rRNA levels, RNA immunoprecipitation followed by RT-qPCR (RIP-qPCR) revealed that p26 binds rRNAs with >80-fold greater affinity than free GFP (Figure 3.4A). Similarly, p26 pulled down GAPDH transcripts with over 220-fold higher affinity compared to GFP, indicating that p26 associates with both rRNAs and mRNAs. Next, we sought to determine whether p26 expression affects the solubility of rRNAs and mRNAs, potentially by sequestering them into insoluble p26 complexes. Alternatively, p26 expression could induce transcriptome-wide RNA condensation, a phenomenon observed during stress that facilitates the preferential translation of newly transcribed transcripts.[187] We first fractionated cell lysates to separate soluble and insoluble RNAs and proteins. p26 migrated to its expected molecular weight in the soluble fraction but formed high molecular weight complexes (~250 kDa) in the insoluble fraction (Figure 3.4B**,** Left). These complexes were directly visualized by confocal microscopy and appeared as rounded condensates (Figure 3.4B**,** Right). Interestingly, rRNAs and GAPDH mRNAs consistently shifted from the soluble to the insoluble fractions in p26-expressing plants compared to GFP controls. On average, rRNAs and GAPDH transcripts exhibited 10- to 100-fold greater enrichment in the insoluble fraction of

plants expressing p26 compared to those expressing GFP (Figure 3.4C). These results indicate that p26 expression reduces the solubility of rRNAs and mRNAs, either through direct binding and sequestration into p26 condensates or potentially through a non-specific decrease in RNA solubility related to cellular stress. Collectively, the decreased solubility and availability of ribosomal components likely impair monosome formation and translation during p26 expression and the later stages of PEMV2 infection.

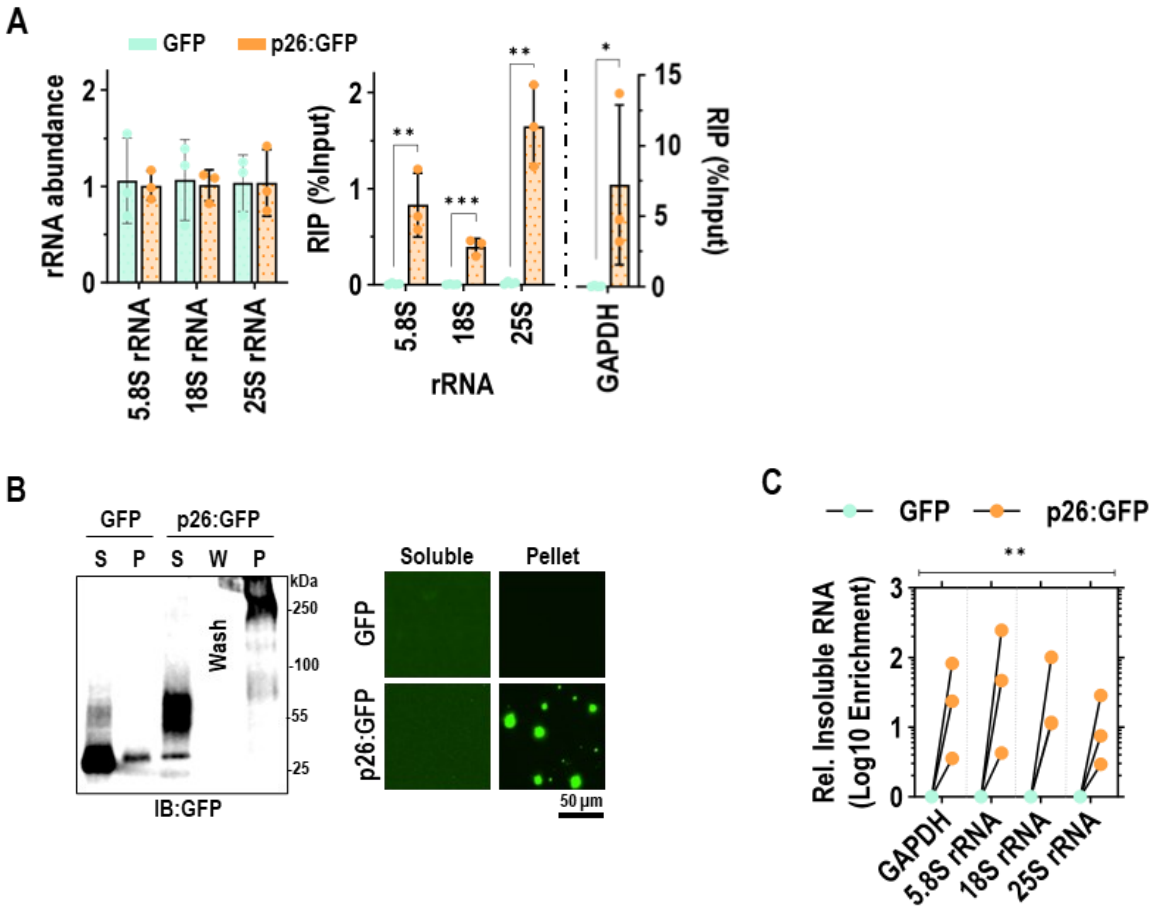

Figure 3.4 p26 directly binds and sequesters rRNAs into insoluble condensates

(**A**) RT-qPCR shows no significant difference between rRNA levels in GFP or p26:GFP samples. RIP-qPCR was used to measure binding between p26:GFP and rRNAs or GAPDH mRNAs. * $P<0.05$; ** $P<0.01$; *** $P<0.0001$ unpaired t test. (**B**) Soluble and insoluble (pellet) fractions were separated from *N. benthamiana* leaves expressing GFP or p26:GFP. Anti-GFP antibodies were used for western blotting. Fractions were directly visualized using confocal microscopy. (**C**) Relative levels of rRNAs and GAPDH mRNAs were measured by RT-qPCR using the ΔC_q method, comparing total RNA to insoluble RNA in the pellet fraction. A before-after plot shows the relative Log10 insoluble RNA levels from GFP- and p26-expressing plants from three independent experiments. ** $P<0.01$ Ratio paired t test.

Discussion

Our study provides new insights into how viral condensates can influence basic cellular processes like translation. p26 condensates are enriched in ribosomal proteins and p26 directly binds rRNAs, sequestering them into high molecular weight complexes thereby reducing their solubility (Figures 3.1 and 3.4). Puromycin incorporation assays and polysome profiling in *N. benthamiana* demonstrate that p26 expression suppresses global translation and ribosome assembly (Figure 3.2). Ribosome assembly was also disrupted in PEMV2-infected plants but was partially restored in a mutant strain lacking p26 expression, confirming the role of p26 in inhibiting ribosome assembly and translation. The incomplete recovery of ribosome assembly by the mutant virus may be attributed to the presence of RNA elements in the 3' untranslated region (UTR) of PEMV2. PEMV2 RNAs contain 3' cap-independent translational enhancers (3' CITEs) that recruit ribosomal subunits and translation initiation factors to the 3' ends of viral RNAs.[188] One such element, the Panicum mosaic virus translation element (PTE), enables eukaryotic initiation factor 4E (eIF4E) recognition and cap-independent translation.[189] We speculate that elevated levels of PEMV2 RNAs during late infection stages may also contribute to translational repression. In this context, 3' CITEs could sequester ribosomes and associated factors, reducing their availability for translating cellular mRNAs.

p26 shares several similarities with the *Phytophthora infestans* effector protein Pi23226. Both localize to the nucleolus, associate with ribosomal proteins and RNAs, and suppress global translation in *N. benthamiana*.[190] However, unlike Pi23226, which

disrupts pre-rRNA processing, our RiboMethSeq experiments demonstrate that p26 does not affect rRNA methylation or processing (Figure 3.3). Translational repression profiles similar to those observed with p26, characterized by reduced monosome and polysome formation, have been reported during proteotoxic stress, expression of aggregation-prone peptides, and chronic stress.[191] Given the intrinsic disorder [65] and insolubility of p26 (Figure 3.4), we hypothesize that its high expression levels could create a proteotoxic challenge, leading to translational repression. Finally, our results provide a possible explanation for previous research reporting that p26 inhibits the co-translational NMD pathway.[106] Here, global suppression of translation by p26 likely counteracts RNA surveillance activity by upframeshift 1 (UPF1) and the NMD machinery.[192]

p26 non-specifically binds RNAs, and its expression induces significant changes in rRNA and mRNA solubility after condensation (Figure 3.4). It is unclear whether this reduced solubility results from direct co-condensation with p26 or reflects a broader cellular response to translational repression and stress.[34] Regardless, we hypothesize that increased condensation of rRNAs and mRNAs during p26 expression contributes to defects in ribosome assembly and translation. Our data indicates that p26 suppresses translation during the later stages of infection. While we have not specifically measured the translational efficiency of viral RNAs during the late stages of PEMV2 infection, we suspect that PEMV2 RNAs are not immune to the translational repression caused by p26. Instead, we hypothesize that reduced global translation facilitates the formation of movement-competent ribonucleoprotein (RNP)

complexes comprising PEMV2 RNAs, p26, and fibrillarin. This hypothesis is supported by two key observations: i) p26 is expressed from a subgenomic RNA only after RNA replication, making it less abundant in early infection stages [193]; and ii) p26 condensate formation is concentration-dependent, occurring only when p26 levels exceed a critical threshold (C_{sat}) for condensation [65]. Given p26's non-specific RNA binding and its association with ribosomal proteins, we propose that p26 induces condensation of ribosomal components and cellular transcripts late in infection. This suppression of global translation likely aids in virus movement, a process that is incompatible with active translation (see Figure 3.5 for model).

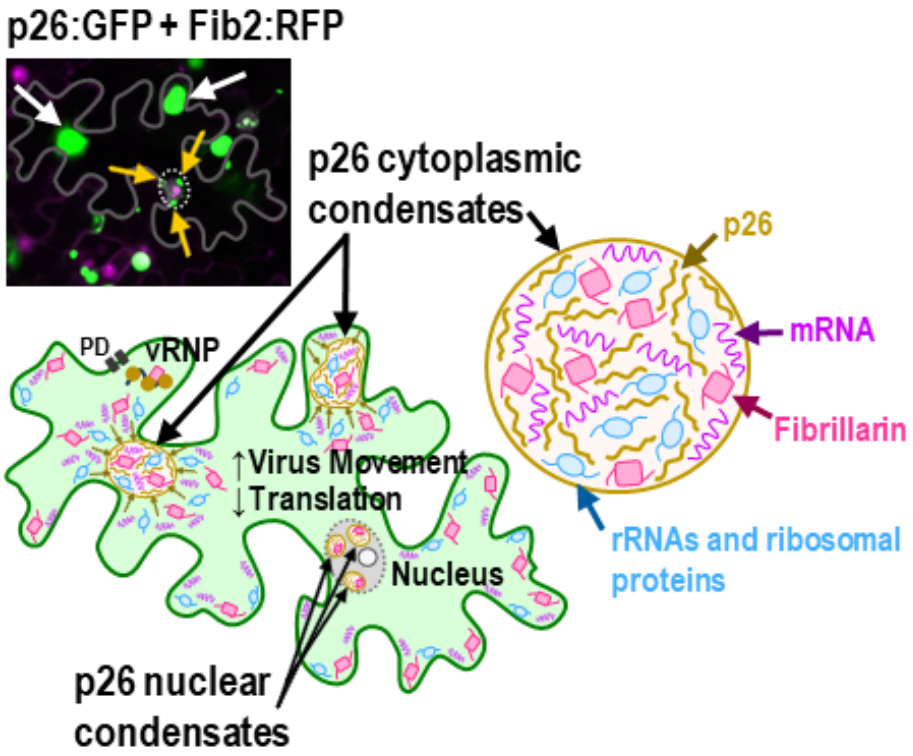

Figure 3.5 Translational repression via p26-mediated sequestration of biomolecules

Proposed model for how p26 condensates sequester translation-associated biomolecules and suppress translation. Inset shows *N. benthamiana* cell expressing p26:GFP and Fib2:RFP. Yellow and white arrows denote nuclear and cytoplasmic condensates, respectively. Sequestration of rRNAs and ribosomal proteins into p26 condensates limits ribosome association with viral RNAs and favors viral ribonucleoprotein (vRNP) complex formation consisting of PEMV2 RNAs, p26, and Fib2. vRNPs can move through plasmodesmata (PD) to move cell-to-cell and establish systemic infections.

Conclusion

Our study highlights how condensates formed during PEMV2 infection can disrupt basic cellular processes. We demonstrate that p26 condensates sequester ribosomal proteins and rRNAs, leading to defects in ribosome assembly and global translation suppression. This translational repression could function as a switch to promote the formation of ribonucleoprotein complexes, enabling viral RNA trafficking and systemic spread. These findings contribute to the broader understanding of how viruses exploit phase separation mechanisms to sequester host machinery, a strategy that is increasingly recognized as a key aspect of viral replication and pathogenicity in diverse virus families.[194]

Materials & Methods

Construction of yeast and plant expression plasmids. For yeast expression, free GFP or p26:GFP were expressed from pYES2 vectors (Invitrogen, Cat No. V825-20) containing the yeast *GAL1* promoter which allows for galactose-inducible and glucose-repressible protein expression in *S. cerevisiae*. GFP was PCR-amplified with forward and reverse primers designed to adjoin *BamH*I and *Xho*I restriction sites, respectively. GFP was digested with *BamH*I and *Xho*I restriction enzymes then ligated into the corresponding restriction sites of pYES2 to create pYES2-GFP. PCR-amplification of p26:GFP from previously reported constructs [65] was accomplished using a forward primer and reverse primer to add *BamH*I and *Xba*I restriction sites, respectively. Following digestion, p26:GFP was cloned into the

corresponding restriction sites of pYES2 to generate pYES2-p26:GFP. Ligation for both constructs was achieved using T4 DNA Ligase (New England BioLabs; Ipswich, Massachusetts) according to the manufacturer's protocol. Binary plasmids containing the Cauliflower mosaic virus (CaMV) duplicated 35S promoter were utilized to express constructs in *N. benthamiana* plants. The pBIN61S vector was used to express p14, GFP, or p26:GFP downstream of the CaMV 35S promoter. pBIN-p14 contains the silencing suppressor p14 from Pothos latent virus and has been previously reported.[113] pBIN-GFP, pBIN-p26:GFP, and binary PEMV2 vectors have been previously described.[29, 65, 145] An entry clone for Fibrillarin 2 (AT4G25630, pENTR223) was obtained from the Arabidopsis Biological Resource Center (ABRC, Columbus, Ohio) and used to transfer Fib2 into the destination vector pGWB555 using Gateway LR Clonase II enzyme (Invitrogen, Waltham, Massachusetts) to create an N-terminal mRFP fusion following the CaMV 35S promoter (pGWB555 was a gift from Tsuyoshi Nakagawa) (Addgene plasmid # 74885).[195] Virus-induced gene silencing (VIGS) vectors pTRV1 (stock #: CD3-1039) and pTRV2 (stock #: CD3-1040) were acquired from ABRC. The Sol Genomics Network VIGS Tool [196] was used to determine the optimal sequence to target Fib2 in *N. benthamiana*. A double-stranded gene fragment (Azenta Life Sciences; South Plainfield, NJ) spanning nucleotides 207-506 of Fib2 cDNA (GenBank: AM269909.1) was designed with 5' *Xba*I and 3' *BamH*I restriction sites. This fragment was PCR-amplified, digested, and ligated into the multiple cloning site of pTRV2 using the respective restriction sites, generating pTRV2-Fib2. The

accuracy of the constructs was verified by Sanger sequencing. All primers used in this study are listed in Supplementary File 1 [174].

Condensate isolation and immunoprecipitation. pYES2-GFP or pYES2-p26:GFP constructs were transformed into *Saccharomyces cerevisiae* (BY4741) using the Frozen-EZ Yeast Transformation II kit (Zymo Research; Irvine, California). Cultures were grown in CSM^{URA-} (complete supplement mixture without uracil) supplemented with 2% glucose overnight at 30°C. Protein expression was induced by resuspending cell pellets in CSM^{URA-} supplemented with 2% galactose to an optical density at 600 nanometers (OD_{600}) of ~0.2, measured with a spectrophotometer UV5 Nano (Mettler Toledo; Columbus, Ohio). Cultures were incubated at 30°C for 6-8 hours and grown to log phase (OD_{600} of 0.4-0.6). Cells were pelleted at 3,000 x *g* for 2 minutes and the supernatant was discarded. Pellets were then snap-frozen in liquid nitrogen and stored at -80°C overnight. Cells were resuspended in lysis buffer (50 mM Tris HCl pH 7.4, 100 mM potassium acetate, 2 mM magnesium acetate, 0.5 mM dithiothreitol (DTT), 50 µg/mL heparin, 0.5% Nonidet P-40 (NP40), 1:5000 antifoam B, EDTA-free protease inhibitor tablet (Thermo Scientific, Cat no. A32955), RNase inhibitor) and transferred to a microcentrifuge tube on ice. Cells were lysed with acid-washed beads on a digital cell disruptor for 2 minutes followed by incubation on ice for 2 minutes (x2 cycles). All centrifuge steps were performed at 4°C unless otherwise stated. Cleared lysates were centrifuged at 16,800 x *g* for 10 minutes. The supernatant was discarded, and condensate-enriched pellets were washed with lysis buffer and

centrifuged at 14,000 x *g* for 10 minutes. Condensates were released from cell pellets by the addition of 2 M urea in lysis buffer followed by a low-speed spin at 900 x *g* for 2 minutes. Condensate-enriched supernatants were either imaged using a 63x objective (Zeiss LSM 510 Meta confocal microscope with Zen 2009 software) or stored at -80°C.

GFP-Trap agarose beads (Chromotek; Rosemont, Illinois) were equilibrated in lysis buffer + 2M urea and washed 2 additional times using a magnetic separation tube rack for buffer removal. Enriched condensates were diluted to 500 µL in cell lysis buffer + 2M urea and added to the equilibrated agarose beads (20 µL of the diluted condensates were collected and set aside as the input fraction). Immunoprecipitation was carried out per manufacturer's instructions using lysis buffer + 2M urea. The beads were resuspended in 2X Laemmli SDS buffer and incubated at 95°C for 10 minutes to dissociate complexes.

Mass spectrometry. The GFP lysate and the condensate fractions from GFP or p26:GFP samples were each collected, as described above, from three biological replicates and sent to MS Bioworks (Ann Arbor, Michigan) for LC-MS/MS analyses. A combination of short SDS-PAGE and in-gel trypsin digestion was used to prepare samples for nano LC-MS/MS using a Waters M-Class LC system interfaced to a ThermoFisher Fusion Lumos mass spectrometer. Data-dependent acquisition (DDA) mass spectrometry was conducted, operating the Orbitrap at 60,000 FWHM and 15,000 FWHM for MS and MS/MS, respectively. Mascot (Matrix Science) was used

to search the UniProt *Saccharomyces cerevisiae* database. Scaffold (Proteome Software) was used to generate a non-redundant list of the identified proteins for each sample. The data was filtered using a 1% false-discovery rate (FDR) for proteins and peptides, and two unique peptides were required per identified protein. To compare log2 fold change values, an imputation of 0.2 was applied to replicates that had 0 spectral counts for an identified protein. The normalized spectral abundance factor (NSAF) was calculated for each protein using the spectral counts (SpC), molecular weight of the protein (MW, reported in kDa), and the total number of proteins (N) applied to this equation: $NSAF = (SpC/MW)/\Sigma(SpC/MW)_N$.

Protein synthesis assay and flow cytometry. Transformed BY4741 strains were cultured in CSM^{URA-} supplemented with 2% glucose and incubated overnight at 30°C. Protein expression was induced as detailed earlier for condensate isolation. Cultures were adjusted to a starting OD_{600} of 0.3 and incubated at 30°C for 6-8 hours until an OD_{600} of 0.6-0.8 was reached. Cells were pelleted at 1,800 x *g* for 5 minutes and washed 3 times with $CSM^{MET-/URA-}$ (CSM that does not contain methionine or uracil) + 2% galactose. The pellet was resuspended in the wash medium and incubated at 30°C for 30 minutes, followed by centrifugation at 1,800 x *g*. The cells were resuspended in Click-iT® working solution ($CSM^{MET-/URA-}$, 2% galactose, 50 µM Click-iT® HGP reagent) and incubated at 30°C for 30 minutes. Cells were pelleted and washed with 1X PBS (phosphate buffered saline), resuspended in 1X PBS + 3.7% formaldehyde, and incubated at room temperature for 15 minutes. Samples were

washed and prepared for flow cytometry following the manufacturer's protocol (Click-iT™ HPG Alexa Fluor™ 594 Protein Synthesis Assay Kit). A BD FACSCalibur (BD Biosciences) flow cytometer was used to measure incorporated HPG (L-homopropargylglycine, a methionine analog) into proteins during protein synthesis. 10,000-100,000 cells were analyzed for both HPG incorporation and GFP expression.

Growth curves. Liquid cultures of BY4741 expressing either GFP or p26:GFP were started from a single colony in CSM^{URA-} supplemented with 2% glucose and grown overnight at 30°C with gentle agitation. Cells were pelleted and resuspended in CSM^{URA-} supplemented with either 2% glucose or 2% galactose to an OD_{600} of 0.4. The culture was then diluted 4-fold in a 96-well plate containing the previously specified media to a final OD_{600} of 0.1. Plates were incubated in the BioTek Synergy H1 Multimode Reader (Agilent; Santa Clara, California) for 36 hours at 30°C with constant shaking. OD_{600} and fluorescence readings (488 nm) were recorded at 20-minute intervals using the BioTek Gen5 software (Agilent; Santa Clara, California).

Agroinfiltration. Binary constructs were transformed into C58C1 agrobacterium via electroporation. Cultures were grown in Luria Broth (LB) medium with applicable antibiotics at 30°C overnight before passaging into fresh media with antibiotics and 20 μM acetosyringone. Following overnight incubation, cultures were centrifuged and resuspended in (10 mM $MgCl_2$, 10 mM MES-K (2-morpholinoethanesulphonic acid potassium) pH 5.6**,** 100 μM acetosyringone). The

OD_{600} was measured using spectrophotometer UV5 Nano (Mettler Toledo; Columbus, Ohio) and diluted to the appropriate optical density in the resuspension buffer. To promote transient gene expression, the silencing suppressor p14 from Pothos latent virus was added to all agroinfiltration solutions at a final OD_{600} of 0.2, unless otherwise noted. pBin-GFP, pBin-p26:GFP and pGWB555-Fib2:RFP were infiltrated at an OD_{600} of 0.4, whereas the viral constructs pCB-PEMV2 and pCB-PEMV2Δp26 were infiltrated at an OD_{600} of 0.2. For VIGS experiments, empty pTRV2 (control) or pTRV2-Fib2 was infiltrated in conjunction with pTRV1 at a final OD_{600} of 0.4, as previously reported.[197] The silencing suppressor p14 was excluded from all VIGS infiltrations. Solutions were incubated at room temperature for 2 hours prior to infiltration into the underside of *N. benthamiana* leaves using a 1 mL syringe. *N. benthamiana* plants were grown at 25°C following a 12-hour light/dark cycle at 65% relative humidity in a growth chamber (Caron; Wernersville, Pennsylvania) with an LED light intensity of 250 μmol $m^{-2}s^{-1}$.

Puromycin incorporation and western blotting. *N. benthamiana* leaves were collected at 2 dpi following agroinfiltration. Leaves were lacerated and placed into a clear 6-well culture plate before resuspension in 4 mL of Murashige & Skoog buffer (½ MS medium, 1% sucrose, 100 μM puromycin). Tissue fragments were subject to vacuum infiltration for 2 hours and then washed with 1X PBS. Vacuum-infiltrated leaf tissue was then snap-frozen with liquid nitrogen, ground into a fine powder, and resuspended in a buffer containing 1X Tris-buffered saline (TBS), 3% 2-

mercaptaoethanol and supplemented with protease inhibitors (Thermo Scientific, Cat no. A32955). Proteins were separated via 10% SDS-PAGE and transferred to a nitrocellulose membrane. Membranes were treated with Ponceau S for 2 minutes to stain for the rubisco large subunit (loading control). Membranes were blocked in 1X TBS-T+BSA (TBS, 0.1% Tween 20, 3% BSA) for 2-4 hours at room temperature prior to incubation with the primary antibody (1:10,000 anti-GFP [Invitrogen, Cat No. PA1-980A] or 1:25,000 anti-puromycin [MilliporeSigma, Cat No. MABE343]) overnight at 4°C with gentle agitation. Membranes were washed and incubated with Invitrogen horseradish-peroxidase (HRP) conjugated secondary antibodies (1:10,000 dilution) for 45 minutes at room temperature. Blots were washed and visualized using SuperSignal™ West Pico PLUS Chemiluminescent Substrate (Thermo Scientific). Blots were imaged using the Azure 600 biosystem or the Bio-Rad ChemiDoc MP Imaging System.

Polysome profiling and RNA enrichment analyses. 7 to 47% (w/v) sucrose gradients (20 mM Tris-HCl pH 7.5, 60 mM KCl, 10 mM $MgCl_2$, 1 mM DTT) were prepared in 5 layers (7%, 17%, 27%, 37%, and 47%) in 13.2 mL ultracentrifuge tubes (Beckman Coulter; Brea, California), snap-frozen in liquid nitrogen and stored at -80°C. Gradients were thawed at 4°C 12-36 hours prior to use. Leaves were collected at 3 dpi (GFP, p26:GFP) or 5 dpi (PEMV2, PEMV2Δp26). Infiltrated leaf tissue was ground in liquid nitrogen with a mortar and pestle and resuspended in polysome extraction buffer (20 mM Tris-HCl pH 7.5, 60 mM KCl, 10 mM $MgCl_2$, 1 mM DTT, 5.26

mM EGTA, 0.5% NP40, 0.2 mg/mL heparin, 50 µg/mL cycloheximide, 50 µg/mL chloramphenicol) + RNase inhibitors and incubated on ice for 10 minutes. Lysates were filtered using 60 µm nylon mesh before centrifugation at 16,000 x *g* for 15 minutes at 4°C. Lysate supernatants were collected, and pellets were resuspended with a pipette in lysis buffer and kept on ice for later use. Lysate supernatants were added in equal amounts to each gradient tube. Samples were subject to ultracentrifugation with the Beckman Optima L-90K Ultracentrifuge (Beckman Coulter; Brea, California) at 32,000 rpm for 2 hours and 45 minutes at 4°C in a SW41-Ti rotor (Beckman Coulter; Brea, California). 200 µL fractions were collected from the uppermost layer and added sequentially to each well in a pre-chilled UV-Star 96-well plate (Greiner Bio-One; Monroe, North Carolina) until the entire gradient had been aliquoted. The absorbance for each sample was measured at 260 nm using a BioTek Synergy H1 Multimode Reader (Agilent; Santa Clara, California). GraphPad Prism version 10 was used to create a polysome profile by plotting the measured absorbance values (OD_{260}) versus each fraction of the gradient followed by 4^{th} order smoothing. Each polysome curve represents the mean absorbance values between replicates.

RiboMethSeq. Infiltrated leaf tissue was collected at 3 dpi for PEMV2 and 11 dpi for VIGS samples. Total RNA was isolated from 100 mg of leaf tissue and on-column DNase treated using the RNeasy Plant Mini Kit (Qiagen; Hilden, Germany) according to the manufactures protocol. RNAs were fragmented by adding 500-800

ng of total RNA to bicarbonate buffer (pH 9.2) and incubated at 95°C for 8 minutes before ethanol precipitation and purification. RNAs were end-repaired by dephosphorylating the 3' ends using Antarctic phosphatase (New England BioLabs; Ipswich, Massachusetts) according to the manufacturer's protocol. 5' ends were phosphorylated using T4 PNK (New England BioLabs; Ipswich, Massachusetts) before purifying RNA fragments with the RNeasy MinElute Cleanup Kit (Qiagen; Hilden, Germany). RNA fragmentation was confirmed by visualizing RNA fragments following gel electrophoresis. small RNA (sRNA) libraries were generated at the University of Missouri Genomics Technology Core. Libraries were sequenced on the Illumina NovaSeq S4 platform (PE100) with 30 million reads per sample. Raw sequencing reads and processed data are publicly available for download from the Gene Expression Omnibus (GEO, NCBI) under accession GSE275487.

Bioinformatics and RiboMethScore calculations. Trimmed FASTQ files (paired-end) were mapped against either fully processed rRNAs or the 45S precursor (Genbank: KP824745.1) from *N. benthamiana* using Bowtie2 [198] with end-to-end (--very-fast) presets. Normalized read counts across the 45S precursor were calculated by normalizing raw read counts (samtools depth) with the largest mean in each data set as 100%. Mean normalized coverage of rRNA precursor regions (e.g., 5' ETS, ITS1, etc.) were calculated using the mean normalized read counts for each respective region. Coverage of 5' and 3' ends was calculated from positive-strand reads using the bedtools Genome Coverage tool.[199] The positions of 5' end reads

were adjusted to the -1 position before calculating total 5' and 3' end read counts for each rRNA position. A custom MATLAB script was used to calculate RiboMethScores from total end counts using the following equation as previously reported by Galvanin *et. al*.[200]

$$\mathrm{RiboMethScore} = 1 - ni/(0.5 * (\frac{\mathrm{SUM}(nj * Wj)}{\mathrm{SUM}(Wj)} + \frac{\mathrm{SUM}(nk * Wk)}{\mathrm{SUM}(Wk)})$$

Briefly, *ni* is the total number of 5' and 3' end reads at each position. *j* varies *i*-2 to *i*-1 whereas *k* varies from *i*+1 to *i*+2 positions. Weight parameters were set at 1.0 and 0.9 for the -1/+1 and -2/+2 positions, respectively.

RIP-qPCR and rRNA binding analyses. *N. benthamiana* leaves agroinfiltrated with pBIN-GFP or pBIN-p26:GFP were collected at 2 dpi. Samples were ground in liquid nitrogen with a mortar and pestle and suspended in 1 mL of lysis buffer (50 mM Tris-HCl pH 7.5, 150 mM NaCl, 10 mM $MgCl_2$, 10% glycerol, 1 mM EDTA, 5 mM DTT, 1% Triton™ X-100) and incubated on ice for 30 minutes. A portion of each lysate was aliquoted and set aside on ice as an input sample. Cleared lysates were added to the GFP-Trap beads and mixed end-over-end at 4°C for 1 hour. The beads were washed 3 times with lysis buffer and RNA was extracted from both the input fractions and the agarose beads using TRIzol (ThermoFisher Scientific; Waltham, Massachusetts). After RNA immunoprecipitation (RIP), a one-step reverse-transcriptase quantitative PCR (RT-qPCR) was conducted on input or IP RNAs using

the NEB Luna® Universal One-Step RT-qPCR SYBR Green Kit (New England BioLabs, Ipswich, MA). Primers targeting *N. benthamiana* GAPDH, 5.8S rRNA, 18S rRNA, 25S rRNA, and PEMV2 gRNA are listed in Supplementary File 1 [174]. RT-qPCR experiments were completed using the Bio-Rad CFX Connect Real-Time PCR Detection System and analyzed using Bio-Rad CFX Maestro software. The RNA IP fractions were normalized to the RNA input fractions using the equation: $\Delta Ct_{Normalized\_RIP} = Ct_{IP} - (Ct_{input} - Log_2 (DF))$ where DF is the dilution factor of the input. The percent input was calculated for each sample using the equation: $\%Input = 2^{(-\Delta Ct[Normalized\ RIP])}$. Graphs were generated using GraphPad Prism version 10.

CHAPTER 4

4. CONCLUSION

Previous work with GRV and PEMV2 movement proteins noted large cytoplasmic inclusion bodies containing ORF3 and p26, respectively, during infection.[29, 31] We first sought to demonstrate that these inclusion bodies were biomolecular condensates formed as a result of p26 phase separation. At the time, research pertaining to phase separation in plants was centered on host condensates, thus, research into the role of phase separation in plant virus-host interactions was almost non-existent. Biomolecular condensates are typically characterized as dynamic and comprised primarily of proteins and RNA.[33] Our results demonstrate that p26 phase separation is driven by electrostatic interactions in the N-terminal IDR of p26, leading to the formation of viscous and poorly dynamic viral condensates. In support of this, disruption of charged residues in the IDR restricted or abolished p26 phase separation. Moreover, our findings suggest that p26 phase separation plays a key role in facilitating virus-host protein-protein interactions, the formation of vRNPs, and systemic virus movement. Overall, this work undoubtedly demonstrates the importance of phase separation in promoting virus infections, an idea that had not been previously investigated for plant virus-host interactions.

Phase separation can be used by a virus to perpetuate a virus infection, as is the case with p26 and Fib2; however, host cells may respond in kind, using phase separation as a tactic for the anti-viral response. Our findings showed that p26 and G3BP1 can co-partition into condensates during a virus infection, we aimed to determine if this phenomenon exerted pro-viral or anti-viral effects. G3BP1 is a host RNA-binding protein that plays a major role in the assembly of stress granules and is involved in the immune response, mRNA stability, and translation.[201] As a key multifunctional protein with reports of pro-viral and anti-viral roles, G3BP1 is a notorious target for viruses.[201] We found that PEMV2 infection correlates with increased G3BP1 expression and G3BP1 overexpression restricts PEMV2 accumulation; suggesting that, for PEMV2 infections, elevated G3BP1 expression is likely part of the anti-viral response by the host. Overexpression of a phase separation-deficient G3BP1 mutant during infection partially restored PEMV2 accumulation, implying that phase separation is a requirement for G3BP1 to exert the most severe anti-viral effect. Investigating the mechanics of phase separation and the conditional biomolecular requirements for condensate formation is imperative to deepen our understanding of intracellular virus-host interactions. This work supports the idea that phase separation is a tactic employed by host cells to restrict an infection and reveals the significance of host protein phase separation in the anti-viral response.

The next aim of our research was to determine the composition of p26 condensates and what role they may play during an infection. Virus-induced

membraneless condensates are often associated with -sense RNA virus replication factories, thus the function and composition of viral condensates formed by +sense RNA viral proteins were largely unexplored. We found that p26 condensates were enriched with Fib2 and ribosomal proteins, and had a unique composition compared to cytoplasmic host condensates, like stress granules and p-bodies. Despite this, gene ontology of our top hits revealed associations with translation, RNP complexes, and ribosome biogenesis. Further analyses concluded that overexpression of p26 repressed global translation in yeast (>10%) and plants (~42%). In support of this, we identified a significant decrease in monosome formation for p26-expressing samples, which was validated during a PEMV2 infection and consistent with our later findings that a PEMV2 mutant, lacking p26, partially rescued monosome formation. Interestingly, a key factor in the ribosome biogenesis process is Fibrillarin, a 2'-*O*-methyltransferase that modifies rRNA and an essential host protein usurped by umbravirus vRNPs.

It's well-established that umbravirus movement proteins, like p26 or ORF3, interact with fibrillarin, as confirmed by our co-localization, mass spectrometry, and co-IP results. We aimed to determine if p26-mediated sequestration of Fib2 into cytoplasmic condensates affected the 2'-*O*-methyltransferase activity of fibrillarin and thus, ribosome biogenesis. Analysis of 2'-*O*-methylation by RiboMeth-Seq, which provides single nucleotide resolution, showed no significant difference in the 2'-*O*-methylation of rRNA for mock-infected and PEMV2-infected samples. Our data also showed that rRNA abundance and rRNA processing were not altered in p26-expressing samples.

However, our data did suggest that p26 seemingly binds rRNA and GAPDH transcripts with a higher affinity than control samples, which was further supported by the increased levels of insoluble rRNA and GAPDH in p26-expressing samples. Therefore, we propose that p26 sequesters mRNA, rRNA, fibrillarin, and ribosomal proteins into cytoplasmic condensates, thereby limiting the availability and accessibility of fundamental translation factors. This phenomenon may function as a mechanism to promote virus trafficking, a process that is incompatible with translation.

It's well-known that viruses hijack host translation factors to promote infection. Viral proteins encoded by DENV and Yellow fever virus (YFV) have been shown to bind translation initiation factors to promote viral RNA translation.[202] Likewise, translation elongation factors have been reported as indispensable for WNV and YFV infections.[202] However, what role phase separation and +sense RNA virus-induced condensates might play in modulating host cellular processes, like translation, had not been investigated prior to this work. Multiple viral proteins from DENV have been shown to localize to membraneless organelles.[203] For example, the DENV capsid protein and non-structural protein 5 (NS5) have both been reported to partition in the nucleolus.[203] In accordance with our findings, research with DENV found that the viral NS1 protein interacts with more than 30 ribosomal proteins.[51] Interestingly, ribosomal protein L18 (RPL18) was identified as an NS1-interactor [51] and was among the top 20 p26-interactors identified in our screen. These findings lend support to our model, that proteins encoded by +sense RNA viruses may entrap ribosomal proteins and other

translation factors into viral condensates, limiting the host's accessibility to these factors.

Phase separation is an exciting topic that is proving to be a cornerstone in the facilitation of cellular processes. In plants, research into phase separation has been focused on flowering, immunity and the stress response.[63] The research herein explored the role of phase separation in mediating virus-host interactions in plants, a concept that, prior to this work, was unexplored. Furthermore, we characterized the composition of biomolecular condensates generated by a +sense viral protein. Membraneless organelles formed by viral proteins have long been associated with virus replication. However, this work reveals translation repression as a potential function for cytoplasmic viral condensates that might aid virus movement. Moreover, this research provides a foundation for future investigations into the function and composition of +sense RNA virus-induced biomolecular condensates. These findings represent a pivotal step forward in understanding the complexities of phase separation in virus-host interactions.

Supplemental Figures, Chapter 2

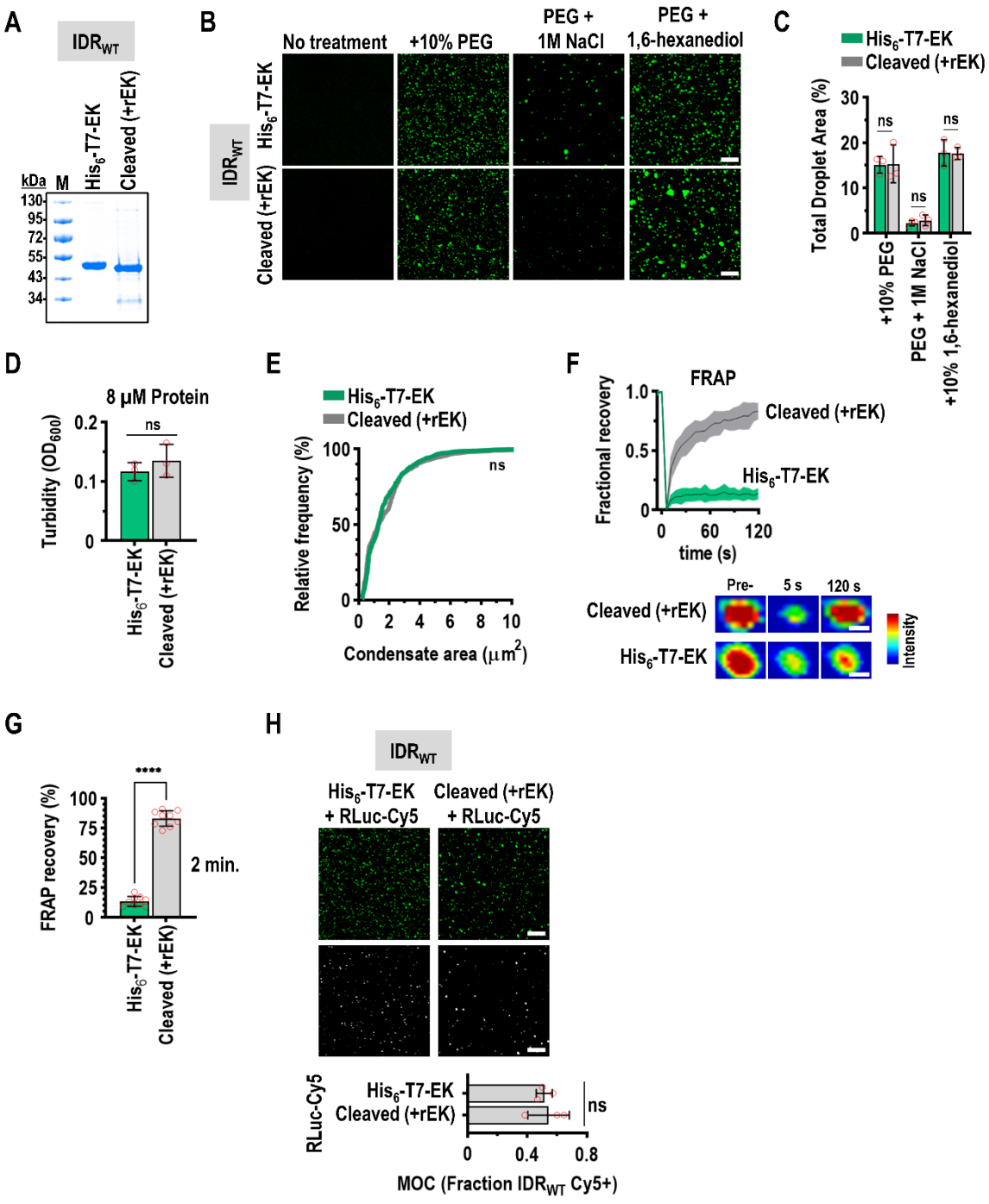

Figure S.1 Characterization of His-tagged and untagged IDRWT

(**A**) Coomassie-stained SDS-PAGE gel shows expected subtle downward shift by IDR_{WT} following His-tag cleavage with recombinant enterokinase (rEK). (**B**) Untagged or tagged IDR_{WT} droplet formation was monitored under various conditions by confocal microscopy. Bar scale: 20 μm. (**C**) Total droplet areas (%) were measured from confocal images using ImageJ. Error bars denote standard deviations and data points represent individual 20x fields (3 total). ns: not significant by two-way ANOVA and Sidak's multiple comparisons test. (**D**) *In vitro* turbidity assays (OD_{600}) were performed with 8 μM tagged or untagged IDR_{WT}. Three biological replicates are shown (red circles). ns: not significant by unpaired t test. (**E**) Particle sizes of tagged and untagged IDR_{WT} droplets from three 20x fields were measured using ImageJ. ns: not significant by two-tailed Mann-Whitney rank test. (**F**) Droplet dynamics of His-tagged and untagged IDR_{WT} were measured by FRAP. Results are from 9 FRAP experiments with shaded areas representing standard deviations for each condition. Representative droplets and heat map overlays are shown for each construct. (**G**) End-point (2 min.) FRAP recoveries were compared between tagged and untagged IDR_{WT}. Error bars denote standard deviations and data points represent individual FRAP experiments (9 total) ****P<0.0001 unpaired t test. (**H**) RLuc-Cy5 RNAs were mixed with tagged and untagged IDR_{WT} at a 1:500 RNA:protein ratio. The fraction of IDR_{WT} signal that was positive for Cy5-labelled RNA was determined by Mander's Overlap Coefficient (MOC) analysis. Error bars denote standard deviations and data points represent individual 20x fields. ns: not significant by unpaired t test.

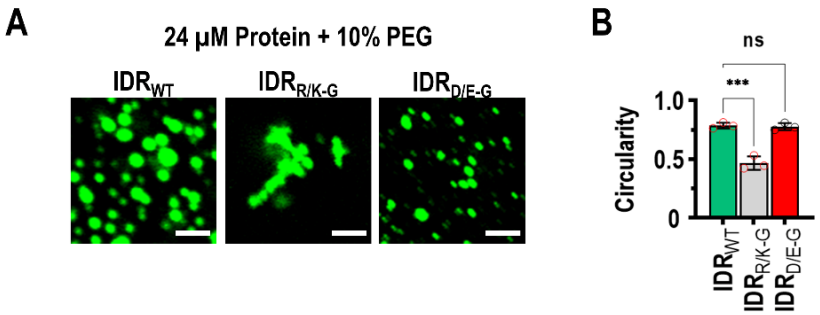

Figure S.2 Aggregate formation by R/K-G

(**A**) 24 μM protein was mixed with 10% PEG-8000 to induce phase separation in standard assay buffer. Droplet or aggregate formation was visualized by confocal microscopy. Bar scale: 5 μm. (**B**) Individual droplets or aggregates were assessed for circularity using ImageJ. Data points represent individual 20x fields and error bars denote standard deviations. ***P<0.001, ns: not significant by one-way ANOVA with Dunnett's multiple comparisons test.

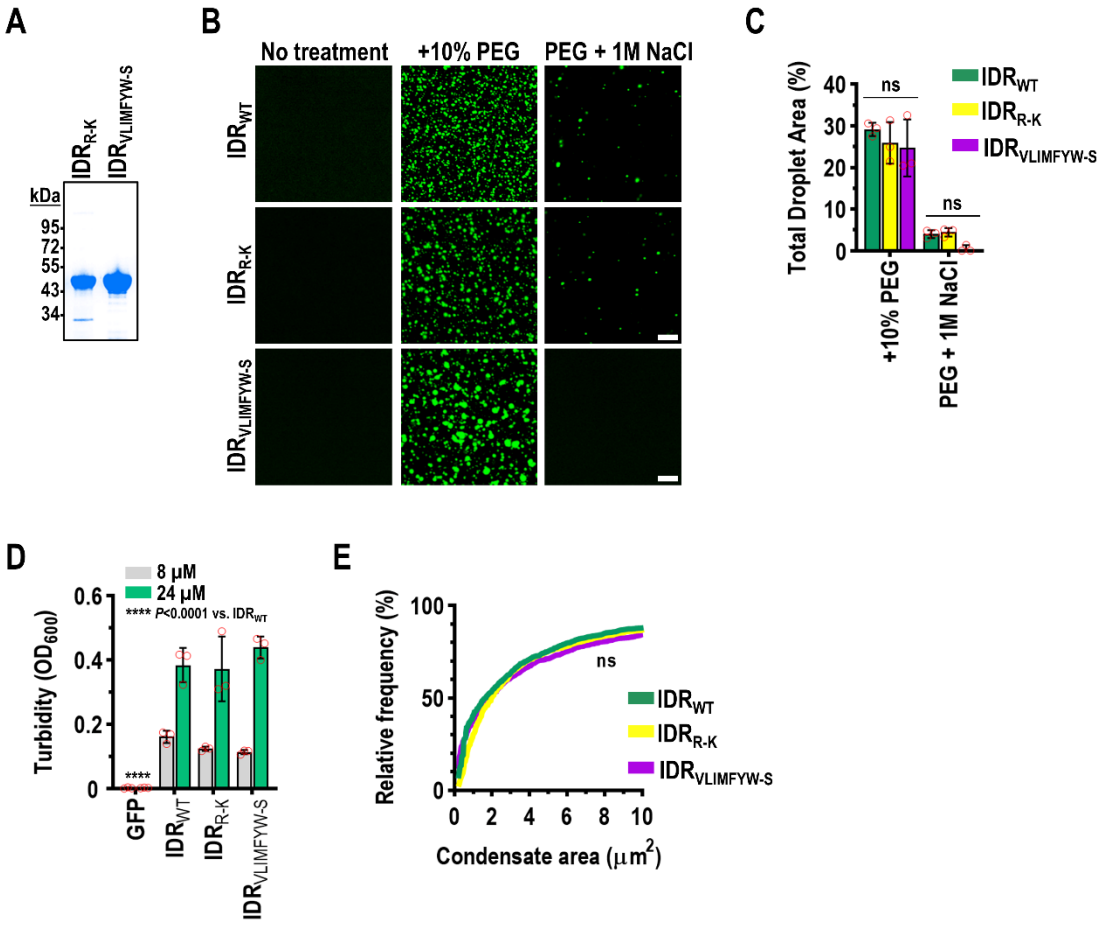
A
B
C
D
E
No treatment
+10% PEG
PEG + 1M NaCl
kDa
95
72
55
43
34
ns
Total Droplet Area (%)
8 μM
24 μM
**** P<0.0001 vs. IDR_WT
Turbidity (OD600)
GFP
Relative frequency (%)
Condensate area (μm²)

Figure S.3 Cation-pi and hydrophobic interactions do not influence p26 phase separation

(**A**) SDS-PAGE analysis of Coomassie-stained recombinant $IDR_{R\text{-}K}$ and $IDR_{VLIMFYW\text{-}S}$. Marker weights are shown on left in kilodaltons (kDa). $IDR_{R\text{-}K}$ contains lysine substitutions for all arginines whereas $IDR_{VLIMFYW\text{-}S}$ contains serine substitutions for all hydrophobic residues. (**B**) Droplet formation by IDR_{WT}, $IDR_{R\text{-}K}$, and $IDR_{VLIMFYW\text{-}S}$ was visualized by confocal microscopy under crowding conditions with and without 1 M NaCl. (**C**) Total droplet areas were measured from three separate 20x fields for each condition (red circles). Error bars denote standard deviations. ns: not significant by two-way ANOVA and Sidak's multiple comparisons test. (**D**) Turbidity assays (OD_{600}) comparing GFP, IDR_{WT}, $IDR_{R\text{-}K}$, and $IDR_{VLIMFYW\text{-}S}$ phase separation propensities. Error bars denote standard deviations and data points represent biological replicates (3 total). **** $P<0.0001$ by two-way ANOVA with Dunnett's multiple comparisons test vs. IDR_{WT}. (**E**) Mean condensate sizes for $IDR_{R\text{-}K}$ and $IDR_{VLIMFYW\text{-}S}$ mutants and wild-type IDR_{WT} were plotted by cumulative distribution frequency. Particle sizes were measured from three representative 20x fields using ImageJ. ns: not significant, two-tailed Mann-Whitney tests compared to IDR_{WT}.

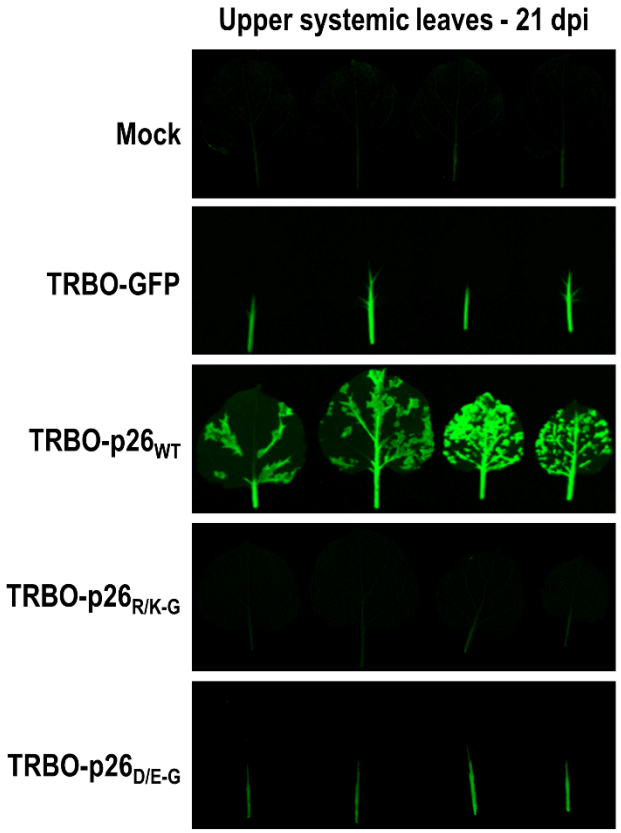

Figure S.4 Systemic trafficking of the TMV-based TRBO vector

At 21 dpi, upper *N. benthamiana* systemic leaves were imaged at 488 nm. TRBO-GFP and TRBO-p26$_{D/E-G}$ were mostly restricted to the petiole and midrib of systemic leaves. In contrast, TRBO-p26$_{WT}$ invaded the lamina of systemic leaves. Images are representative of three independent experiments with at least four plants for each condition.

REFERENCES

(1) National Research Council Committee on Examination of Plant Science Research Programs in the United States. Why Plant-Biology Research Today? In *Plant Biology Research and Training for the 21st Century*, National Academies Press (US), 1992.
(2) Veeresham, C. Natural products derived from plants as a source of drugs. *J Adv Pharm Technol Res* **2012**, *3* (4), 200-201. DOI: 10.4103/2231-4040.104709 From NLM.
(3) Wang, N.; Scherm, H. Key Discoveries in Plant Pathology During the Past Half Century: Impacts on the Life Sciences and on Plant Disease Management. *Phytopathology* **2023**, *113* (4), 588-593. DOI: 10.1094/phyto-02-23-0070-kd From NLM.
(4) Bentham, A. R.; De la Concepcion, J. C.; Mukhi, N.; Zdrzałek, R.; Draeger, M.; Gorenkin, D.; Hughes, R. K.; Banfield, M. J. A molecular roadmap to the plant immune system. *J Biol Chem* **2020**, *295* (44), 14916-14935. DOI: 10.1074/jbc.REV120.010852 From NLM.
(5) Jones, J. D. G.; Vance, R. E.; Dangl, J. L. Intracellular innate immune surveillance devices in plants and animals. *Science* **2016**, *354* (6316), aaf6395. DOI: 10.1126/science.aaf6395 (acccessed 2024/11/07).
(6) Noman, A.; Aqeel, M.; Lou, Y. PRRs and NB-LRRs: From Signal Perception to Activation of Plant Innate Immunity. *Int J Mol Sci* **2019**, *20* (8). DOI: 10.3390/ijms20081882 From NLM.
(7) Ting, J. P.; Lovering, R. C.; Alnemri, E. S.; Bertin, J.; Boss, J. M.; Davis, B. K.; Flavell, R. A.; Girardin, S. E.; Godzik, A.; Harton, J. A.; et al. The NLR gene family: a standard nomenclature. *Immunity* **2008**, *28* (3), 285-287. DOI: 10.1016/j.immuni.2008.02.005 From NLM.
(8) Felekkis, K.; Deltas, C. RNA Intereference: a powerful laboratory tool and its therapeutic implications. *Hippokratia* **2006**, *10* (3), 112-115. From NLM.
(9) Todd, J. N. A.; Carreón-Anguiano, K. G.; Islas-Flores, I.; Canto-Canché, B. Fungal Effectoromics: A World in Constant Evolution. *Int J Mol Sci* **2022**, *23* (21). DOI: 10.3390/ijms232113433 From NLM.
(10) Lechevalier, H. Dmitri Iosifovich Ivanovski (1864-1920). *Bacteriol Rev* **1972**, *36* (2), 135-145. DOI: 10.1128/br.36.2.135-145.1972 From NLM.
(11) Artika, I. M.; Wiyatno, A.; Ma'roef, C. N. Pathogenic viruses: Molecular detection and characterization. *Infect Genet Evol* **2020**, *81*, 104215. DOI: 10.1016/j.meegid.2020.104215 From NLM.
(12) Nathanson, N. The Human Toll of Viral Diseases: Past Plagues and Pending Pandemics. In *Viral Pathogenesis*, Copyright © 2016 Elsevier Ltd. All rights reserved., 2016; pp 3-16.
(13) Sudhan, S. S.; Sharma, P. Human Viruses: Emergence and Evolution. In *Emerging and Reemerging Viral Pathogens*, Copyright © 2020 Elsevier Inc. All rights reserved., 2020; pp 53-68.
(14) Bhadoria, P.; Gupta, G.; Agarwal, A. Viral Pandemics in the Past Two Decades: An Overview. *J Family Med Prim Care* **2021**, *10* (8), 2745-2750. DOI: 10.4103/jfmpc.jfmpc_2071_20 From NLM.
(15) Koonin, E. V.; Krupovic, M.; Agol, V. I. The Baltimore Classification of Viruses 50 Years Later: How Does It Stand in the Light of Virus Evolution? *Microbiol Mol Biol Rev* **2021**, *85* (3), e0005321. DOI: 10.1128/mmbr.00053-21 From NLM.
(16) Mahmoudabadi, G.; Phillips, R. A comprehensive and quantitative exploration of thousands of viral genomes. *Elife* **2018**, *7*. DOI: 10.7554/eLife.31955 From NLM.
(17) Payne, S. Introduction to RNA Viruses. In *Viruses*, Copyright © 2017 Elsevier Inc. All rights reserved., 2017; pp 97-105.

(18) Geng, G.; Wang, D.; Liu, Z.; Wang, Y.; Zhu, M.; Cao, X.; Yu, C.; Yuan, X. Translation of Plant RNA Viruses. *Viruses* **2021**, *13* (12). DOI: 10.3390/v13122499 From NLM.
(19) Walsh, D.; Mathews, M. B.; Mohr, I. Tinkering with translation: protein synthesis in virus-infected cells. *Cold Spring Harb Perspect Biol* **2013**, *5* (1), a012351. DOI: 10.1101/cshperspect.a012351 From NLM.
(20) Xiao, H.; Xu, L. H.; Yamada, Y.; Liu, D. X. Coronavirus Spike Protein Inhibits Host Cell Translation by Interaction with eIF3f. *PLOS ONE* **2008**, *3* (1), e1494. DOI: 10.1371/journal.pone.0001494.
(21) Relich Ryan, F.; Loeffelholz Michael, J. Taxonomic Changes for Human Viruses, 2020 to 2022. *Journal of Clinical Microbiology* **2022**, *61* (1), e00337-00322. DOI: 10.1128/jcm.00337-22 (acccessed 2024/09/16).
(22) Gaur, R. K.; Ali, A.; Cheng, X.; Mäkinen, K.; Agindotan, B.; Wang, X. Editorial: Plant Viruses, Volume II: Molecular Plant Virus Epidemiology and Its Management. *Frontiers in Microbiology* **2021**, *12*, Editorial.
(23) He, S.; Creasey Krainer, K. M. Pandemics of People and Plants: Which Is the Greater Threat to Food Security? *Mol Plant* **2020**, *13* (7), 933-934. DOI: 10.1016/j.molp.2020.06.007 From NLM.
(24) Zhao, Y.; Yang, X.; Zhou, G.; Zhang, T. Engineering plant virus resistance: from RNA silencing to genome editing strategies. *Plant Biotechnol J* **2020**, *18* (2), 328-336. DOI: 10.1111/pbi.13278 From NLM.
(25) Tatineni, S.; Hein, G. L. Plant Viruses of Agricultural Importance: Current and Future Perspectives of Virus Disease Management Strategies. *Phytopathology* **2023**, *113* (2), 117-141. DOI: 10.1094/phyto-05-22-0167-rvw From NLM.
(26) Folimonova, S. Y. Citrus tristeza virus: A large RNA virus with complex biology turned into a valuable tool for crop protection. *PLoS Pathog* **2020**, *16* (4), e1008416. DOI: 10.1371/journal.ppat.1008416 From NLM.
(27) Song, Y.; Hanner, R. H.; Meng, B. Transcriptomic Analyses of Grapevine Leafroll-Associated Virus 3 Infection in Leaves and Berries of 'Cabernet Franc'. *Viruses* **2022**, *14* (8). DOI: 10.3390/v14081831 From NLM.
(28) Gao, F.; Simon, A. E. Differential use of 3'CITEs by the subgenomic RNA of Pea enation mosaic virus 2. *Virology* **2017**, *510*, 194-204. DOI: 10.1016/j.virol.2017.07.021 From NLM.
(29) May, J. P.; Johnson, P. Z.; Ilyas, M.; Gao, F.; Simon, A. E. The Multifunctional Long-Distance Movement Protein of Pea Enation Mosaic Virus 2 Protects Viral and Host Transcripts from Nonsense-Mediated Decay. *mBio* **2020**, *11* (2). DOI: 10.1128/mBio.00204-20 From NLM.
(30) Taliansky, M. E.; Robinson, D. J. Molecular biology of umbraviruses: phantom warriors. *J Gen Virol* **2003**, *84* (Pt 8), 1951-1960. DOI: 10.1099/vir.0.19219-0 From NLM.
(31) Kim, S. H.; Ryabov, E. V.; Kalinina, N. O.; Rakitina, D. V.; Gillespie, T.; MacFarlane, S.; Haupt, S.; Brown, J. W.; Taliansky, M. Cajal bodies and the nucleolus are required for a plant virus systemic infection. *EMBO J* **2007**, *26* (8), 2169-2179. DOI: 10.1038/sj.emboj.7601674 From NLM.
(32) Kim, S. H.; Macfarlane, S.; Kalinina, N. O.; Rakitina, D. V.; Ryabov, E. V.; Gillespie, T.; Haupt, S.; Brown, J. W.; Taliansky, M. Interaction of a plant virus-encoded protein with the major nucleolar protein fibrillarin is required for systemic virus infection. *Proc Natl Acad Sci U S A* **2007**, *104* (26), 11115-11120. DOI: 10.1073/pnas.0704632104 From NLM.

(33) Parker, D. M.; Winkenbach, L. P.; Osborne Nishimura, E. It's Just a Phase: Exploring the Relationship Between mRNA, Biomolecular Condensates, and Translational Control. *Front Genet* **2022**, *13*, 931220. DOI: 10.3389/fgene.2022.931220 From NLM.
(34) Glauninger, H.; Wong Hickernell, C. J.; Bard, J. A. M.; Drummond, D. A. Stressful steps: Progress and challenges in understanding stress-induced mRNA condensation and accumulation in stress granules. *Mol Cell* **2022**, *82* (14), 2544-2556. DOI: 10.1016/j.molcel.2022.05.014 From NLM.
(35) Youn, J.-Y.; Dyakov, B. J. A.; Zhang, J.; Knight, J. D. R.; Vernon, R. M.; Forman-Kay, J. D.; Gingras, A.-C. Properties of Stress Granule and P-Body Proteomes. *Molecular Cell* **2019**, *76* (2), 286-294. DOI: 10.1016/j.molcel.2019.09.014 (acccessed 2024/09/16).
(36) Solis-Miranda, J.; Chodasiewicz, M.; Skirycz, A.; Fernie, A. R.; Moschou, P. N.; Bozhkov, P. V.; Gutierrez-Beltran, E. Stress-related biomolecular condensates in plants. *Plant Cell* **2023**, *35* (9), 3187-3204. DOI: 10.1093/plcell/koad127 From NLM.
(37) Alberti, S.; Gladfelter, A.; Mittag, T. Considerations and Challenges in Studying Liquid-Liquid Phase Separation and Biomolecular Condensates. *Cell* **2019**, *176* (3), 419-434.
(38) Wei, W.; Bai, L.; Yan, B.; Meng, W.; Wang, H.; Zhai, J.; Si, F.; Zheng, C. When liquid-liquid phase separation meets viral infections. *Front Immunol* **2022**, *13*, 985622. DOI: 10.3389/fimmu.2022.985622 From NLM.
(39) Boeynaems, S.; Alberti, S.; Fawzi, N. L.; Mittag, T.; Polymenidou, M.; Rousseau, F.; Schymkowitz, J.; Shorter, J.; Wolozin, B.; Van Den Bosch, L.; et al. Protein Phase Separation: A New Phase in Cell Biology. *Trends in Cell Biology* **2018**, *28* (6), 420-435.
(40) Banani, S. F.; Lee, H. O.; Hyman, A. A.; Rosen, M. K. Biomolecular condensates: organizers of cellular biochemistry. *Nature Reviews Molecular Cell Biology* **2017**, *18* (5), 285-298. DOI: 10.1038/nrm.2017.7.
(41) Ferreon, A. C.; Ferreon, J. C.; Wright, P. E.; Deniz, A. A. Modulation of allostery by protein intrinsic disorder. *Nature* **2013**, *498* (7454), 390-394. DOI: 10.1038/nature12294 From NLM.
(42) Ren, J.; Zhang, Z.; Zong, Z.; Zhang, L.; Zhou, F. Emerging Implications of Phase Separation in Cancer. *Advanced Science* **2022**, *9* (31), 2202855. DOI: https://doi.org/10.1002/advs.202202855 (acccessed 2024/11/07).
(43) Wiedner, H. J.; Giudice, J. It's not just a phase: function and characteristics of RNA-binding proteins in phase separation. *Nat Struct Mol Biol* **2021**, *28* (6), 465-473. DOI: 10.1038/s41594-021-00601-w From NLM.
(44) Luo, Y.; Na, Z.; Slavoff, S. A. P-Bodies: Composition, Properties, and Functions. *Biochemistry* **2018**, *57* (17), 2424-2431.
(45) Jain, S.; Wheeler, J. R.; Walters, R. W.; Agrawal, A.; Barsic, A.; Parker, R. ATPase-Modulated Stress Granules Contain a Diverse Proteome and Substructure. *Cell* **2016**, *164* (3), 487-498. DOI: 10.1016/j.cell.2015.12.038 From NLM.
(46) Beckham, C. J.; Light, H. R.; Nissan, T. A.; Ahlquist, P.; Parker, R.; Noueiry, A. Interactions between brome mosaic virus RNAs and cytoplasmic processing bodies. *J Virol* **2007**, *81* (18), 9759-9768. DOI: 10.1128/jvi.00844-07 From NLM.
(47) Reineke, L. C.; Lloyd, R. E. Diversion of stress granules and P-bodies during viral infection. *Virology* **2013**, *436* (2), 255-267. DOI: 10.1016/j.virol.2012.11.017 From NLM.
(48) Zheng, D.; Ezzeddine, N.; Chen, C. Y.; Zhu, W.; He, X.; Shyu, A. B. Deadenylation is prerequisite for P-body formation and mRNA decay in mammalian cells. *J Cell Biol* **2008**, *182* (1), 89-101. DOI: 10.1083/jcb.200801196 From NLM.

(49) Dougherty, J. D.; White, J. P.; Lloyd, R. E. Poliovirus-mediated disruption of cytoplasmic processing bodies. *J Virol* **2011**, *85* (1), 64-75. DOI: 10.1128/jvi.01657-10 From NLM.
(50) Khong, A.; Jan, E. Modulation of stress granules and P bodies during dicistrovirus infection. *J Virol* **2011**, *85* (4), 1439-1451. DOI: 10.1128/jvi.02220-10 From NLM.
(51) Roth, H.; Magg, V.; Uch, F.; Mutz, P.; Klein, P.; Haneke, K.; Lohmann, V.; Bartenschlager, R.; Fackler, O. T.; Locker, N.; et al. Flavivirus Infection Uncouples Translation Suppression from Cellular Stress Responses. *mBio* **2017**, *8* (1). DOI: 10.1128/mBio.02150-16 From NLM.
(52) Garaigorta, U.; Heim, M. H.; Boyd, B.; Wieland, S.; Chisari, F. V. Hepatitis C virus (HCV) induces formation of stress granules whose proteins regulate HCV RNA replication and virus assembly and egress. *J Virol* **2012**, *86* (20), 11043-11056. DOI: 10.1128/jvi.07101-11 From NLM.
(53) Charman, M.; Weitzman, M. D. Replication Compartments of DNA Viruses in the Nucleus: Location, Location, Location. *Viruses* **2020**, *12* (2). DOI: 10.3390/v12020151 From NLM.
(54) Sagan, S. M.; Weber, S. C. Let's phase it: viruses are master architects of biomolecular condensates. *Trends Biochem Sci* **2023**, *48* (3), 229-243. DOI: 10.1016/j.tibs.2022.09.008 From NLM.
(55) Li, H.; Ernst, C.; Kolonko-Adamska, M.; Greb-Markiewicz, B.; Man, J.; Parissi, V.; Ng, B. W. Phase separation in viral infections. *Trends Microbiol* **2022**, *30* (12), 1217-1231. DOI: 10.1016/j.tim.2022.06.005 From NLM.
(56) Zhang, X.; Zheng, R.; Li, Z.; Ma, J. Liquid-liquid Phase Separation in Viral Function. *Journal of Molecular Biology* **2023**, *435* (16), 167955. DOI: https://doi.org/10.1016/j.jmb.2023.167955.
(57) Nikolic, J.; Le Bars, R.; Lama, Z.; Scrima, N.; Lagaudrière-Gesbert, C.; Gaudin, Y.; Blondel, D. Negri bodies are viral factories with properties of liquid organelles. *Nat Commun* **2017**, *8* (1), 58. DOI: 10.1038/s41467-017-00102-9 From NLM.
(58) Dolnik, O.; Gerresheim, G. K.; Biedenkopf, N. New Perspectives on the Biogenesis of Viral Inclusion Bodies in Negative-Sense RNA Virus Infections. In *Cells*, 2021; Vol. 10.
(59) Alenquer, M.; Vale-Costa, S.; Etibor, T. A.; Ferreira, F.; Sousa, A. L.; Amorim, M. J. Influenza A virus ribonucleoproteins form liquid organelles at endoplasmic reticulum exit sites. *Nature Communications* **2019**, *10* (1), 1629. DOI: 10.1038/s41467-019-09549-4.
(60) den Boon, J. A.; Diaz, A.; Ahlquist, P. Cytoplasmic viral replication complexes. *Cell Host Microbe* **2010**, *8* (1), 77-85. DOI: 10.1016/j.chom.2010.06.010 From NLM.
(61) Savastano, A.; Ibáñez de Opakua, A.; Rankovic, M.; Zweckstetter, M. Nucleocapsid protein of SARS-CoV-2 phase separates into RNA-rich polymerase-containing condensates. *Nature communications* **2020**, *11* (1), 6041. DOI: 10.1038/s41467-020-19843-1.
(62) Nabeel-Shah, S.; Lee, H.; Ahmed, N.; Burke, G. L.; Farhangmehr, S.; Ashraf, K.; Pu, S.; Braunschweig, U.; Zhong, G.; Wei, H.; et al. SARS-CoV-2 nucleocapsid protein binds host mRNAs and attenuates stress granules to impair host stress response. *iScience* **2022**, *25* (1), 103562. DOI: https://doi.org/10.1016/j.isci.2021.103562.
(63) Liu, Q.; Liu, W.; Niu, Y.; Wang, T.; Dong, J. Liquid–liquid phase separation in plants: Advances and perspectives from model species to crops. *Plant Communications* **2024**, *5* (1), 100663. DOI: https://doi.org/10.1016/j.xplc.2023.100663.
(64) Garcia-Blanco, M. A.; Ooi, E. E.; Sessions, O. M. RNA Viruses, Pandemics and Anticipatory Preparedness. *Viruses* **2022**, *14* (10). DOI: 10.3390/v14102176 From NLM.
(65) Brown, S. L.; Garrison, D. J.; May, J. P. Phase separation of a plant virus movement protein and cellular factors support virus-host interactions. *PLoS Pathog* **2021**, *17* (9), e1009622. DOI: 10.1371/journal.ppat.1009622 From NLM.

(66) Inoue, T.; Tsai, B. How viruses use the endoplasmic reticulum for entry, replication, and assembly. *Cold Spring Harb Perspect Biol* **2013**, *5* (1), a013250-a013250. DOI: 10.1101/cshperspect.a013250 PubMed.
(67) Anand, S. K.; Tikoo, S. K. Viruses as modulators of mitochondrial functions. *Adv Virol* **2013**, *2013*, 738794-738794. DOI: 10.1155/2013/738794 PubMed.
(68) Walker, E. J.; Ghildyal, R. Editorial: Viral Interactions with the Nucleus. *Front Microbiol* **2017**, *8*, 951-951. DOI: 10.3389/fmicb.2017.00951 PubMed.
(69) Miller, S.; Krijnse-Locker, J. Modification of intracellular membrane structures for virus replication. *Nature Reviews Microbiology* **2008**, *6* (5), 363-374. DOI: 10.1038/nrmicro1890.
(70) Dolgin, E. What lava lamps and vinaigrette can teach us about cell biology. *Nature* **2018**, *555* (7696), 300-302. DOI: 10.1038/d41586-018-03070-2 PubMed.
(71) Tang, L. Liquid phase separation. *Nature Methods* **2019**, *16* (1), 18-18. DOI: 10.1038/s41592-018-0269-7.
(72) Drino, A.; Schaefer, M. R. RNAs, Phase Separation, and Membrane-Less Organelles: Are Post-Transcriptional Modifications Modulating Organelle Dynamics? *BioEssays* **2018**, *40* (12), 1800085. DOI: 10.1002/bies.201800085 (acccessed 2020/03/09).
(73) Zhang, H.; Elbaum-Garfinkle, S.; Langdon, E. M.; Taylor, N.; Occhipinti, P.; Bridges, A. A.; Brangwynne, C. P.; Gladfelter, A. S. RNA Controls PolyQ Protein Phase Transitions. *Mol Cell* **2015**, *60* (2), 220-230. DOI: 10.1016/j.molcel.2015.09.017 PubMed.
(74) Vernon, R. M.; Chong, P. A.; Tsang, B.; Kim, T. H.; Bah, A.; Farber, P.; Lin, H.; Forman-Kay, J. D. Pi-Pi contacts are an overlooked protein feature relevant to phase separation. *Elife* **2018**, *7*, e31486. DOI: 10.7554/eLife.31486 PubMed.
(75) Murthy, A. C.; Dignon, G. L.; Kan, Y.; Zerze, G. H.; Parekh, S. H.; Mittal, J.; Fawzi, N. L. Molecular interactions underlying liquid-liquid phase separation of the FUS low-complexity domain. *Nature structural & molecular biology* **2019**, *26* (7), 637-648. DOI: 10.1038/s41594-019-0250-x From NLM.
(76) Boeynaems, S.; Alberti, S.; Fawzi, N. L.; Mittag, T.; Polymenidou, M.; Rousseau, F.; Schymkowitz, J.; Shorter, J.; Wolozin, B.; Van Den Bosch, L.; et al. Protein Phase Separation: A New Phase in Cell Biology. *Trends in cell biology* **2018**, *28* (6), 420-435. DOI: 10.1016/j.tcb.2018.02.004 From NLM.
(77) Shorter, J. Phase separation of RNA-binding proteins in physiology and disease: An introduction to the JBC Reviews thematic series. *The Journal of biological chemistry* **2019**, *294* (18), 7113-7114. DOI: 10.1074/jbc.REV119.007944 From NLM.
(78) Riback, J. A.; Katanski, C. D.; Kear-Scott, J. L.; Pilipenko, E. V.; Rojek, A. E.; Sosnick, T. R.; Drummond, D. A. Stress-Triggered Phase Separation Is an Adaptive, Evolutionarily Tuned Response. *Cell* **2017**, *168* (6), 1028-1040.e1019. DOI: 10.1016/j.cell.2017.02.027 PubMed.
(79) Matsuki, H.; Takahashi, M.; Higuchi, M.; Makokha, G. N.; Oie, M.; Fujii, M. Both G3BP1 and G3BP2 contribute to stress granule formation. *Genes to cells : devoted to molecular & cellular mechanisms* **2013**, *18* (2), 135-146. DOI: 10.1111/gtc.12023 From NLM.
(80) Jain, S.; Wheeler, J. R.; Walters, R. W.; Agrawal, A.; Barsic, A.; Parker, R. ATPase-Modulated Stress Granules Contain a Diverse Proteome and Substructure. *Cell* **2016**, *164* (3), 487-498. DOI: 10.1016/j.cell.2015.12.038 PubMed.
(81) Wheeler, J. R.; Matheny, T.; Jain, S.; Abrisch, R.; Parker, R. Distinct stages in stress granule assembly and disassembly. *Elife* **2016**, *5*, e18413. DOI: 10.7554/eLife.18413.
(82) Cristea, I. M.; Rozjabek, H.; Molloy, K. R.; Karki, S.; White, L. L.; Rice, C. M.; Rout, M. P.; Chait, B. T.; MacDonald, M. R. Host factors associated with the Sindbis virus RNA-dependent

RNA polymerase: role for G3BP1 and G3BP2 in virus replication. *Journal of virology* **2010**, *84* (13), 6720-6732. DOI: 10.1128/jvi.01983-09 From NLM.
(83) Götte, B.; Panas, M. D.; Hellström, K.; Liu, L.; Samreen, B.; Larsson, O.; Ahola, T.; McInerney, G. M. Separate domains of G3BP promote efficient clustering of alphavirus replication complexes and recruitment of the translation initiation machinery. *PLoS Pathog* **2019**, *15* (6), e1007842. DOI: 10.1371/journal.ppat.1007842 From NLM.
(84) Hosmillo, M.; Lu, J.; McAllaster, M. R.; Eaglesham, J. B.; Wang, X.; Emmott, E.; Domingues, P.; Chaudhry, Y.; Fitzmaurice, T. J.; Tung, M. K.; et al. Noroviruses subvert the core stress granule component G3BP1 to promote viral VPg-dependent translation. *Elife* **2019**, *8*. DOI: 10.7554/eLife.46681 From NLM.
(85) Yang, W.; Ru, Y.; Ren, J.; Bai, J.; Wei, J.; Fu, S.; Liu, X.; Li, D.; Zheng, H. G3BP1 inhibits RNA virus replication by positively regulating RIG-I-mediated cellular antiviral response. *Cell death & disease* **2019**, *10* (12), 946. DOI: 10.1038/s41419-019-2178-9 From NLM.
(86) Pandey, K.; Zhong, S.; Diel, D. G.; Hou, Y.; Wang, Q.; Nelson, E.; Wang, X. GTPase-activating protein-binding protein 1 (G3BP1) plays an antiviral role against porcine epidemic diarrhea virus. *Veterinary microbiology* **2019**, *236*, 108392. DOI: 10.1016/j.vetmic.2019.108392 From NLM.
(87) Reineke, L. C.; Kedersha, N.; Langereis, M. A.; van Kuppeveld, F. J.; Lloyd, R. E. Stress granules regulate double-stranded RNA-dependent protein kinase activation through a complex containing G3BP1 and Caprin1. *mBio* **2015**, *6* (2), e02486. DOI: 10.1128/mBio.02486-14 From NLM.
(88) Heinrich, B. S.; Maliga, Z.; Stein, D. A.; Hyman, A. A.; Whelan, S. P. J. Phase Transitions Drive the Formation of Vesicular Stomatitis Virus Replication Compartments. *mBio* **2018**, *9* (5). DOI: 10.1128/mBio.02290-17 From NLM.
(89) Zhou, Y.; Su, J. M.; Samuel, C. E.; Ma, D. Measles Virus Forms Inclusion Bodies with Properties of Liquid Organelles. *Journal of virology* **2019**, *93* (21). DOI: 10.1128/jvi.00948-19 From NLM.
(90) Nevers, Q.; Albertini, A. A.; Lagaudrière-Gesbert, C.; Gaudin, Y. Negri bodies and other virus membrane-less replication compartments. *Biochim Biophys Acta Mol Cell Res* **2020**, *1867* (12), 118831-118831. DOI: 10.1016/j.bbamcr.2020.118831 PubMed.
(91) Lahaye, X.; Vidy, A.; Pomier, C.; Obiang, L.; Harper, F.; Gaudin, Y.; Blondel, D. Functional characterization of Negri bodies (NBs) in rabies virus-infected cells: Evidence that NBs are sites of viral transcription and replication. *Journal of virology* **2009**, *83* (16), 7948-7958. DOI: 10.1128/JVI.00554-09 PubMed.
(92) Belov, G. A.; van Kuppeveld, F. J. (+)RNA viruses rewire cellular pathways to build replication organelles. *Curr Opin Virol* **2012**, *2* (6), 740-747. DOI: 10.1016/j.coviro.2012.09.006 From NLM.
(93) Nagy, P. D.; Strating, J. R.; van Kuppeveld, F. J. Building Viral Replication Organelles: Close Encounters of the Membrane Types. *PLoS Pathog* **2016**, *12* (10), e1005912. DOI: 10.1371/journal.ppat.1005912 From NLM.
(94) Cascarina, S. M.; Ross, E. D. A proposed role for the SARS-CoV-2 nucleocapsid protein in the formation and regulation of biomolecular condensates. *FASEB journal : official publication of the Federation of American Societies for Experimental Biology* **2020**. DOI: 10.1096/fj.202001351 From NLM.
(95) Iserman, C.; Roden, C. A.; Boerneke, M. A.; Sealfon, R. S. G.; McLaughlin, G. A.; Jungreis, I.; Fritch, E. J.; Hou, Y. J.; Ekena, J.; Weidmann, C. A.; et al. Genomic RNA Elements Drive Phase

Separation of the SARS-CoV-2 Nucleocapsid. *Mol Cell* **2020**, *80* (6), 1078-1091.e1076. DOI: 10.1016/j.molcel.2020.11.041 From NLM.
(96) Perdikari, T. M.; Murthy, A. C.; Ryan, V. H.; Watters, S.; Naik, M. T.; Fawzi, N. L. SARS-CoV-2 nucleocapsid protein phase-separates with RNA and with human hnRNPs. *EMBO J* **2020**, *39* (24), e106478, https://doi.org/10.15252/embj.2020106478. DOI: https://doi.org/10.15252/embj.2020106478 (acccessed 2020/12/15).
(97) Li, J.; Guo, M.; Tian, X.; Wang, X.; Yang, X.; Wu, P.; Liu, C.; Xiao, Z.; Qu, Y.; Yin, Y.; et al. Virus-Host Interactome and Proteomic Survey Reveal Potential Virulence Factors Influencing SARS-CoV-2 Pathogenesis. *Med* **2020**. DOI: https://doi.org/10.1016/j.medj.2020.07.002.
(98) Nabeel-Shah, S.; Lee, H.; Ahmed, N.; Marcon, E.; Farhangmehr, S.; Pu, S.; Burke, G. L.; Ashraf, K.; Wei, H.; Zhong, G.; et al. SARS-CoV-2 Nucleocapsid protein attenuates stress granule formation and alters gene expression via direct interaction with host mRNAs. *bioRxiv : the preprint server for biology* **2020**, 2020.2010.2023.342113. DOI: 10.1101/2020.10.23.342113.
(99) Carlson, C. R.; Asfaha, J. B.; Ghent, C. M.; Howard, C. J.; Hartooni, N.; Safari, M.; Frankel, A. D.; Morgan, D. O. Phosphoregulation of Phase Separation by the SARS-CoV-2 N Protein Suggests a Biophysical Basis for its Dual Functions. *Mol Cell* **2020**, *80* (6), 1092-1103.e1094. DOI: 10.1016/j.molcel.2020.11.025 From NLM.
(100) Alers-Velazquez, R.; Jacques, S.; Muller, C.; Boldt, J.; Schoelz, J.; Leisner, S. Cauliflower mosaic virus P6 inclusion body formation: A dynamic and intricate process. *Virology* **2021**, *553*, 9-22. DOI: https://doi.org/10.1016/j.virol.2020.10.003.
(101) Li, Q.; Liu, N.; Liu, Q.; Zheng, X.; Lu, L.; Gao, W.; Liu, Y.; Liu, Y.; Zhang, S.; Wang, Q.; et al. DEAD-box helicases modulate dicing body formation in Arabidopsis. *Sci Adv* **2021**, *7* (18). DOI: 10.1126/sciadv.abc6266 From NLM.
(102) Yang, Z.; Li, Y. Dissection of RNAi-based antiviral immunity in plants. *Current opinion in virology* **2018**, *32*, 88-99. DOI: 10.1016/j.coviro.2018.08.003 From NLM.
(103) Ryabov, E. V.; Robinson, D. J.; Taliansky, M. Umbravirus-encoded proteins both stabilize heterologous viral RNA and mediate its systemic movement in some plant species. *Virology* **2001**, *288* (2), 391-400. DOI: 10.1006/viro.2001.1078 From NLM.
(104) Ryabov, E. V.; Oparka, K. J.; Santa Cruz, S.; Robinson, D. J.; Taliansky, M. E. Intracellular location of two groundnut rosette umbravirus proteins delivered by PVX and TMV vectors. *Virology* **1998**, *242* (2), 303-313. DOI: 10.1006/viro.1997.9025 From NLM.
(105) Taliansky, M.; Roberts, I. M.; Kalinina, N.; Ryabov, E. V.; Raj, S. K.; Robinson, D. J.; Oparka, K. J. An umbraviral protein, involved in long-distance RNA movement, binds viral RNA and forms unique, protective ribonucleoprotein complexes. *Journal of virology* **2003**, *77* (5), 3031-3040. DOI: 10.1128/jvi.77.5.3031-3040.2003 PubMed.
(106) May, J. P.; Johnson, P. Z.; Ilyas, M.; Gao, F.; Simon, A. E. The Multifunctional Long-Distance Movement Protein of Pea Enation Mosaic Virus 2 Protects Viral and Host Transcripts from Nonsense-Mediated Decay. *mBio* **2020**, *11* (2), e00204-00220. DOI: 10.1128/mBio.00204-20.
(107) Canetta, E.; Kim, S. H.; Kalinina, N. O.; Shaw, J.; Adya, A. K.; Gillespie, T.; Brown, J. W. S.; Taliansky, M. A plant virus movement protein forms ringlike complexes with the major nucleolar protein, fibrillarin, in vitro. *J Mol Biol* **2008**, *376* (4), 932-937. DOI: 10.1016/j.jmb.2007.12.039 PubMed.
(108) Kim, S. H.; MacFarlane, S.; Kalinina, N. O.; Rakitina, D. V.; Ryabov, E. V.; Gillespie, T.; Haupt, S.; Brown, J. W. S.; Taliansky, M. Interaction of a plant virus-encoded protein with the

major nucleolar protein fibrillarin is required for systemic virus infection. *Proceedings of the National Academy of Sciences* **2007**, *104* (26), 11115. DOI: 10.1073/pnas.0704632104.
(109) Kalinina, N. O.; Makarova, S.; Makhotenko, A.; Love, A. J.; Taliansky, M. The Multiple Functions of the Nucleolus in Plant Development, Disease and Stress Responses. *Frontiers in plant science* **2018**, *9* (132), Review. DOI: 10.3389/fpls.2018.00132.
(110) Haupt, S.; Stroganova, T.; Ryabov, E.; Kim, S. H.; Fraser, G.; Duncan, G.; Mayo, M. A.; Barker, H.; Taliansky, M. Nucleolar localization of potato leafroll virus capsid proteins. *J Gen Virol* **2005**, *86* (Pt 10), 2891-2896. DOI: 10.1099/vir.0.81101-0 From NLM.
(111) Chang, C.-H.; Hsu, F.-C.; Lee, S.-C.; Lo, Y.-S.; Wang, J.-D.; Shaw, J.; Taliansky, M.; Chang, B.-Y.; Hsu, Y.-H.; Lin, N.-S. The Nucleolar Fibrillarin Protein Is Required for Helper Virus-Independent Long-Distance Trafficking of a Subviral Satellite RNA in Plants. *Plant Cell* **2016**, *28* (10), 2586-2602. DOI: 10.1105/tpc.16.00071 (acccessed 3/4/2021).
(112) Feric, M.; Vaidya, N.; Harmon, T. S.; Mitrea, D. M.; Zhu, L.; Richardson, T. M.; Kriwacki, R. W.; Pappu, R. V.; Brangwynne, C. P. Coexisting Liquid Phases Underlie Nucleolar Subcompartments. *Cell* **2016**, *165* (7), 1686-1697. DOI: 10.1016/j.cell.2016.04.047 From NLM.
(113) Mérai, Z.; Kerényi, Z.; Molnár, A.; Barta, E.; Válóczi, A.; Bisztray, G.; Havelda, Z.; Burgyán, J.; Silhavy, D. Aureusvirus P14 is an efficient RNA silencing suppressor that binds double-stranded RNAs without size specificity. *Journal of virology* **2005**, *79* (11), 7217-7226. DOI: 10.1128/jvi.79.11.7217-7226.2005 From NLM.
(114) Ishikawa-Ankerhold, H., Ankerhold, R. and Drummen, G. . Fluorescence Recovery After Photobleaching (FRAP). In *In eLS, John Wiley & Sons, Ltd (Ed.)*. 2014.
(115) Protter, D. S. W.; Rao, B. S.; Van Treeck, B.; Lin, Y.; Mizoue, L.; Rosen, M. K.; Parker, R. Intrinsically Disordered Regions Can Contribute Promiscuous Interactions to RNP Granule Assembly. *Cell Rep* **2018**, *22* (6), 1401-1412. DOI: 10.1016/j.celrep.2018.01.036 (acccessed 2021/08/19).
(116) Dosztányi, Z. Prediction of protein disorder based on IUPred. *Protein Sci* **2018**, *27* (1), 331-340. DOI: 10.1002/pro.3334 PubMed.
(117) Bolognesi, B.; Lorenzo Gotor, N.; Dhar, R.; Cirillo, D.; Baldrighi, M.; Tartaglia, G. G.; Lehner, B. A Concentration-Dependent Liquid Phase Separation Can Cause Toxicity upon Increased Protein Expression. *Cell Rep* **2016**, *16* (1), 222-231. DOI: 10.1016/j.celrep.2016.05.076 PubMed.
(118) S., K. S. M. S. A. Hexanediol: a chemical probe to investigate the material properties of membrane-less compartments. Matters [Internet]. Sciencematters; 2017 May 22; http://dx.doi.org/10.19185/matters.201702000010.
(119) Dosztányi, Z. Prediction of protein disorder based on IUPred. *Protein Sci* **2018**, *27* (1), 331-340. DOI: 10.1002/pro.3334 From NLM.
(120) Bolognesi, B.; Lorenzo Gotor, N.; Dhar, R.; Cirillo, D.; Baldrighi, M.; Tartaglia, G. G.; Lehner, B. A Concentration-Dependent Liquid Phase Separation Can Cause Toxicity upon Increased Protein Expression. *Cell Rep* **2016**, *16* (1), 222-231. DOI: 10.1016/j.celrep.2016.05.076 From NLM.
(121) Luo, H.; Lee, N.; Wang, X.; Li, Y.; Schmelzer, A.; Hunter, A. K.; Pabst, T.; Wang, W. K. Liquid-liquid phase separation causes high turbidity and pressure during low pH elution process in Protein A chromatography. *Journal of Chromatography A* **2017**, *1488*, 57-67. DOI: https://doi.org/10.1016/j.chroma.2017.01.067.
(122) Ryabov, E. V.; Kim, S. H.; Taliansky, M. Identification of a nuclear localization signal and nuclear export signal of the umbraviral long-distance RNA movement protein. *J Gen Virol* **2004**, *85* (Pt 5), 1329-1333. DOI: 10.1099/vir.0.79854-0 From NLM.

(123) Frottin, F.; Schueder, F.; Tiwary, S.; Gupta, R.; Körner, R.; Schlichthaerle, T.; Cox, J.; Jungmann, R.; Hartl, F. U.; Hipp, M. S. The nucleolus functions as a phase-separated protein quality control compartment. *Science* **2019**, eaaw9157. DOI: 10.1126/science.aaw9157.
(124) Rakitina, D. V.; Taliansky, M.; Brown, J. W. S.; Kalinina, N. O. Two RNA-binding sites in plant fibrillarin provide interactions with various RNA substrates. *Nucleic Acids Res* **2011**, *39* (20), 8869-8880. DOI: 10.1093/nar/gkr594 (acccessed 3/22/2021).
(125) Yao, R. W.; Xu, G.; Wang, Y.; Shan, L.; Luan, P. F.; Wang, Y.; Wu, M.; Yang, L. Z.; Xing, Y. H.; Yang, L.; et al. Nascent Pre-rRNA Sorting via Phase Separation Drives the Assembly of Dense Fibrillar Components in the Human Nucleolus. *Mol Cell* **2019**, *76* (5), 767-783.e711. DOI: 10.1016/j.molcel.2019.08.014 From NLM.
(126) Berry, J.; Weber, S. C.; Vaidya, N.; Haataja, M.; Brangwynne, C. P. RNA transcription modulates phase transition-driven nuclear body assembly. *Proceedings of the National Academy of Sciences* **2015**, *112* (38), E5237. DOI: 10.1073/pnas.1509317112.
(127) Banani, S. F.; Rice, A. M.; Peeples, W. B.; Lin, Y.; Jain, S.; Parker, R.; Rosen, M. K. Compositional Control of Phase-Separated Cellular Bodies. *Cell* **2016**, *166* (3), 651-663. DOI: 10.1016/j.cell.2016.06.010 (acccessed 2021/07/09).
(128) Ditlev, J. A.; Case, L. B.; Rosen, M. K. Who's In and Who's Out—Compositional Control of Biomolecular Condensates. *Journal of Molecular Biology* **2018**, *430* (23), 4666-4684. DOI: https://doi.org/10.1016/j.jmb.2018.08.003.
(129) Stauffer, W.; Sheng, H.; Lim, H. N. EzColocalization: An ImageJ plugin for visualizing and measuring colocalization in cells and organisms. *Scientific reports* **2018**, *8* (1), 15764. DOI: 10.1038/s41598-018-33592-8 From NLM.
(130) Lindbo, J. A. TRBO: A High-Efficiency Tobacco Mosaic Virus RNA-Based Overexpression Vector. *Plant Physiology* **2007**, *145* (4), 1232. DOI: 10.1104/pp.107.106377.
(131) Ryabov, E. V.; Robinson, D. J.; Taliansky, M. E. A plant virus-encoded protein facilitates long-distance movement of heterologous viral RNA. *Proceedings of the National Academy of Sciences* **1999**, *96* (4), 1212-1217. DOI: 10.1073/pnas.96.4.1212.
(132) Krapp, S.; Greiner, E.; Amin, B.; Sonnewald, U.; Krenz, B. The stress granule component G3BP is a novel interaction partner for the nuclear shuttle proteins of the nanovirus pea necrotic yellow dwarf virus and geminivirus abutilon mosaic virus. *Virus Res* **2017**, *227*, 6-14. DOI: 10.1016/j.virusres.2016.09.021 From NLM.
(133) Tourrière, H.; Chebli, K.; Zekri, L.; Courselaud, B.; Blanchard, J. M.; Bertrand, E.; Tazi, J. The RasGAP-associated endoribonuclease G3BP assembles stress granules. *J Cell Biol* **2003**, *160* (6), 823-831. DOI: 10.1083/jcb.200212128 PubMed.
(134) Guillén-Boixet, J.; Kopach, A.; Holehouse, A. S.; Wittmann, S.; Jahnel, M.; Schlüßler, R.; Kim, K.; Trussina, I. R. E. A.; Wang, J.; Mateju, D.; et al. RNA-Induced Conformational Switching and Clustering of G3BP Drive Stress Granule Assembly by Condensation. *Cell* **2020**, *181* (2), 346-361.e317. DOI: 10.1016/j.cell.2020.03.049 PubMed.
(135) Boeynaems, S.; Bogaert, E.; Kovacs, D.; Konijnenberg, A.; Timmerman, E.; Volkov, A.; Guharoy, M.; De Decker, M.; Jaspers, T.; Ryan, V. H.; et al. Phase Separation of C9orf72 Dipeptide Repeats Perturbs Stress Granule Dynamics. *Mol Cell* **2017**, *65* (6), 1044-1055.e1045. DOI: 10.1016/j.molcel.2017.02.013 PubMed.
(136) Brangwynne, Clifford P.; Tompa, P.; Pappu, Rohit V. Polymer physics of intracellular phase transitions. *Nature Physics* **2015**, *11* (11), 899-904. DOI: 10.1038/nphys3532.

(137) Savada, R. P.; Bonham-Smith, P. C. Charge versus sequence for nuclear/nucleolar localization of plant ribosomal proteins. *Plant molecular biology* **2013**, *81* (4-5), 477-493. DOI: 10.1007/s11103-013-0017-4 From NLM.
(138) Musinova, Y. R.; Kananykhina, E. Y.; Potashnikova, D. M.; Lisitsyna, O. M.; Sheval, E. V. A charge-dependent mechanism is responsible for the dynamic accumulation of proteins inside nucleoli. *Biochimica et Biophysica Acta (BBA) - Molecular Cell Research* **2015**, *1853* (1), 101-110. DOI: https://doi.org/10.1016/j.bbamcr.2014.10.007.
(139) Reuper, H.; Amari, K.; Krenz, B. Analyzing the G3BP-like gene family of Arabidopsis thaliana in early turnip mosaic virus infection. *Scientific reports* **2021**, *11* (1), 2187. DOI: 10.1038/s41598-021-81276-7.
(140) Fischer, J. W.; Busa, V. F.; Shao, Y.; Leung, A. K. L. Structure-Mediated RNA Decay by UPF1 and G3BP1. *Mol Cell* **2020**, *78* (1), 70-84.e76. DOI: 10.1016/j.molcel.2020.01.021 From NLM.
(141) Simon, A. E.; Miller, W. A. 3' cap-independent translation enhancers of plant viruses. *Annual review of microbiology* **2013**, *67*, 21-42. DOI: 10.1146/annurev-micro-092412-155609 From NLM.
(142) May, J. P.; Yuan, X.; Sawicki, E.; Simon, A. E. RNA virus evasion of nonsense-mediated decay. *PLoS Pathog* **2018**, *14* (11), e1007459. DOI: 10.1371/journal.ppat.1007459 From NLM.
(143) May, J. P.; Simon, A. E. Targeting of viral RNAs by Upf1-mediated RNA decay pathways. *Current opinion in virology* **2020**, *47*, 1-8. DOI: 10.1016/j.coviro.2020.11.002 From NLM.
(144) Brown, J. A. L.; Roberts, T. L.; Richards, R.; Woods, R.; Birrell, G.; Lim, Y. C.; Ohno, S.; Yamashita, A.; Abraham, R. T.; Gueven, N.; et al. A novel role for hSMG-1 in stress granule formation. *Mol Cell Biol* **2011**, *31* (22), 4417-4429. DOI: 10.1128/MCB.05987-11 PubMed.
(145) Kertész, S.; Kerényi, Z.; Mérai, Z.; Bartos, I.; Pálfy, T.; Barta, E.; Silhavy, D. Both introns and long 3'-UTRs operate as cis-acting elements to trigger nonsense-mediated decay in plants. *Nucleic Acids Res* **2006**, *34* (21), 6147-6157. DOI: 10.1093/nar/gkl737 From NLM.
(146) Busch, D. J.; Houser, J. R.; Hayden, C. C.; Sherman, M. B.; Lafer, E. M.; Stachowiak, J. C. Intrinsically disordered proteins drive membrane curvature. *Nature communications* **2015**, *6*, 7875. DOI: 10.1038/ncomms8875 From NLM.
(147) DeGroot, A. C. M.; Busch, D. J.; Hayden, C. C.; Mihelic, S. A.; Alpar, A. T.; Behar, M.; Stachowiak, J. C. Entropic Control of Receptor Recycling Using Engineered Ligands. *Biophysical journal* **2018**, *114* (6), 1377-1388. DOI: 10.1016/j.bpj.2018.01.036 From NLM.
(148) Boeynaems, S.; De Decker, M.; Tompa, P.; Van Den Bosch, L. Arginine-rich Peptides Can Actively Mediate Liquid-liquid Phase Separation. *Bio-protocol* **2017**, *7* (17), e2525. DOI: 10.21769/BioProtoc.2525.
(149) Oh, J. W.; Kong, Q.; Song, C.; Carpenter, C. D.; Simon, A. E. Open reading frames of turnip crinkle virus involved in satellite symptom expression and incompatibility with Arabidopsis thaliana ecotype Dijon. *Mol Plant Microbe Interact* **1995**, *8* (6), 979-987. DOI: 10.1094/mpmi-8-0979 From NLM.
(150) Grentzmann, G.; Ingram, J. A.; Kelly, P. J.; Gesteland, R. F.; Atkins, J. F. A dual-luciferase reporter system for studying recoding signals. *RNA* **1998**, *4* (4), 479-486. PubMed.
(151) Schneider, C. A.; Rasband, W. S.; Eliceiri, K. W. NIH Image to ImageJ: 25 years of image analysis. *Nature methods* **2012**, *9* (7), 671-675. DOI: 10.1038/nmeth.2089.
(152) Untergasser, A.; Cutcutache, I.; Koressaar, T.; Ye, J.; Faircloth, B. C.; Remm, M.; Rozen, S. G. Primer3--new capabilities and interfaces. *Nucleic Acids Res* **2012**, *40* (15), e115. DOI: 10.1093/nar/gks596 From NLM.

(153) Liu, Y.; Zhang, Y.; Wang, M.; Cheng, A.; Yang, Q.; Wu, Y.; Jia, R.; Liu, M.; Zhu, D.; Chen, S.; et al. Structures and Functions of the 3' Untranslated Regions of Positive-Sense Single-Stranded RNA Viruses Infecting Humans and Animals. *Front Cell Infect Microbiol* **2020**, *10*, 453. DOI: 10.3389/fcimb.2020.00453 From NLM.
(154) Taliansky, M.; Roberts, I. M.; Kalinina, N.; Ryabov, E. V.; Raj, S. K.; Robinson, D. J.; Oparka, K. J. An umbraviral protein, involved in long-distance RNA movement, binds viral RNA and forms unique, protective ribonucleoprotein complexes. *J Virol* **2003**, *77* (5), 3031-3040. DOI: 10.1128/jvi.77.5.3031-3040.2003 From NLM.
(155) Tchurikov, N. A.; Kravatsky, Y. V. The Role of rDNA Clusters in Global Epigenetic Gene Regulation. *Front Genet* **2021**, *12*, 730633. DOI: 10.3389/fgene.2021.730633 From NLM.
(156) Shrinivas, K.; Sabari, B. R.; Coffey, E. L.; Klein, I. A.; Boija, A.; Zamudio, A. V.; Schuijers, J.; Hannett, N. M.; Sharp, P. A.; Young, R. A.; et al. Enhancer Features that Drive Formation of Transcriptional Condensates. *Mol Cell* **2019**, *75* (3), 549-561.e547. DOI: 10.1016/j.molcel.2019.07.009 From NLM.
(157) Kang, J.-Y.; Wen, Z.; Pan, D.; Zhang, Y.; Li, Q.; Zhong, A.; Yu, X.; Wu, Y.-C.; Chen, Y.; Zhang, X.; et al. LLPS of FXR1 drives spermiogenesis by activating translation of stored mRNAs. *Science 377* (6607), eabj6647. DOI: 10.1126/science.abj6647 (acccessed 2024/02/02).
(158) Etibor, T. A.; Yamauchi, Y.; Amorim, M. J. Liquid Biomolecular Condensates and Viral Lifecycles: Review and Perspectives. *Viruses* **2021**, *13* (3). DOI: 10.3390/v13030366 From NLM.
(159) Brocca, S.; Grandori, R.; Longhi, S.; Uversky, V. Liquid-Liquid Phase Separation by Intrinsically Disordered Protein Regions of Viruses: Roles in Viral Life Cycle and Control of Virus-Host Interactions. *International journal of molecular sciences* **2020**, *21* (23). DOI: 10.3390/ijms21239045 From NLM.
(160) Su, J. M.; Wilson, M. Z.; Samuel, C. E.; Ma, D. Formation and Function of Liquid-Like Viral Factories in Negative-Sense Single-Stranded RNA Virus Infections. *Viruses* **2021**, *13* (1). DOI: 10.3390/v13010126 From NLM.
(161) May, J. P. Plant viruses and biomolecular condensates: novel perspectives in virus replication strategies. *New Phytol* **2024**. DOI: 10.1111/nph.19778 From NLM.
(162) Lin, W.; Nagy, P. D. Co-opted cytosolic proteins form condensate substructures within membranous replication organelles of a positive-strand RNA virus. *New Phytol* **2024**, *243* (5), 1917-1935. DOI: 10.1111/nph.19691 From NLM.
(163) Dreher, T. W.; Miller, W. A. Translational control in positive strand RNA plant viruses. *Virology* **2006**, *344* (1), 185-197. DOI: https://doi.org/10.1016/j.virol.2005.09.031.
(164) Sanfaçon, H. Plant Translation Factors and Virus Resistance. *Viruses* **2015**, *7* (7), 3392-3419. DOI: 10.3390/v7072778 From NLM.
(165) Wang, H.; Shi, D.; Jiang, P.; Yu, Z.; Han, Y.; Zhang, Z.; Wang, P.; Huang, H.; Yao, H.; Qian, P. SARS-CoV-2 N protein potentiates host NPM1-snoRNA translation machinery to enhance viral replication. *Signal Transduction and Targeted Therapy* **2022**, *7* (1), 356. DOI: 10.1038/s41392-022-01210-9.
(166) Monette, A.; Niu, M.; Chen, L.; Rao, S.; Gorelick, R. J.; Mouland, A. J. Pan-retroviral Nucleocapsid-Mediated Phase Separation Regulates Genomic RNA Positioning and Trafficking. *Cell Rep* **2020**, *31* (3), 107520. DOI: 10.1016/j.celrep.2020.03.084 From NLM.
(167) Hafrén, A.; Lõhmus, A.; Mäkinen, K. Formation of Potato Virus A-Induced RNA Granules and Viral Translation Are Interrelated Processes Required for Optimal Virus Accumulation. *PLoS Pathog* **2015**, *11* (12), e1005314. DOI: 10.1371/journal.ppat.1005314 From NLM.

(168) Zhu, J.; Gopinath, K.; Murali, A.; Yi, G.; Hayward, S. D.; Zhu, H.; Kao, C. RNA-binding proteins that inhibit RNA virus infection. *Proc Natl Acad Sci U S A* **2007**, *104* (9), 3129-3134. DOI: 10.1073/pnas.0611617104 From NLM.
(169) Zhao, R. Y. Yeast for virus research. *Microb Cell* **2017**, *4* (10), 311-330. DOI: 10.15698/mic2017.10.592 From NLM.
(170) Nagy, P. D. Exploitation of a surrogate host, Saccharomyces cerevisiae, to identify cellular targets and develop novel antiviral approaches. *Current opinion in virology* **2017**, *26*, 132-140. DOI: 10.1016/j.coviro.2017.07.031 From NLM.
(171) Pogany, J.; Nagy, P. D. Activation of Tomato Bushy Stunt Virus RNA-Dependent RNA Polymerase by Cellular Heat Shock Protein 70 Is Enhanced by Phospholipids In Vitro. *Journal of virology* **2015**, *89* (10), 5714-5723. DOI: 10.1128/jvi.03711-14 From NLM.
(172) Serva, S.; Nagy, P. D. Proteomics analysis of the tombusvirus replicase: Hsp70 molecular chaperone is associated with the replicase and enhances viral RNA replication. *Journal of virology* **2006**, *80* (5), 2162-2169. DOI: 10.1128/jvi.80.5.2162-2169.2006 From NLM.
(173) Wheeler, J. R.; Jain, S.; Khong, A.; Parker, R. Isolation of yeast and mammalian stress granule cores. *Methods (San Diego, Calif.)* **2017**, *126*, 12-17. DOI: 10.1016/j.ymeth.2017.04.020 From NLM.
(174) Brown, S. L.; May, J. P. Viral condensates formed by Pea enation mosaic virus 2 sequester ribosomal components and suppress translation. *Virology* **2025**, *601*, 110301. DOI: https://doi.org/10.1016/j.virol.2024.110301.
(175) Mazzoni-Putman, S. M.; Stepanova, A. N. A Plant Biologist's Toolbox to Study Translation. *Front Plant Sci* **2018**, *9*, 873. DOI: 10.3389/fpls.2018.00873 From NLM.
(176) Lecampion, C.; Floris, M.; Fantino, J. R.; Robaglia, C.; Laloi, C. An Easy Method for Plant Polysome Profiling. *J Vis Exp* **2016**, (114). DOI: 10.3791/54231 From NLM.
(177) Decle-Carrasco, S.; Rodríguez-Piña, A. L.; Rodríguez-Zapata, L. C.; Castano, E. Current research on viral proteins that interact with fibrillarin. *Mol Biol Rep* **2023**, *50* (5), 4631-4643. DOI: 10.1007/s11033-023-08343-2 From NLM.
(178) Jaafar, M.; Paraqindes, H.; Gabut, M.; Diaz, J. J.; Marcel, V.; Durand, S. 2'O-Ribose Methylation of Ribosomal RNAs: Natural Diversity in Living Organisms, Biological Processes, and Diseases. *Cells* **2021**, *10* (8). DOI: 10.3390/cells10081948 From NLM.
(179) Khoshnevis, S.; Dreggors-Walker, R. E.; Marchand, V.; Motorin, Y.; Ghalei, H. Ribosomal RNA 2'-O-methylations regulate translation by impacting ribosome dynamics. *Proc Natl Acad Sci U S A* **2022**, *119* (12), e2117334119. DOI: 10.1073/pnas.2117334119 From NLM.
(180) Chawla, M.; Oliva, R.; Bujnicki, J. M.; Cavallo, L. An atlas of RNA base pairs involving modified nucleobases with optimal geometries and accurate energies. *Nucleic Acids Res* **2015**, *43* (14), 6714-6729. DOI: 10.1093/nar/gkv606 From NLM.
(181) Erales, J.; Marchand, V.; Panthu, B.; Gillot, S.; Belin, S.; Ghayad, S. E.; Garcia, M.; Laforêts, F.; Marcel, V.; Baudin-Baillieu, A.; et al. Evidence for rRNA 2'-O-methylation plasticity: Control of intrinsic translational capabilities of human ribosomes. *Proc Natl Acad Sci U S A* **2017**, *114* (49), 12934-12939. DOI: 10.1073/pnas.1707674114 From NLM.
(182) Birkedal, U.; Christensen-Dalsgaard, M.; Krogh, N.; Sabarinathan, R.; Gorodkin, J.; Nielsen, H. Profiling of ribose methylations in RNA by high-throughput sequencing. *Angew Chem Int Ed Engl* **2015**, *54* (2), 451-455. DOI: 10.1002/anie.201408362 From NLM.
(183) Marchand, V.; Blanloeil-Oillo, F.; Helm, M.; Motorin, Y. Illumina-based RiboMethSeq approach for mapping of 2'-O-Me residues in RNA. *Nucleic Acids Research* **2016**, *44* (16), e135-e135. DOI: 10.1093/nar/gkw547 (acccessed 4/27/2023).

(184) Motorin, Y.; Marchand, V. Detection and Analysis of RNA Ribose 2'-O-Methylations: Challenges and Solutions. *Genes (Basel)* **2018**, *9* (12). DOI: 10.3390/genes9120642 From NLM.
(185) Marchand, V.; Blanloeil-Oillo, F.; Helm, M.; Motorin, Y. Illumina-based RiboMethSeq approach for mapping of 2'-O-Me residues in RNA. *Nucleic Acids Res* **2016**, *44* (16), e135. DOI: 10.1093/nar/gkw547 From NLM.
(186) Azevedo-Favory, J.; Gaspin, C.; Ayadi, L.; Montacié, C.; Marchand, V.; Jobet, E.; Rompais, M.; Carapito, C.; Motorin, Y.; Sáez-Vásquez, J. Mapping rRNA 2'-O-methylations and identification of C/D snoRNAs in Arabidopsis thaliana plants. *RNA Biol* **2021**, *18* (11), 1760-1777. DOI: 10.1080/15476286.2020.1869892 From NLM.
(187) Glauninger, H.; Bard, J. A. M.; Wong Hickernell, C. J.; Airoldi, E. M.; Li, W.; Singer, R. H.; Paul, S.; Fei, J.; Sosnick, T. R.; Wallace, E. W. J.; et al. Transcriptome-wide mRNA condensation precedes stress granule formation and excludes stress-induced transcripts. *bioRxiv : the preprint server for biology* **2024**, 2024.2004.2015.589678. DOI: 10.1101/2024.04.15.589678.
(188) Gao, F.; Kasprzak, W. K.; Szarko, C.; Shapiro, B. A.; Simon, A. E. The 3' untranslated region of Pea Enation Mosaic Virus contains two T-shaped, ribosome-binding, cap-independent translation enhancers. *Journal of virology* **2014**, *88* (20), 11696-11712. DOI: 10.1128/jvi.01433-14 From NLM.
(189) Lewicka, A.; Roman, C.; Jones, S.; Disare, M.; Rice, Phoebe A.; Piccirilli, Joseph A. Crystal structure of a cap-independent translation enhancer RNA. *Nucleic Acids Res* **2023**, *51* (16), 8891-8907. DOI: 10.1093/nar/gkad649 (acccessed 9/16/2024).
(190) Lee, S.; Kim, J.; Kim, M. S.; Min, C. W.; Kim, S. T.; Choi, S. B.; Lee, J. H.; Choi, D. The Phytophthora nucleolar effector Pi23226 targets host ribosome biogenesis to induce necrotrophic cell death. *Plant Commun* **2023**, *4* (5), 100606. DOI: 10.1016/j.xplc.2023.100606 From NLM.
(191) Kirstein-Miles, J.; Scior, A.; Deuerling, E.; Morimoto, R. I. The nascent polypeptide-associated complex is a key regulator of proteostasis. *EMBO J* **2013**, *32* (10), 1451-1468-1468. DOI: https://doi.org/10.1038/emboj.2013.87 (acccessed 2024/09/12).
(192) May, J. P.; Simon, A. E. Targeting of viral RNAs by Upf1-mediated RNA decay pathways. *Current opinion in virology* **2021**, *47*, 1-8. DOI: https://doi.org/10.1016/j.coviro.2020.11.002.
(193) Chkuaseli, T.; White, K. A. Dimerization of an umbravirus RNA genome activates subgenomic mRNA transcription. *Nucleic Acids Res* **2023**, *51* (16), 8787-8804. DOI: 10.1093/nar/gkad550 From NLM.
(194) Galloux, M.; Longhi, S. Unraveling Liquid-Liquid Phase Separation (LLPS) in Viral Infections to Understand and Treat Viral Diseases. *International journal of molecular sciences* **2024**, *25* (13). DOI: 10.3390/ijms25136981 From NLM.
(195) Nakagawa, T.; Suzuki, T.; Murata, S.; Nakamura, S.; Hino, T.; Maeo, K.; Tabata, R.; Kawai, T.; Tanaka, K.; Niwa, Y.; et al. Improved Gateway binary vectors: high-performance vectors for creation of fusion constructs in transgenic analysis of plants. *Biosci Biotechnol Biochem* **2007**, *71* (8), 2095-2100. DOI: 10.1271/bbb.70216 From NLM.
(196) Fernandez-Pozo, N.; Rosli, H. G.; Martin, G. B.; Mueller, L. A. The SGN VIGS tool: user-friendly software to design virus-induced gene silencing (VIGS) constructs for functional genomics. *Mol Plant* **2015**, *8* (3), 486-488. DOI: 10.1016/j.molp.2014.11.024 From NLM.
(197) Dinesh-Kumar, S. P.; Anandalakshmi, R.; Marathe, R.; Schiff, M.; Liu, Y. Virus-induced gene silencing. *Methods Mol Biol* **2003**, *236*, 287-294. DOI: 10.1385/1-59259-413-1:287 From NLM.
(198) Langmead, B.; Salzberg, S. L. Fast gapped-read alignment with Bowtie 2. *Nat Methods* **2012**, *9* (4), 357-359. DOI: 10.1038/nmeth.1923 From NLM.

(199) Quinlan, A. R.; Hall, I. M. BEDTools: a flexible suite of utilities for comparing genomic features. *Bioinformatics (Oxford, England)* **2010**, *26* (6), 841-842. DOI: 10.1093/bioinformatics/btq033 (acccessed 1/12/2024).
(200) Galvanin, A.; Ayadi, L.; Helm, M.; Motorin, Y.; Marchand, V. Mapping and Quantification of tRNA 2'-O-Methylation by RiboMethSeq. *Methods in molecular biology (Clifton, N.J.)* **2019**, *1870*, 273-295. DOI: 10.1007/978-1-4939-8808-2_21 From NLM.
(201) Jayabalan, A. K.; Griffin, D. E.; Leung, A. K. L. Pro-Viral and Anti-Viral Roles of the RNA-Binding Protein G3BP1. *Viruses* **2023**, *15* (2). DOI: 10.3390/v15020449 From NLM.
(202) Sinha, S.; Singh, K.; Ravi Kumar, Y. S.; Roy, R.; Phadnis, S.; Meena, V.; Bhattacharyya, S.; Verma, B. Dengue virus pathogenesis and host molecular machineries. *Journal of Biomedical Science* **2024**, *31* (1), 43. DOI: 10.1186/s12929-024-01030-9.
(203) Saito, A.; Shofa, M.; Ode, H.; Yumiya, M.; Hirano, J.; Okamoto, T.; Yoshimura, S. H. How Do Flaviviruses Hijack Host Cell Functions by Phase Separation? *Viruses* **2021**, *13* (8). DOI: 10.3390/v13081479 From NLM.

VITA

Shelby L. Brown attended Maple Woods Community College and graduated with an Associate of Arts degree in 2015. She went on to study at the University of Missouri-Kansas City (UMKC), where she began working as an undergraduate researcher for Dr. Theodore White in 2018. Shelby's research primarily focused on studying the influence of media conditions on mixed-species pathogenic fungal growth and competitiveness. She graduated from UMKC in May of 2019 with a Bachelor of Science in Biology and Chemistry.

In 2020, Shelby began working as a laboratory assistant for Dr. Jared P. May at UMKC. Later that year, she began graduate school and officially joined his lab as a PhD student researcher. She was awarded a Master of Science degree in Cell and Molecular Biology in 2022. Her doctoral research centered on the phase separation of viral proteins in plants, and how that phenomenon affects the interplay of virus-host interactions. In 2024, Shelby graduated with a Doctor of Philosophy degree (PhD) with a primary discipline in Cell Biology and Biophysics and two secondary disciplines in Molecular Biology and Biochemistry, and Biomedical and Health Informatics. Shelby plans to continue studying phase separation in relation to virus-host interactions as a post-doctoral researcher and in the future, as an independent researcher.